ABSTRACT

Title of Document:	ENERGY EFFICIENT TWO-PHASE COOLING FOR CONCENTRATED PHOTOVOLTAIC ARRAYS
	Alexander Douglas Reeser, Master of Science, 2013
Directed By:	Professor Avram Bar-Cohen, Department of Mechanical Engineering

Concentrated sunlight focused on the aperture of a photovoltaic solar cell, coupled with high efficiency, triple junction cells can produce much greater power densities than traditional 1 sun photovoltaic cells. However, the large concentration ratios will lead to very high cell temperatures if not efficiently cooled by a thermal management system. Two phase, flow boiling is an attractive cooling option for such CPV arrays.

In this work, two phase flow boiling in mini/microchannels and micro pin fin arrays will be explored as a possible CPV cooling technique. The most energy efficient microchannel design is chosen based on a least-material, least-energy analysis. Heat transfer and pressure drop obtained in micro pin fins will be compared to data in the recent literature and new correlations for heat transfer coefficient and pressure drop will be presented. The work concludes with an energy efficiency comparison of micro pin fins with geometrically similar microchannel geometry.

ENERGY EFFICIENT TWO-PHASE COOLING FOR CONCENTRATED PHOTOVOLTAIC ARRAYS

By

Alexander Douglas Reeser

Thesis submitted to the Faculty of the Graduate School of the
University of Maryland, College Park, in partial fulfillment
of the requirements for the degree of
Master of Science
2013

Advisory Committee:
Professor Avram Bar-Cohen, Chair
Professor Patrick McCluskey
Professor Michael Ohadi

Dedication

This work is dedicated to 3 individuals: my Mother Susan Reeser, Megan Schiffhauer and my Uncle Gary Reeser. These people believed in me from the beginning, and probably will until the end. This work is dedicated to them.

Acknowledgements

Many thanks to Professor Avram Bar-Cohen for generously endowing to me this opportunity at graduate school to obtain my Master's degree. I consider myself lucky to have had such a wonderful advisor during my time here at the University of Maryland. Without his unfathomable knowledge and sagacity, I would not be where I am today.

I would like to thank my thesis defense committee members: Professor Patrick McCluskey and Professor Michael Ohadi for their help throughout the final stages of my work on this thesis.

I also extend thanks to Professor Gad Hetsroni for his valuable input, which has been very welcome.

This research was very appreciatively supported by a grant from the United States – Israel Binational Science Foundation (BSF), Jerusalem, Israel.

My former and current colleagues and labmates: Dr. Peng Wang, Caleb Holloway, Mike Manno, Juan Cevallos, Horacio Nochetto, Frank Robinson and Darin Sharar all deserve merit for their help with my work over the last 2 years.

Special thanks to Mr. Russ Jones of Spectrolab Inc. for his assistance.

Table of Contents

List of Figures

Chapter 1: Introduction

Photovoltaic Solar Cells

With the current energy demands of today's world increasing steadily, a reliable, low cost and long lasting source of energy must be secured. Consider, then, that 4.012×10^7 TWh is the potential average yearly irradiation incident on the land area of the United States. Since its total energy consumption in 2011 was 28,516 TWh [1] - a mere fraction of the total terrestrial irradiation - there is more than enough energy available from the sun to energetically satisfy the needs of the entire continental US.

Silicon-based PV is currently the lowest cost and most widespread technology available to generate free electricity from the sun. A 25% efficient, one square-meter monocrystalline solar module will generate about 250 W of power in direct sunlight. Athough quite low in energy generation per unit area, the average US home has sufficient rooftop, if not backyard, area to meet its power needs with a PV array. However, Silicon PV are expensive to produce in large areas though current methods to increase PV energy density and reduce costs are still being actively researched.

Triple junction solar cells , made from horizontally stacked III-IV semiconductors, are a most promising alternative to silicon solar cells, with a conversion efficiency that has reached 41.1% and is expected to reach even higher values by 2015 [2]. The cell and layers are kept extremely thin – on the order of 8 μm

for the two top layers and 175 µm for the Germanium substrate – to reduce internal series resistances and improve absorption and transmission of the layers. Each junction is tailored to a specific spectral range with minimal overlap thereby capturing more of the solar spectrum than Silicon and improving efficiency up to a theoretical maximum of 86.8% for an infinite-junction cell [3] (see Figure 1.1).

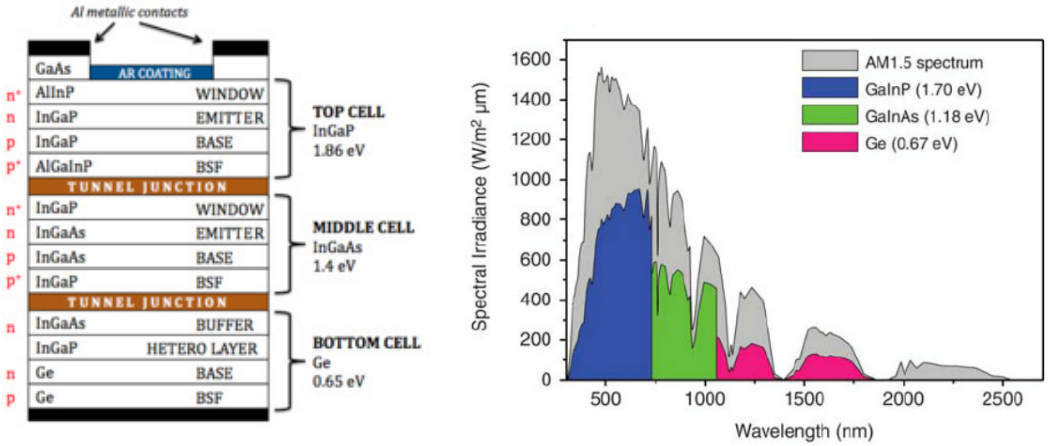

Figure 1.1: Layout and spectral information for a Spectrolab Triple Junction Cell [3]

Optical Concentration

Although multijunction solar cells are more expensive than Silicon, the total cell area needed to provide a specified power level can be drastically reduced, due to their inherently higher efficiency and the use of concentration, thus minimizing solar cell material cost. It is expected that concentrating photovoltaics (CPV) in which the large area of expensive semiconductors is replaced with an equivalent area of relatively low-cost optical reflectors will lead to considerable cost savings. The power density per unit area of the cell is greatly enhanced by collecting and focusing the light into a small intense beam leading to a reduced cell footprint for comparable

power generation. Because of this increased power density and reduced area, the cost of the highest efficiency cell can then be justified.

The magnification ratio or "suns" of a concentration system is the dimensionless unit by which solar concentrators are compared. It is defined as the ratio of average intensity of the focused light divided by the standard non-concentrated normal insolation, 1000 W/m^2 (e.g., 50 suns is 50 kW/m^2 of incident power). For high concentration systems of 500 suns or more the most commonly used optics are point-focus parabolic dish mirrors or Fresnel lenses employed either as multiple, small one-cell systems in series connected module arrays, or a densely packed "parquet" of cells with one large concentrator. Fresnel lenses function by focusing light via refraction, while a short focal length and large aperture can be attained with comparatively less thickness and less material than traditional convex lenses.

Parabolic or circular paraboloid dish concentrators work by reflecting all incoming light incident on its surface to a single focal point, where the receiver containing the cells is located. Parabolic dishes can be scaled up or down in size and have a theoretical concentration limit of 10000 suns. This factor is lower in practice due to imperfections in the reflecting surface, but is still usually capable of up to and exceeding 2000 suns depending on the quality of the manufacturing. See [4] and [5] for more information. Fresnel lenses are ordinarily lower in concentration and smaller in size than parabolic dish systems due to their construction, so are therefore typically used in the series-connected single-cell modular system configurations. Fresnel lens concentration ratios can be enhanced up to 2000 suns using secondary optics.

Some disadvantages of CPV that currently prevent widespread use are: solar tracking systems are required adding significantly to their cost and complexity; optical concentrators do not work nearly as well with diffuse sunlight, limiting their application; and finally, high concentrations may necessitate the use of active cooling systems. Despite these limitations, CPV remain very promising for utility scale and high power installations.

Effect of Elevated Temperature on Cell Performance

Solar cells, like most semiconductor-based electronic devices, are adversely affected by temperature. When the temperature rises more electrons are excited into the conduction band and, in a PV cell, this has the effect of reducing power conversion efficiency. The relationship of cell efficiency to temperature is expressed as a simple, but useful linear equation [6] which is expected to be quite accurate up to temperatures of about 350°C [7]. The linear equation is typically expressed as

$$\eta = \eta_R - C_T(T - T_R) \qquad (1.1)$$

where η is cell efficiency, T is cell temperature, C_T is the temperature coefficient, T_R is the reference temperature, and η_R is the reference efficiency at T_R.

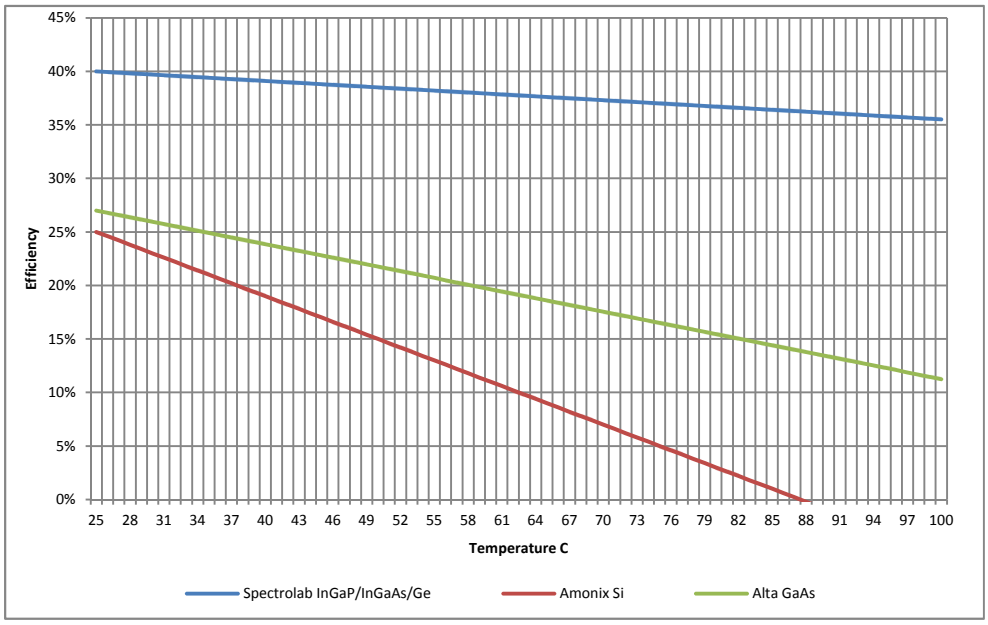

Figure 1.2: Comparison of three types of photovoltaic cells. Spectrolab InGaP/InGaAs/Ge triple junction, Amonix single junction Si, and Alta single junction GaAs

Typically the efficiency quoted by manufacturers of the cell is at ideal standard AM (air mass) 1.5 conditions, with the cell reference temperature at 25°C in direct sun. Manufacturers will specify a mean value of the temperature coefficient for a large population of cells, and a maximum continuous operating temperature, about 100°C for Spectrolab C4MJ cells [8]. The temperature coefficient is difficult to measure, and can vary significantly, depending on various parameters such as the type, diameter, thickness and configuration of the semiconductors used, the spectrum and concentration level of light in which it is being tested, and cell-to-cell manufacturing inconsistencies. Figure 1.2 shows a comparison between production Silicon, GaAs and triple junction cells over a 25° - 100° range. It can be seen from the figure that

efficiency drop and cell type can play an important role in cell performance, especially at increasingly higher temperatures [9] [10].

Concentrated Sunlight and Temperature

The operating temperature of photovoltaic cells will always be above ambient without a cooling solution due to the heat generated by incident sunlight. Cell to ambient temperature differences are typically 20°-30° with un-concentrated, direct sunlight. Even though operating the cells at elevated temperatures will reduce efficiency, no cooling solution is usually implemented for 1 sun concentration, since the extra expense and/or parasitic power loss of the cooling system can not be recovered by the cell's efficiency increase. As the cell surface temperature rises according to the increasing concentration ratio, the loss in efficiency quickly becomes much more significant along with the risk of severe and permanent thermal degradation. Therefore, for CPV systems the heat must be removed by thermal management. Figure 1.3 is a graph of cell temperature versus concentration ratio for a single cell exchanging heat with the ambient only through natural convection (or cooling system failure) calculated with an energy balance:

$$\tau\alpha ACq - \eta\tau\alpha ACq - 2A\varepsilon\sigma(T^4 - T_0^4) - 2Ah(T - T_0) = 0 \qquad (1.2)$$

(Luminous power absorbed) – (electric power to the load) – (heat dissipated from ambient radiation and convection from the top and bottom of the cell) = 0

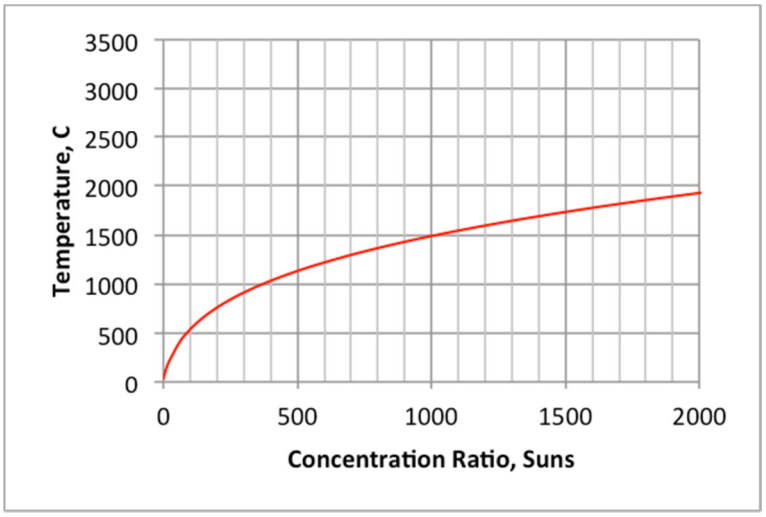

Figure 1.3: Concentration ratio and PV temperature with no thermal management

The model in Equation 1.2 was approximated assuming a transmissivity of 0.8 for the optical collector, a cell absorptivity of 0.85, a cell area of 1 cm^2, and an ambient temperature of 30°C. Additionally, it was assumed that there is no conduction heat transfer taking place and both sides of the cell are cooled by natural convection using an empirical correlation for a horizontal hot plate [11]:

$$h = \frac{Nu \cdot k}{L}, Nu = 0.54Ra^{1/4}, Ra = \frac{g\beta(T - T_\infty)L^3}{\nu\alpha} \qquad (1.3)$$

Most importantly, the figure shows that the cell could reach temperatures that melt not only the metal electrodes at greater than 1000 suns, but also anything that is in thermal contact with the cell. The entire PV system and components will be easily compromised if there is a failure of the cooling system or if the excessive heat is not

properly mitigated. This reinforces the need for a cooling system capable of handling the high heat flux associated with concentrated sunlight.

Passive Cooling

Although several ways of cooling a solar cell are possible, by far the most common method is attaching a thermal solution to the bottom or back surface, since the path of the light to the cell receiver area must not be obstructed. Min and coworkers were able to passively cool a GaInP/GaAs/Ge triple junction cell subjected to 400 suns to 37°C [12]. Even cells subjected to 1300 suns, such as the Greenvolts' system [13], could be passively cooled.

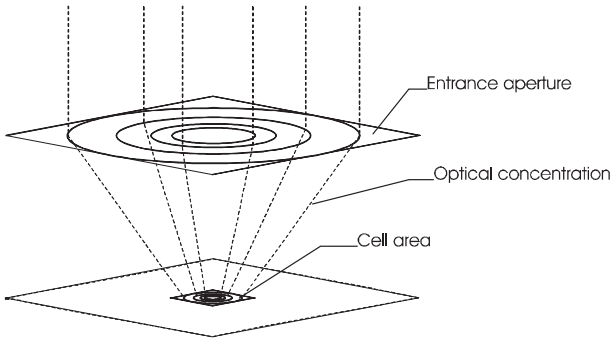

Figure 1.4: Area available for cooling; the large square surrounding cell area [6]

Since the area available for the heat sink can be many times the area of the cell (see Figure 1.4) and since there are no parasitic pumping losses, passive cooling is the most popular method used with single cell arrays in commercial CPV systems [6]. For densely packed cell arrays, in which the area available for the heat sink is less than for single cells, active cooling is generally used.

Single Phase Liquid Cooling

Systems requiring active cooling such as Solar Systems water-cooled, 500 sun parabolic dish CPV [14] as mentioned previously, are typically utilized for cells in the dense array configuration since significant parasitic pumping losses come into play. Multiple cells are needed in each cooling manifold to maintain low relative pumping losses. van Kessel et al. [5] were able to successfully cool a commercially available single 1 cm^2 Spectrolab triple junction cell subjected to 2000 suns, to a junction temperature of 70°C using Dynalene HC-20 coolant. Since the goal of the testing was to assess the long-term thermal reliability of the cell and packaging, pumping losses for their cooling system were not factored into the final power measurements. Multiple closed loop systems such as that tested by van Kessel et al. for many individual cells connected together in a dense array could be impractically large and/or inefficient if used in real applications.

Figure 1.5: Solar Systems' densely packed array visible in its parabolic dish CPV receiver

Verlinden et al. [15] discussed actual performance measurements of the Solar Systems' parabolic dish liquid cooling system, the only known liquid-cooled, high-concentration CPV system previously or currently in commercial production. The initial system design operated at a concentration of 340 suns, which was chosen based on the efficiency loss that occurred for concentrations above that level for the SunPower Corp. Silicon cells they

were using at the time. Each module was composed of 384, 1.0 cm x 1.5 cm cells in sixteen 24-cell modules. A picture of the receiver composed of the 16 individual modules can be seen in Figure 1.5. The cells operated at 24% efficiency (nominally 20% DC system efficiency), generating 3.45kW of power. The total parasitic power loss to the system was 121W, with 86W of that dedicated to pumping power for the

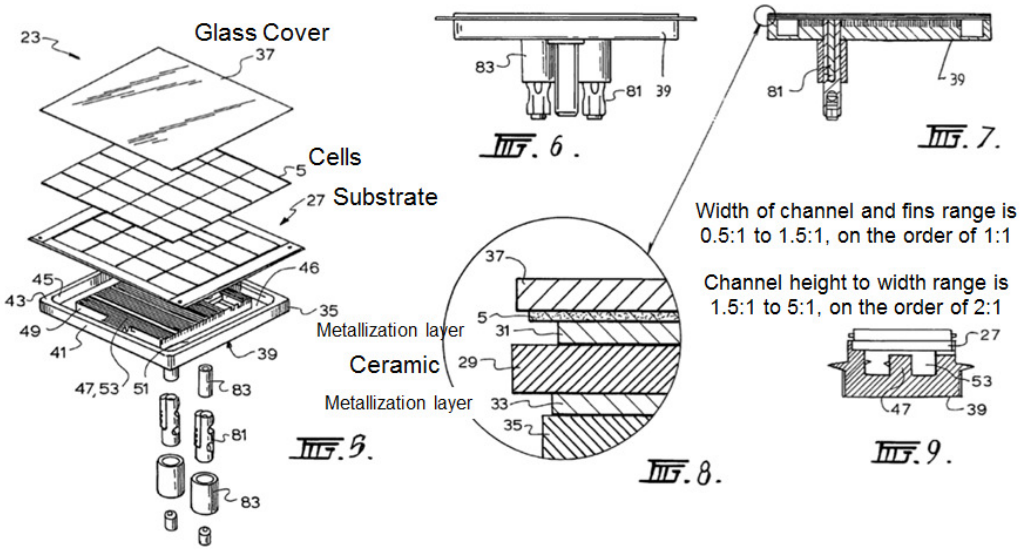

Figure 1.6: Solar Systems individually cooled, 24 cell CPV module.

closed-loop water-cooling system based on a patented design by Lasich [16]. The design uses multiple small, parallel minichannels situated underneath the cell modules, which have their own coolant loop and cold plate. This design has the capacity to remove 500 W/cm^2, enough to efficiently remove heat for much higher concentrations. See Figure 1.6 for a detailed schematic of the module's cooling design.

Recently, Verlinden [17] describes Solar Systems' production CPV system, capable of reaching 500 sun concentrations and, thus, offering a significant update of

the original 340 sun model. It was initially based on CUTJ Spectrolab triple juction cells and uses an improved optical design with multiple reflecting mirrors assembled in a parabolic shape. Additionally, more modern 40% efficient Specrolab cells are replacing the somewhat outdated CUTJ cells. The improved parabolic dish design allows the system to achieve a geometric concentration of 500 suns. With the array of 64 modules totaling over 1500 individual cells Solar Systems are able to get module efficiencies as high as 36.1% and a total rated system output of an impressive 36.5kW compared to the previous 3.45kW achieved. A variation of the original cooling system is still used with these improved dishes, taking advantage of its high thermal capacity. The parasitic power loss for the new 500 sun system is 950W which is still less than 3% of total system output [18].

Two Phase Cooling

Currently, no production CPV systems are cooled using two phase flow boiling. Although the technology has promise for CPV due to the low pumping requirements and excellent heat transfer rates, the thermofluid transport mechanisms for flow boiling are not yet well understood. The only two-phase cooling photovoltaic study known in the literature is by Ho et al [19]. The authors analytically compared water and R134a in two phase and single phase flows for their fixed, high aspect ratio 1 meter long by 0.1 meter wide, single-channel cooler under 100 suns of concentration. They compared several flow rates, channel heights, and inlet temperatures and their effect on cell efficiency and performance. In the analysis they concluded that R134a was the superior fluid due to the low saturation temperature and low required pumping power. The methodology considered only Silicon PV

technology at low concentration ratios of 100 suns for a “linear trough” design, which will cause high frictional pressure drops due to the long channel. They do not discuss what effect the heat transfer coefficient, vapor quality, or changing the cooler geometry may have on cooling performance.

Chapter 2: Heat Transfer Correlations from the Literature

There are many studies in the area of micro scale single-phase and two-phase heat transfer. In this chapter, selected correlations in the literature for heat transfer coefficient, pressure drop, and critical heat flux will be reviewed and summarized.

2.1 Single Phase Micro-Channel Correlations

For single-phase cooling, the heat transfer coefficient on the surface of the channel is given by:

$$h_{sp} = \frac{Nuk_l}{D_h} \qquad (2.1)$$

k_l is the thermal conductivity of the fluid, and D_h is the hydraulic diameter.

The hydraulic diameter will be:

$$D_h = \frac{4W_{ch}H_{ch}}{P} \qquad (2.2)$$

P is the channel perimeter wetted by the fluid, where $P = 2(W_{ch}+H_{ch})$.

For laminar flow (Re < 2300) in rectangular channels, the Nusselt number values can be calculated using a correlation by Copeland [20] that also accounts for the thermal entrance effect:

$$Nu_l = \left\{ \left[2.22 \left(\frac{\mathrm{Re}\,\mathrm{Pr}\,D_h}{L_{CP}} \right)^{0.33} \right]^3 + \left(8.31G - 0.02\right)^3 \right\}^{1/3} \qquad (2.3)$$

The geometric parameter G is:

$$G = \frac{\left(W_{ch} / H_{ch}\right)^2 + 1}{\left(W_{ch} / H_{ch} + 1\right)^2} \qquad (2.4)$$

The dimensionless Reynolds number Re and Prandtl number Pr are defined as:

$$\mathrm{Re} = \frac{\rho D_h V}{\mu} \qquad (2.5)$$

$$\mathrm{Pr} = \frac{\mu c_p}{k_l} \qquad (2.6)$$

Where ρ, μ, c_p k_l, and V are the density, viscosity, heat capacity, thermal conductivity and velocity of the fluid, respectively.

The Nusselt number was correlated by Gnielinsky [21] for turbulent flow (Re > 2300) and the correlation includes the thermal entrance length effect:

$$Nu = \frac{(f/2)(\mathrm{Re}-1000)\mathrm{Pr}}{1+12.7\sqrt{f/2}\left(\mathrm{Pr}^{2/3}-1\right)}\left[1+\left(\frac{D_h}{L}\right)\right] \qquad (2.7)$$

where f is the friction factor, which was correlated by Filonenko [22]:

$$f = \left(1.58\ln(\mathrm{Re}) - 3.28\right)^{-2} \qquad (2.8)$$

Total pressure drop including all components is given as:

$$\Delta P_{sp} = \Delta P_{sp,fric} + \Delta P_{sp,c} + \Delta P_{sp,e} \qquad (2.9)$$

where $\Delta P_{sp,fric}$ is the frictional pressure drop, $\Delta P_{sp,c}$ is the pressure drop due to contraction of the flow, and $\Delta P_{sp,e}$ is the pressure drop due to expansion at the end of the channel. The pressure drop due to contraction $\Delta P_{sp,c}$ and expansion $\Delta P_{sp,e}$ can be calculated as follows [23]:

$$\Delta P_c + \Delta P_e = \frac{\rho V^2}{2}\left(K_c + K_e\right) \qquad (2.10)$$

$$K_c = 0.8 - 0.4\sigma^2$$

$$K_e = (1-\sigma)^2 - 0.4\sigma$$

and σ is the ratio of the fluid flow inlet cross sectional area to the total front cross sectional area of the microcooler:

$$\sigma = \frac{NW_{channel}H_{channel}}{W_{microcooler}H_{channel}} = \frac{NW_{channel}}{W_{microcooler}}$$

The frictional pressure drop $\Delta P_{sp,fric}$ is given by the Darcy-Weisbach equation [24]:

$$\Delta P_{sp,fric} = f\frac{L_{ch}}{D_h}\frac{\rho V^2}{2} \qquad (2.11)$$

where V is the fluid velocity, and f is the friction factor. For laminar flow, the friction factor, which accounts for the thermal entrance length effect, is [25]:

$$f = \frac{1}{\mathrm{Re}}\left\{\left[3.2\left(\frac{D_h \mathrm{Re}}{L_{ch}}\right)^{0.57}\right]^2 + (4.70+19.64G)^2\right\}^{1/2} \qquad (2.12)$$

For turbulent flow, the friction factor is given from Equation 2.8 above.

2.2 Two Phase Micro-Channel Correlations

In this discussion it is assumed that the saturated fluid enters micro-cooler channels fully saturated and without any subcooling. Heat flux and fluid flow are both uniform, and evenly distributed across all the channels. Among all available correlations, the Chen model [26] is recognized as the standard for prediction of the two-phase heat transfer coefficient. While the Chen model was developed for large diameter pipes, it has been shown to provide satisfactory accuracy, with a mean absolute error of 20%, for the dominant annular flow regime in microgaps and microchannels [27]. The Chen correlation includes two thermal transport components

- a microscopic nucleate boiling component and a bulk convective boiling component – that make up the total heat transfer coefficient. The nucleate boiling component is multiplied by a suppression factor, S, and the convective component is multiplied by an enhancement factor, F.

$$h_{tp} = h_{NB} S + h_{conv,tp} F \qquad (2.13)$$

The Dittus-Boelter correlation [28] is used to calculate the liquid-only convective heat transfer coefficient. The Forster and Zuber' pool boiling correlation [29] is the basis for the nucleate boiling component. The enhancement factor, F, is a function of the reciprocal of the Martinelli parameter, X_{tt} and reflects the contribution of the high vapor velocity in the core on convective transfer at the wall. The suppression factor, S, is unity at low vapor qualities and decreases as vapor quality increases. Strong convective heat transfer decreases the wall superheat and suppresses the activation of vapor nucleation sites at the surface thus reducing the contribution of the h_{NB} term [30]. The detailed relations for Chen's model are expressed as [31]:

$$h_{conv} = h_l \, \mathrm{Pr}_l^{0.296} \qquad (2.14)$$

where

$$h_l = 0.023 \left(\frac{k_l}{D} \right) \mathrm{Re}_l^{0.8} \, \mathrm{Pr}_l^{0.4}$$

$$h_{NB} = 0.00122 \left[\frac{k_l^{0.79} c_{pl}^{0.45} \rho_l^{0.49}}{\sigma^{0.5} \mu_l^{0.29} h_{lv}^{0.24} \rho_v^{0.24}} \right] \left[T_w - T_{sat}(P_l) \right]^{0.24} \left[P_{sat}(T_w) - P_l \right]^{0.75}$$

$$S(\mathrm{Re}_{tp}) = \left(1.25 + 2.56 \times 10^{-6} \, \mathrm{Re}_{tp}^{1.17} \right)^{-1}$$

$$\mathrm{Re}_{tp} = \mathrm{Re}_l \left[F(X_{tt}) \right]^{1.25}$$

$$F(X_{tt}) = 1 \qquad \text{for } X_{tt}^{-1} \le 0.1$$

$$F(X_{tt}) = 2.35 \left(0.213 + \frac{1}{X_{tt}} \right)^{0.736} \qquad \text{for } X_{tt}^{-1} > 0.1$$

$$X_{tt} = \left(\frac{1-x}{x}\right)^{0.9}\left(\frac{\rho_v}{\rho_l}\right)^{0.5}\left(\frac{\mu_l}{\mu_v}\right)^{0.1}$$

Thermodynamic equilibrium quality is determined by:

$$x(z) = \frac{Q}{\dot{m}h_{fg}}\frac{z}{L_{mc}} \qquad (2.15)$$

The quality equation is a function of position z along the flow length in the channel. Exit quality is found by setting z equal to the total length of the micro cooler, L_{mc}. h_{fg} is the enthalpy of vaporization of the working fluid and Q is the heat rate.

Using the average heat transfer coefficient, the effective (base) heat transfer coefficient h_{eff} can be calculated as:

$$h_{eff} = \frac{h[2N_{ch}\eta H_{ch} + W_{mc} - (N-1)W_{fin}]}{W_{mc}} \qquad (2.16)$$

Critical heat flux (CHF) is the limiting heat flux; setting the upper bound on the local cooling capacity of the micro-cooler, while dryout – occurring when the exit quality exceeds unity – sets the global cooling capacity. When CHF occurs, a rapid increase in temperature can result, with possible thermal damage of the target device. Therefore, the ability to predict the CHF is important with regards to the limit of safe operation for the two phase cooling system.

Qu and Mudawar [32] developed an empirical saturated CHF correlation with a low mean average error (MAE) of 4% with their experimental database. The

correlation was developed for water and R-113 in rectangular microchannels. It is given as:

$$\frac{q_{CHF}}{\dot{m}h_{fg}} = 33.43\left(\frac{\rho_G}{\rho_L}\right)^{1.11} We_L^{-0.21}\left(\frac{L}{d_e}\right)^{-0.36} \qquad (2.17)$$

Where $We_L = \frac{\dot{m}^2 L}{\rho_L \sigma}$

The total two-phase pressure drop across the micro-cooler (ΔP_{tp}) is calculated as the sum of the frictional pressure drop ($\Delta P_{tp,f}$), the pressure drop caused by the acceleration of the vapor in the channels ($\Delta P_{tp,a}$), the pressure drop due to contraction of the flow ($\Delta P_{tp,c}$), and the pressure drop due to expansion ($\Delta P_{tp,e}$). Any gravitational effects are assumed negligible, since the cooler is assumed to be horizontal in this study. The full two phase pressure drop is given as:

$$\Delta P_{tp} = \Delta P_{tp,fric} + \Delta P_{tp,a} + \Delta P_{tp,c} + \Delta P_{tp,e} \qquad (2.18)$$

There are several empirical correlations for pressure drop in the literature. With an MAE of 24%, the Müller-Steinhagen correlation [33] provides one of the best predictions for the frictional pressure drop component, covering many tube diameters in macro and micro scale. The correlation is outlined below:

$$\left(\frac{dP}{dL}\right)_{tp} = \left\{\left(\frac{dP}{dL}\right)_l + 2\left[\left(\frac{dP}{dL}\right)_l - \left(\frac{dP}{dL}\right)_v\right]x\right\}(1-x)^{1/3} + \left(\frac{dP}{dL}\right)_v x^{3.0} \qquad (2.17)$$

$$\left(\frac{dP}{dL}\right)_l = f_l \frac{2G^2}{\rho_l D}$$

$$\left(\frac{dP}{dL}\right)_v = f_v \frac{2G^2}{\rho_v D}$$

$$f_{l\,or\,v} = \frac{64}{\mathrm{Re}_{l\,or\,v}}, \quad if\ \mathrm{Re} \le 1187$$

$$f_{l\,or\,v} = \frac{0.3164}{\mathrm{Re}_{l\,or\,v}^{1/4}} \quad if\ \mathrm{Re} > 1187$$

The pressure drop caused by the acceleration of the vapor can be calculated using the following equation: $\Delta P_{tp,a} = G^2 v_l \left[\frac{x^2}{\alpha} \frac{\upsilon_v}{\upsilon_l} + \frac{(1-x)^2}{1-\alpha} - 1 \right]$ (2.18)

where α is the void fraction and v_l and v_v are liquid and vapor specific volume, respectively. In this study, the void fraction is evaluated by:

$$\alpha = \frac{1}{1 + \frac{(1-x_e)}{x_e}\left(\frac{\upsilon_l}{\upsilon_v}\right)^{0.67}}$$

The pressure drop due to contraction of the flow $\Delta P_{sp,c}$ and expansion $\Delta P_{sp,e}$ can be calculated from Equation 2.10.

Pumping power is directly related to the product of pressure drop and volumetric flow rate:

$$P_P = \frac{\Delta P \times \dot{V}}{\eta} \qquad (2.19)$$

where η is pump efficiency, which is assumed 100% in this study. With this assumption, it is the fluid power that is shown in the upcoming cases and this value will be lower than the "bus power" required to drive the pump, with pump efficiencies spanning the range of 20%-90%, depending on the type, size, operating

point, and other considerations in the selection of the pump. It should also be noted that the pumping power requirements of the liquid loop, and the condenser, used to cool and condense the vapor, are not included in these calculations.

2.3 Single Phase Micro Pin-Fin Correlation

A summary of the best single phase micro pin fin correlation found in the literature for heat transfer coefficient and frictional pressure drop, proposed by Tullius et al. [34], is given in the following section. It was developed for a range of conditions, including various pin fin shapes, sizes and heat sink materials using water as the working fluid. It was found to have good prediction accuracy of 8%-9% MAE (depending on pin fin shape) for heat transfer coefficient and 6%-9% MAE for pressure drop (also depending on shape of the pin fins). The Tullius et al. correlation can be implemented from micro to mini sized pin fins, as well as a large range of heat flux (10–150 W/cm^2), mass flux (60 kg/m^{2}s–1000 kg/m^{2}s) and Reynolds number range (100–1500). It is to be noted that successful correlation of the data, required a distinct geometric factor, $C_{Nu,}$ and $C_{f,}$ for each pin fin shape. The correlation for Nusselt number is outlined as follows:

$$Nu_f = C_{Nu}\left(\frac{S_L}{D_f}\right)^{0.2}\left(\frac{S_t}{D_f}\right)^{0.2}\left(\frac{h_f}{D_f}\right)^{0.25}\left(1+\frac{dh}{D_f}\right)^{0.4}\mathrm{Re}_f^{0.6}\mathrm{Pr}^{0.36}\left(\frac{\mathrm{Pr}}{\mathrm{Pr}_s}\right)^{0.25} \quad (2.20)$$

Geometry	Circle	Square	Diamond	Triangle	Ellipse	Hexagon
C_{Nu}	0.08	0.0937	0.036	0.0454	0.0936	0.0752

For frictional pressure drop, a similar form along with a shape multiplier is used:

$$f = C_f \left(\frac{S_L}{D_f}\right)^{0.2} \left(\frac{S_t}{D_f}\right)^{0.2} \left(\frac{h_f}{D_f}\right)^{0.18} \left(1+\frac{dh}{D_f}\right)^{0.2} \mathrm{Re}_f^{-0.435} \tag{2.21}$$

Geometry	Circle	Square	Diamond	Triangle	Ellipse	Hexagon
C_f	2.96	5.28	1.81	2.45	3.44	4.53

2.4 Two Phase Micro Pin-Fin Correlations

The summary all two-phase micro pin fin correlations used in this work for heat transfer coefficient and frictional pressure drop are given in this section.

All of the two-phase micro pin fin heat transfer correlations found in the literature were developed for highly subcooled inlet conditions and low exit thermodynamic vapor qualities. No studies (at the time of this work) exist for saturated or near saturated inlet along with high vapor quality flow conditions.

The correlation for heat transfer coefficient by Krishnamurthy and Peles [35] was developed for high heat flux cooling (20–350 W/cm^2) with a Silicon pin fin microcooler, having circular staggered pin fins of 100μm diameter. It uses a superposition type model, with the nucleate boiling term removed. The single phase Nusselt number is valid for Reynolds numbers less than 10^3. The correlation is summarized in Equation 2.22 as follows:

$$\zeta = 1 \tag{2.22}$$

$$(\phi)^2 = 1 + \frac{0.24}{X_{vv}} + \frac{1}{X_{vv}^2}$$

$$\left(\Delta P_f\right)_f = \frac{fN\left(G\left(1-x\right)\right)^2}{2\rho_f} \quad \left(\Delta P_f\right)_v = \frac{fN\left(Gx\right)^2}{2\rho_v}$$

$$X_{vv} = \left[\frac{\left(\Delta P_f / \Delta Z\right)_f}{\left(\Delta P_f / \Delta Z\right)_v}\right]^{1/2}$$

$$h_{sp} = \frac{Nu \cdot k_f}{d_{fin}}$$

$$h_{tp} = \zeta\left(\phi^2\right)^{0.2475} h_{sp}$$

$$Nu = 0.76\left(\frac{S_t}{d}\right)^{0.16}\left(\frac{S_L}{d}\right)^{0.2}\left(\frac{H_{fin}}{d}\right)^{-0.11} \mathrm{Re}^{0.33}\,\mathrm{Pr}^{0.333}$$

In Equation 2.22, X_{vv} is the Martinelli parameter, N is the number of pin fin rows in the flow direction, f is the single phase friction factor, x is the exit quality, S_t , S_L and H_{fin} are the transverse, longitudinal and height of the fins respectively.

The Qu and Siu-Ho [36] correlation was developed for high heat flux cooling (25 – 250 W/cm^2) utilizing a square, staggered copper pin fin array with a subcooled inlet. The model was fitted to Qu and Siu-Ho's original data and requires a subcooling term, in the form of negative inlet quality, in order to obtain proper results. It is therefore not applicable to a saturated inlet condition. The following is a summary of the correlation:

$$h_{tp} = 1.0 - 12.2 \cdot x_{in} \exp\left[-(101 \cdot x_{in} + 29.4) \cdot x_e\right] \cdot 50.44 \qquad (2.23)$$

where x_{in} is the inlet subcooling and x_e is the local quality.

The heat transfer coefficient model developed by McNeil et al. [37] is for relatively low heat flux cooling (1 – 15 W/cm^2) using refrigerant R113 in copper inline pin fins. Similar to the Krishnamurthy and Peles model, it utilizes superposition, which addresses the nucleate boiling and convective heat transfer mechanisms separately. It is the only micro pin fin correlation in this study that was developed for inline pin fin arrays. The correlation is given below.

$$h_{tp} = S \cdot h_{nb} + F \cdot h_{conv} \qquad (2.24)$$

Single phase convective term:

$$h_{sp} = \frac{Nu \cdot k_f}{d_{fin}}$$

$Nu = Nu_r \times F_1 \times F_4$ (F_4 *is a row dependent multiplier*)

$Nu_r = a \cdot \mathrm{Re}_b^m \, \mathrm{Pr}_b^{0.34}$

For $\mathrm{Re} < 300$, $a = 0.742, m = 0.431$

For $300 < \mathrm{Re} < 2 \times 10^5$, $a = 0.211, m = 0.651$

For $\mathrm{Re} > 2 \times 10^5$, $a = 0.116, m = 0.7$

$$F_1 = \left(\frac{\mathrm{Pr}_b}{\mathrm{Pr}_w} \right)^{0.26}$$

Nucleate boiling term:

$$P_r = \frac{P}{P_{cr}}$$

$$h_{nb} = 0.945 P_r^{0.17} + 4 P_r^{1.2} + 10 P_r^{10} (P_{cr}/1000)^{0.69} (q''/1000)^{0.7}$$

Enhancement and suppression factors:

$$X_0 = 0.041 \left[\frac{\sigma}{g(\rho_l - \rho_v)} \right]^{1/2}$$

$$X_c = F \cdot h_{conv} \frac{X_0}{k}$$

$$S = \frac{1}{X_c} \left(1 - e^{-X_c} \right)$$

$$F = \left(\phi_L^2 \right)^{0.36}$$

$$(\phi_L)^2 = 1 + \frac{8}{X_{tt}} + \frac{1}{X_{tt}^2}$$

$$X_{tt} = \left(\frac{1-x}{x} \right)^{0.9} * \left(\frac{\rho_v}{\rho_l} \right)^{1/2} \left(\frac{\mu_l}{\mu_v} \right)^{0.1}$$

Due to the limited research database of two phase flow in pin fins, only one pressure drop correlation exists that is suitable for flow boiling in pin fin arrays. The correlation that will be utilized in this work is by Qu and Siu-Ho [38]. Their Lockhart-Martinelli type correlation was developed for the same test section and experimental conditions as their heat transfer coefficient correlation [34]. The correlation is dependent on the level of inlet subcooling and heat flux, which in turn determine the pin fin row, in the flow direction, where saturated boiling commences, N_{sat} (pin fin row where local vapor quality = 0). It is assumed that the fluid maintains a liquid-only state in the entire subcooled region. ΔP_{tp} is thus defined as the sum of two separate, segment-based, closed form summations where local fluid property values are re-calculated at each pin fin row, *i*. ΔP_{sub} is the subcooled frictional pressure drop that dominates before the local vapor quality reaches zero (local vapor

quality < 0), therefore the summation is from $i = 1$ to N_{sat-1}. The ΔP_{sat} is the saturated boiling frictional pressure drop component, which occurs from N_{sat} to N_f (the total number of pin fin rows in the flow direction). A summary of the Qu and Siu-Ho correlation for pressure drop is given below.

$$\Delta P_{sub} = \sum_{i=1}^{N_{sat-1}} \left[f_{sp,,i} \left(\frac{\mu_{f,i}}{\mu_{w,i}} \right)^{0.58} \frac{G^2}{2\rho_{f,i}} \right] \tag{2.25}$$

$$\Delta P_{sat} = \sum_{i=N_{sat}}^{N_f} \left[f_{sp,,i} \frac{v_{f,i} G^2 (1 - x_{local,i})^2}{2} \phi_{f,i}^2 \right]$$

$$f_{sp} = 20.09 \, \mathrm{Re}_{sp,f}^{-0.547}$$

$$\phi_f^2 = 1 + \frac{C}{X_{vv}} + \frac{1}{X_{vv}^2}$$

$$C = 5$$

$$X_{vv} = \left(\frac{\mu_f}{\mu_g} \right)^{0.274} \left(\frac{1 - x_{local}}{x_{local}} \right)^{0.727} \left(\frac{v_f}{v_g} \right)^{0.5}$$

$$\Delta P_{tp} = \Delta P_{sub} + \Delta P_{sat}$$

Chapter 3: Energy Efficient Micro-Cooler Design for High Heat Flux CPV Systems

In this chapter, the potential application of an R134a-cooled two-phase micro-cooler for thermal management of a triple junction concentrated photovoltaic (CPV) solar cell under a 2000 sun concentration is presented. An analytical model for the triple-junction solar cell temperature based on prediction of two-phase flow boiling in micro-channel coolers is developed and analytically exercised with empirical

correlations from the open literature for the heat transfer coefficient, pressure drop, and critical heat flux. The thermo-fluid analysis is augmented by detailed energy modeling relating the solar energy harvest to the "parasitic" work expended to provide the requisite cooling, including pumping power and the energy consumed in the formation and fabrication of the micro-cooler itself. Three fin thicknesses between 100μm and 500μm, a variable number of fins between zero and 9, and 5 channel heights between 0.25mm and 3mm are examined for a R134a flow rate of 0.85g/s to determine the energy efficient microcooler design under these conditions for a $1cm^2$ triple junction CPV cell.

3.1 Energy Optimization: Coefficient of Performance

The Coefficient of Performance (COP) is traditionally used to describe the cooling capability or heat output of a thermodynamic system in relation to the electrical or mechanical energy used to drive the cooling or heating process and serves as a basis of comparison for heat pump and refrigeration equipment. It is expressed as $COP = \frac{Q}{W}$ where Q is the heating energy or cooling output (kWh) and W is the energy input (kWh).

With a modest re-definition, this metric can also be applied to actively cooled CPV cells, taking the ratio of the useful electrical power generated by the cell (solar energy harvest or net solar energy) to the power consumed by the pump to cool the cell. The equation for COP used in this way will be given as:

$$COP = \frac{E_{PV} - P_{Pump}}{P_{Pump}} = \frac{\text{Solar Energy Harvest}}{\text{Pumping Power}} \qquad (3.1)$$

This equation depends only on solar energy and pumping power and does not include energy from other sources. However, it could be modified to include other parasitic losses e.g. transmission line loss and power for the control electronics. In addition to the pumping power and parasitic losses, account should also be taken of the energy associated with the mining and refining of the raw materials, as well as the manufacture, transportation and final assembly of all the various components and materials in a CPV system. Such an extensive energy analysis, cataloging, quantifying, and optimizing the energy content for each of these processes for all the components, is beyond the scope of the present effort. Instead, this study will limit its attention to the embedded energy in the Aluminum micro-cooler material and the required pumping power**.**

The total mass of the Aluminum used in the fabrication of the micro-cooler determines the embedded energy content and has a direct impact on the performance of the cooling system. The material mass has associated formation energy for processing the raw Aluminum ingots and additional energy is required for the further refinement or "fabrication" of that raw metal into its final form. Iyengar *et al.* [39] found that 85 kWh/kg or 306 MJ/kg was used to extrude and fabricate air-cooled Aluminum heat sinks. Embedded energy factors exist for many other common heat exchanger and heat sink materials and this methodology can therefore be applied to materials other than Aluminum.

In the COP of Equation 3.1, we will add the embedded energy to the pumping power in the denominator and convert the power terms to work terms by multiplying by the total lifetime hours of operation, t_L. The result is a Total Coefficient of Performance (COP_T) metric defined as:

$$COP_T = COP\left(\frac{P_{pump}t_L}{P_{pump}t_L + 85000m}\right) = \frac{\text{Solar Energy Harvest} \cdot \text{Lifetime Hours}}{\text{Pumping Work + Embodied Energy}} \qquad (3.2)$$

Although the COP_T metric was derived from the COP, it is distinct in that embedded energy is included to account for the energy required for the formation and fabrication of the Aluminum as well as the lifetime energy of the pump. For the duration of this paper, the terms COP and COP_T will be in reference to the definitions given in Equations 3.1 and 3.2, respectively. In addition, since multi-junction cells are expected to last 25 years or more in a stable environment, and the solar industry is under pressure to increase cell lifetime to at least 30 years [5], in this analysis total lifetime t_L will be taken as 30 years assuming CPV operation for an average of 12 hours per day. It will be shown that COP and COP_T can be useful metrics to aid in identifying the system geometry that allows the most efficient use of mass and pumping power, while maintaining good cooling performance and high solar cell efficiency. Finally, it should be noted that the COP and COP_T are indirectly dependent on system parameters such as the fin geometry, flow rate, solar concentration etc.

3.2 Conceptual Design of the CPV Microcooler

As a vehicle for exploring the efficacy of two-phase cooling of a 2000 sun CPV, we have simulated the thermo-fluid behavior of a notional CPV cell based on a Spectrolab 100 mm^2 C4MJ triple junction device, consisting of 3 layers of III-V semiconductors made from compounds of Indium, Arsenic, Gallium, and Phosphorus on a Germanium substrate. Each layer is very thin; the topmost layers (typically GaInP and GaInAs) are less than 10 μm to allow light to propagate to successive layers which respond to a different wavelength of the light spectrum. The bottom Germanium substrate is typically the thickest layer and each of the two top layers are epitaxially grown using a form of metalorganic vapour phase deposition [40]. Triple junction cells such as the C4MJ are ideal for high solar concentration applications (>500 suns) due to their low internal series resistance and their consequent ability to provide better performance in a CPV application compared to traditional single junction silicon-based cells [41]. The typical C4MJ efficiency of 40% is for a temperature of 25°C under the ASTM G-173-03 AM 1.5 standard test condition for the direct solar component of spectral irradiance, 50 W/cm^2 of insolation, 1 standard atmosphere of pressure, and at normal incidence to the sun. The temperature coefficient of conversion efficiency is 0.06%/°C, leading to a linear decrease in cell efficiency as temperature increases, as:

$$\eta = 40\% - 0.06\%(T - 25°C) \tag{3.3}$$

The values given here are expected to be the average performance over a large population of Spectrolab cells. [42]

The Aluminum micro-cooler overall dimensions are identical to the 10 mm x 10 mm overall cell base dimensions. The cell is attached to the top face of the micro-cooler by a 50 μm layer of In97Ag03 lead-free solder, chosen for its relatively high

Table 3.1: Micro-cooler dimensions (mm)

Parameter					Value	
Overall Length (L_{mc})					10	
Overall Width (W_{mc})					10	
Base Thickness (H_b)					0.1, 0.3, 0.5	
Channel Height (H_{ch})					0.25, 0.5, 1, 2, 3	
	100 μm Fin Thickness		300 μm Fin Thickness		500 μm Fin thickness	
Channel Number	Fin Thickness (W_w)	Channel Width (W_{ch})	Fin Thickness (W_w)	Channel Width (W_{ch})	Fin Thickness (W_w)	Channel Width (W_{ch})
1	0.1	9.8	0.3	9.4	0.5	9
2	0.1	4.85	0.3	4.55	0.5	4.25
3	0.1	3.2	0.3	2.93	0.5	2.67
4	0.1	2.375	0.3	2.13	0.5	1.875
5	0.1	1.88	0.3	1.64	0.5	1.4
6	0.1	1.55	0.3	1.317	0.5	1.083
7	0.1	1.314	0.3	1.09	0.5	0.857
8	0.1	1.138	0.3	0.913	0.5	0.688
9	0.1	1	0.3	0.778	0.5	0.556
10	0.1	0.89	0.3	0.67	0.5	0.45

thermal conductivity of 73 W/m-K. Following the manufacturer's recommendation, the cell temperature will be kept below 110°C to prevent thermal degradation.

The simulation described herein involved the use of 3 distinct fin thicknesses (100 μm, 300 μm and 500 μm) and the number of fins varying from zero, i.e. a single "open" channel, to 9, and 5 channel heights (0.25mm, 0.5mm, 1mm, 2mm and 3mm). The wall thickness and base thickness were taken to be equal to the thickness of the fin. These geometric parameters are summarized in Table 3.1. For the single phase baseline computations, water was used due to its excellent thermal properties. Water enters the channels at 30°C and atmospheric pressure. R134a was chosen as the two phase working fluid due to its relatively high latent heat of vaporization and low

saturation temperature. It is assumed that R134a enters the channels fully saturated at 30°C, which requires a saturation pressure of 7.7 Bar at the inlet (except where indicated).

3.3 Parametric Study: Energy Optimization Results

The amount of waste heat that must be removed by the micro-cooler is directly related to the solar cell efficiency, η, calculated from Equation 1.1. The waste heat is the portion of incident solar energy that is not converted to electricity, i.e. $(1-\eta)\cdot\dot{Q}$. The solar generated power and waste heat are complementary to each other; their total must equal the irradiation or solar flux, $\dot{Q}$. As the cell temperature rises, its conversion efficiency will decrease, necessitating more heat removal by the microcooler. Conversely, as the cell temperature decreases, its conversion efficiency will improve and less heat will need to be removed. Because of the interdependence of efficiency and cooling rate, the subject simulations were performed iteratively, keeping the solar flux constant at 200 W/cm^2 (2000 suns), until agreement of better than ±0.005% in the heat dissipation was achieved. This method ensured that solar generated power and heat dissipation were consistent with each other.

Throughout the two phase calculation domain, the mass flow rate was kept constant. It is well known that at constant heat flux, two-phase flow requires lower pumping power at high qualities due to relatively low flow rates. Therefore the hypothetical two phase cooling system was chosen to operate at a 0.85 g/s mass flow rate that leads to a high exit vapor quality of approximately 85%. The single phase water results were calculated at much higher mass flow rates, ranging from about 10-

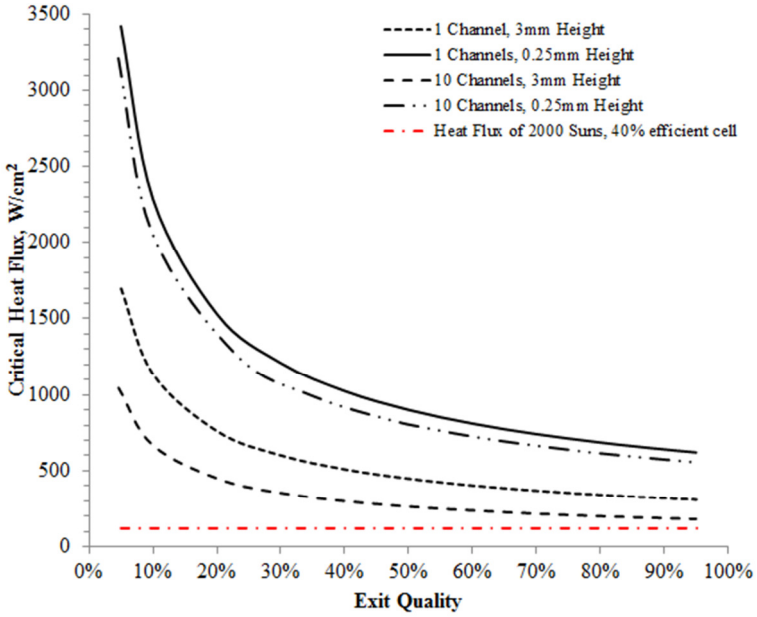

Figure 3.1: Comparison of critical heat flux (CHF) as a function of exit vapor quality

50 g/s of water, which would yield cell temperatures that match those achieved with two-phase R134a flow.

Critical heat flux is calculated using Equation (2.17) and shown in Figure 3.1 as a function of thermodynamic exit quality. The horizontal dashed line represents the location of the heat flux encountered at 2000 suns with a conversion efficiency of 40%. Since the number of channels ranged from 1 to 10 and the channel height spanned from 0.25mm to 3mm, the 4 possible combinations shown in Figure 3.1

define the upper and lower geometric bounds that were investigated, and are seen to be above the heat flux generated by 2000 suns on a 40% efficient cell. Thus it is shown that critical heat flux will not be encountered in the stated parametric range nor pose a constraint on the cooling effectiveness of the two phase microcooler.

Heat Transfer Coefficient

The two-phase heat transfer coefficient in the micro-cooler is the key parameter in this study and governs the total heat transfer from the CPV cell to the refrigerant. The "effective" heat transfer coefficient, obtained by summing up the heat transfer in all the channels and normalizing it to the base area of the micro-cooler was calculated for the stated number of channels and is depicted in Figure 3.2, where the effective heat transfer coefficients are seen to range from approximately 35kW/m^2K to 65kW/m^2K across the stated parametric range.

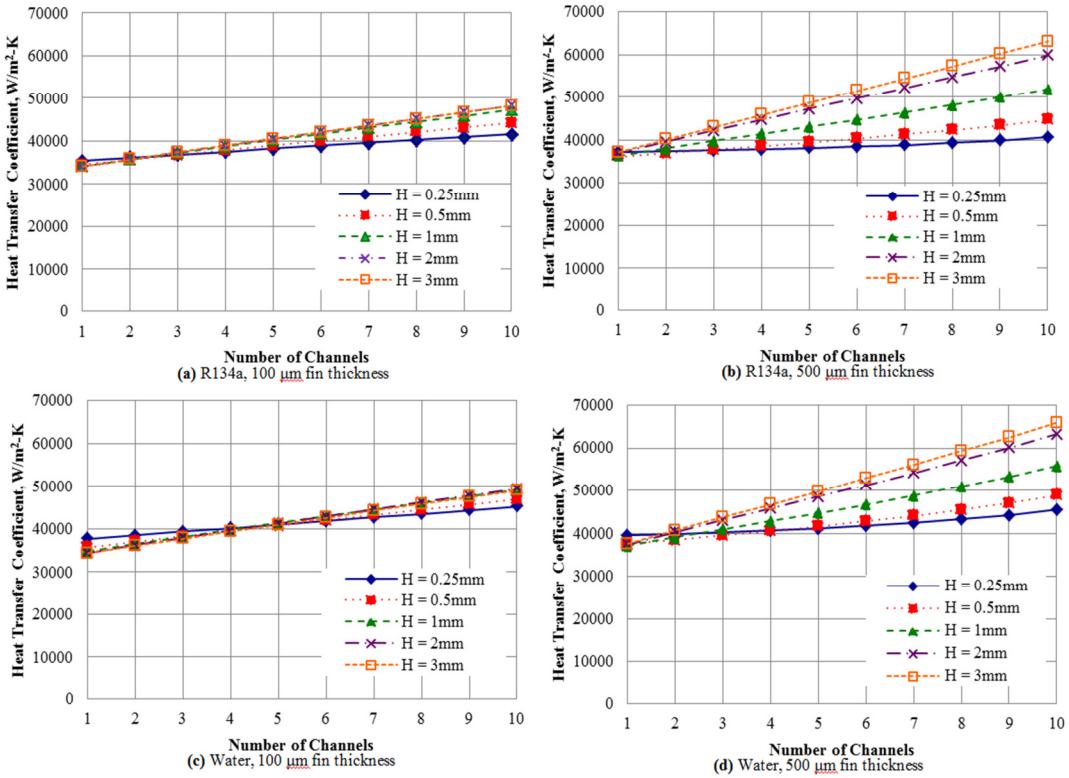

Figure 3.2: Single phase and two-phase effective heat transfer coefficient. R134a flow rate: 0.85 g/s

The increase in the effective heat transfer coefficient with the number of channels is characterized by a smooth, linear trend. However, as the channel height and fin thickness increase, the slope of each trend line increases. This monotonic increase in effective heat transfer coefficient as the number of channels is increased along the x-axis, is greatest for the 3mm height line. The trend of increasing effective heat transfer coefficient with channel number, depicted in Figure 3.2, is due to the combined effect of smaller hydraulic diameter and greater wetted surface area. Interestingly for the conditions examined, the single phase heat transfer coefficients attained with water and the two-phase heat transfer coefficients attained with R134a

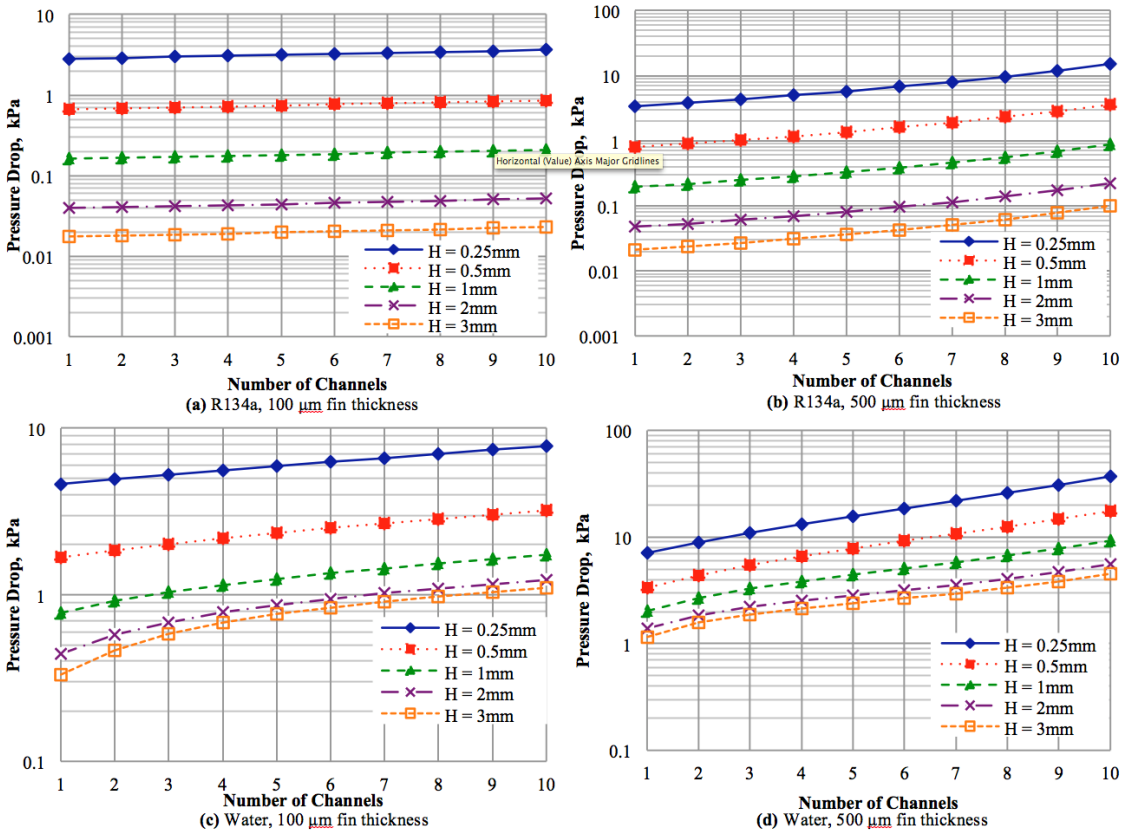

Figure 3.3: Single phase and two-phase pressure drop. R134a flow rate: 0.85 g/s

are similar in magnitude. Although this similarity is achieved with much higher water flow rates and subsequently more water pumping power.

Pressure Drop

Pressure drop is one of the essential parameters in this analysis because it determines the power required for pumping the fluid and how large a pump is needed to overcome resistance to flow. Pressure drop plots, for the parametric range examined in this study are shown in Figure 3.3 and seen to range from 0.77kPa to 37kPa for single phase water and 0.16kPa to 15kPa for two phase R134a across the parametric range. The two-phase pressure drop is very low for channels higher than

0.5mm and, in general, the single-phase pressure drops are noticeably higher than the two-phase values for the same number of channels and fin thickness combination.

The greatest pressure drop values were observed for the smallest channel dimensions, e.g. the 10-channel micro-cooler design with 0.25mm tall, 500µm thick fins. The single-phase pumping power that is required to match the cooling performance of two-phase over the range investigated was also considerably higher (see Figure 3.4) due to the higher flow rates needed and the greater pressure drops experienced in maintaining identical cell temperatures. While most of the single-phase pumping power for a single 1 cm^2 microcooler is on the order of milliwatts, two-phase cooling spans a much wider range starting in the tens of microwatts up to

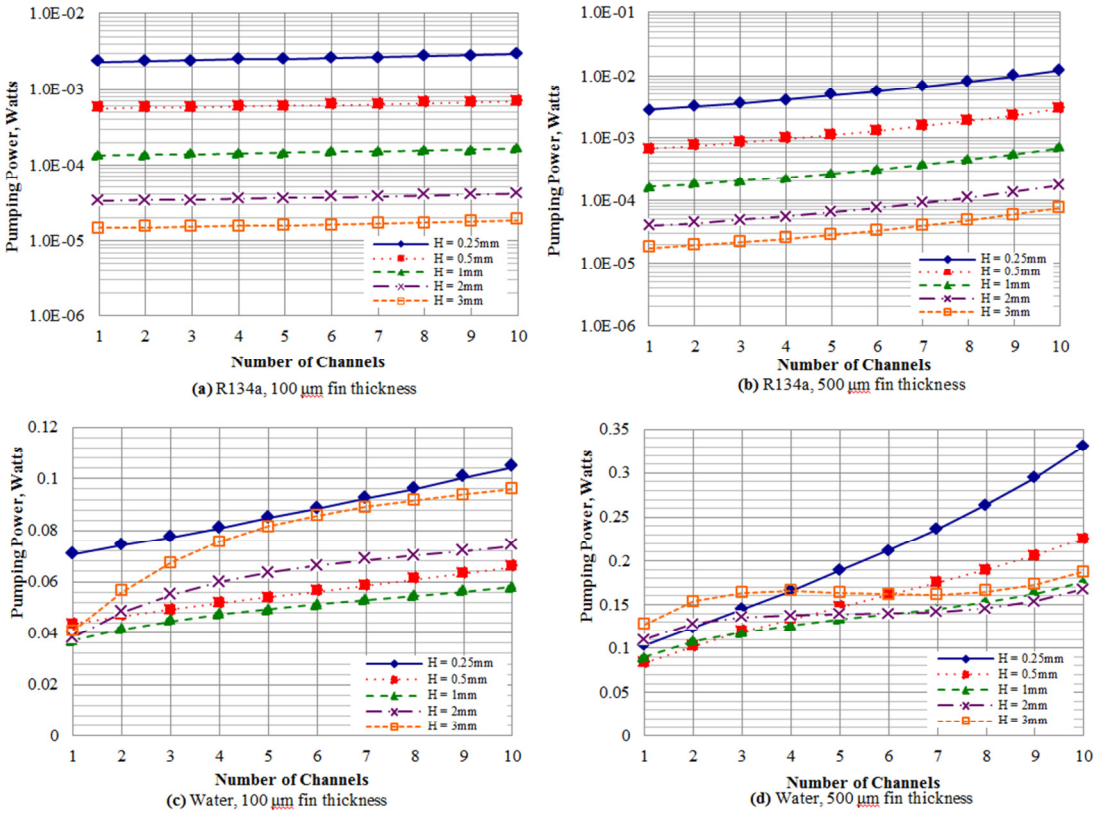

Figure 3.4: Comparison of pumping power for water-cooled single-phase and R134a-cooled two-phase micro-coolers

just over 10 milliwatts for the 10mm by 10mm CPV module.

Temperature of the Cell

Since the CPV energy conversion efficiency depends on the cell temperature as per Equation 3.3, the temperatures experienced by the cell are central to its performance. Figure 3.5 depicts the cell temperature for two-phase R134a cooling for 100µm and 500µm fin thickness. As previously noted, water flow rates were adjusted so as to maintain cell temperatures identical to that achieved with two-phase R134a

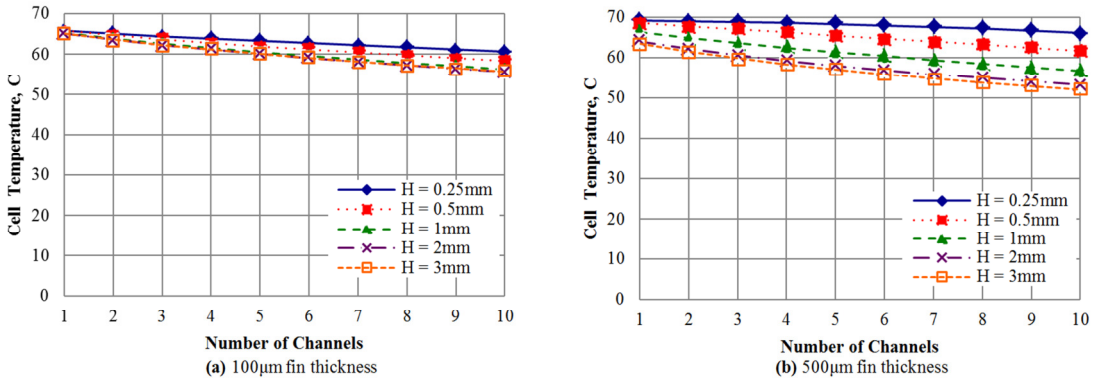

Figure 3.5: Solar cell base temperature.

cooling. Therefore, the single-phase water temperatures are identical to the two-phase temperatures shown in Figure 3.5. It is expected that increasing the number of channels will lower cell temperature due to larger heat transfer surface, smaller hydraulic diameter, and thus higher effective heat transfer coefficients. Interestingly, for all the single-phase and two-phase liquid cooling configurations studied, the solar cell temperature was successfully held below 70°C for a concentration ratio of 2000 suns. Moreover, in the range studied, the effect of adding fins results in just a modest temperature reduction, with 3mm channel height for the range of 1 to 10 channels

providing a cell temperature of 52°C, the lowest temperature observed. The highest temperature was 69°C and occurred for the 0.25mm height single channel.

Solar Cell Performance

The primary motivation for using a two-phase CPV cooling solution is to reduce the parasitic pumping load on the solar power system while maintaining a sufficiently low temperature for efficient power production. Figure 3.6 shows the trend of solar energy harvest, which is the total net power generation of the cell operating under a concentration level of 2000 suns, after subtracting the pumping power required to cool the CPV, and is seen to vary by little more than 1 Watt across the parametric range**.** Figure 3.6 shows solar energy harvest for a 10mm by 10mm CPV cooled by a microchannel cooler using R134a flowing past 500µm thick fins 0.25mm to 3mm tall.

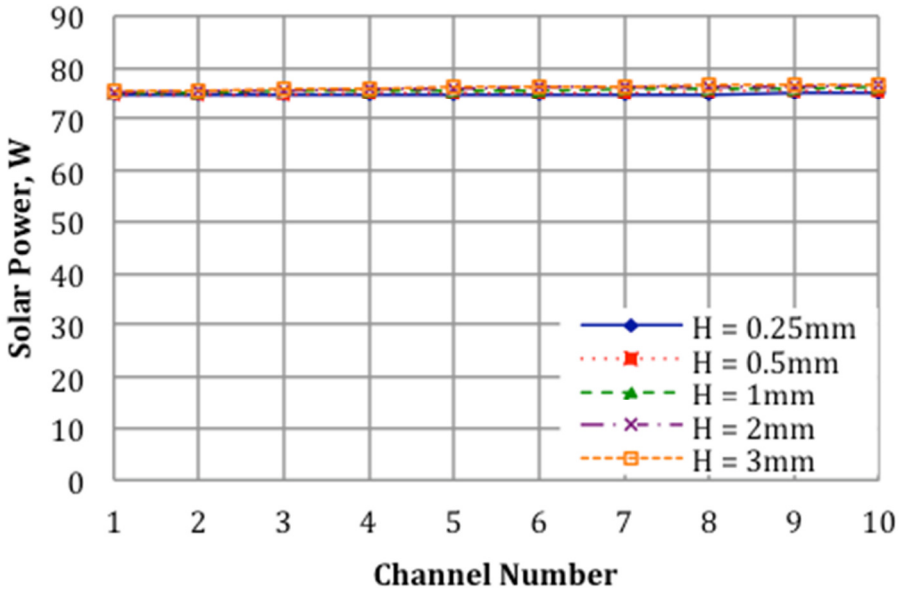

Figure 3.6: Solar energy harvest for a R134a-cooled two-phase micro-cooler. R134a flow rate: 0.85 g/s

Coefficient of Performance

The COP and COP_T metrics defined in Equations 3.1 and 3.2 can be used as an aid to drive the parametric design to the most optimal configuration, since it is not yet completely clear from the previous data where this optimum would occur. The values of COP and COP_T are shown in Figures 3.7 and 3.8, respectively. The two-phase COP is seen to increase monotonically with greater channel heights, but for

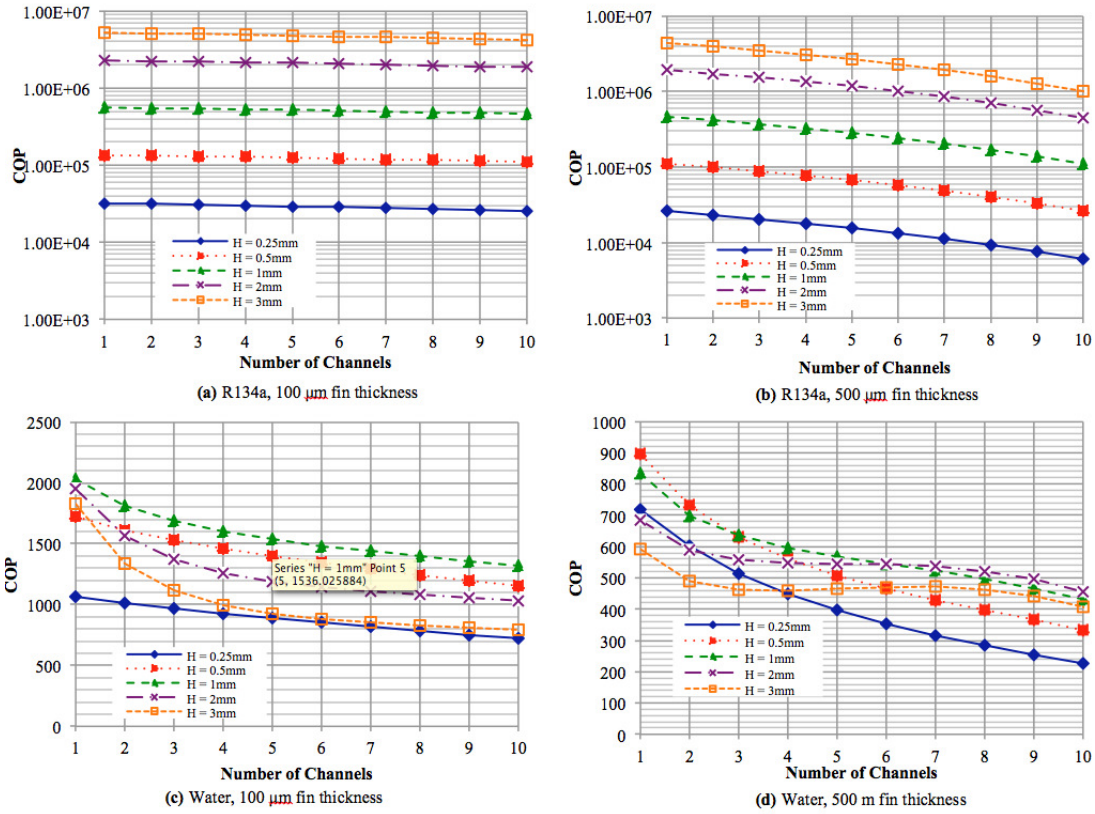

Figure 3.7: Single phase and two-phase coefficient of performance. R134a flow rate: 0.85 g/s

each height a maximum value is attained for a single channel, and the COP is then seen to decrease with an increase in the number of channels. Single-phase COP also

decreases with channel number and it is easier to observe that maximum COP occurs for a microcooler with just a single channel. In comparing the COP with the pumping

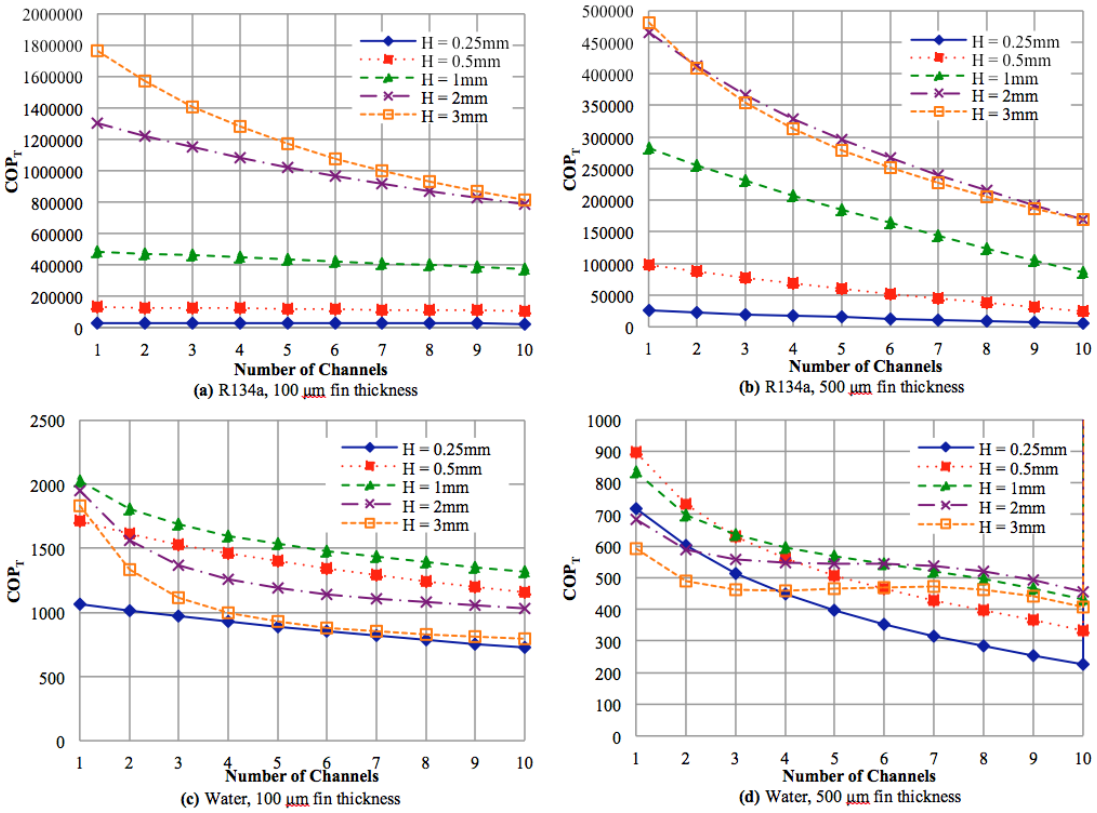

Figure 3.8: Single phase and two-phase total coefficient of performance (COP_T). R134a flow rate: 0.85 g/s

power graphs in Figure 3.4, the COP is seen to be inversely proportional to the pumping power for single-phase water. Two-phase COP_T also increases with channel height, but the 3mm line has a lower value for most of the range in the 300μm and 500μm fin thickness cases. This suggests that fin heights above 2mm are inefficient at those points because the additional mass does not sufficiently improve cooling performance to compensate for the higher energy investment and thus suppresses the COP_T. Due to the high pumping power in single-phase water cooling, accounting for

nearly 100% of the invested energy in the microcooler, the COP_T curves for this mode of cooling essentially match the COP at every point.

The lifetime pumping percent for two-phase cooling spans a much larger range than single phase, reaching as low as 10% for some 3mm height cases and rising to as high as 99% for a few 0.25 channel height designs. Figure 3.9 displays the pumping work percentage versus channel number for two-phase R134a at the

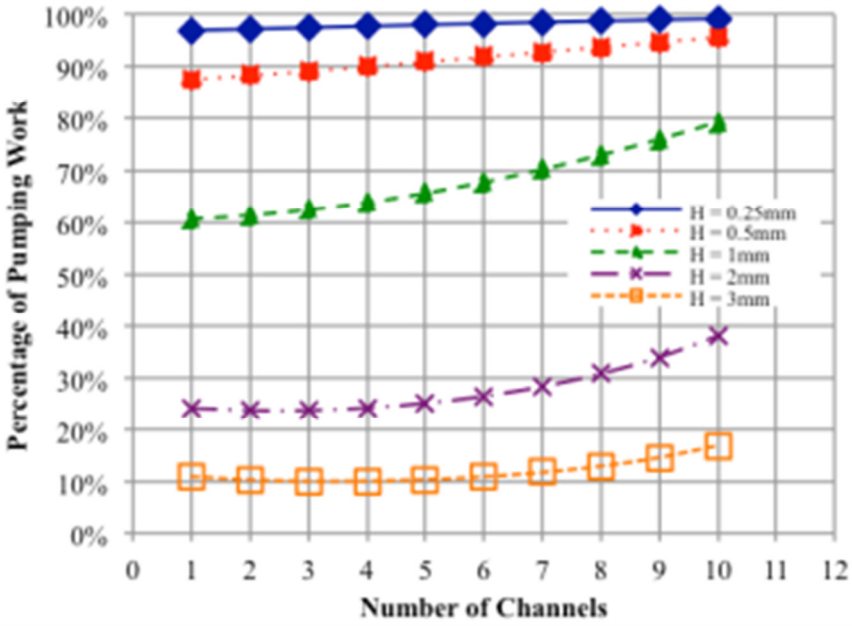

Figure 3.9: Pumping work percentage vs. number of channels. R134a flow rate: 0.85 g/s

constant flow rate of 0.85 g/s. Since pumping work can make up a much smaller fraction of the COP_T, the embedded energy of the Aluminum micro-cooler can play a more pronounced role in determining the value of the COP_T.

It is clear from our investigation that COP and COP_T peak at the single channel point for all graphs followed by a downward trend that steepens as fin thickness increases. This downward sloping trend persists into higher channel number

with no recovery or upward turn observed for these cases. It would appear, then, that based on COP analysis the optimal configuration for cooling a 10mm x 10mm triple junction cell would be a single "microgap" channel.

3.4 Energy Analysis of Concentrating Silicon Photovoltaics

Up until now, our energy efficiency analysis has been focused on cooling the latest generation of 40% efficient triple junction CPV cells. Since these cells are very insensitive to temperature, we have shown that they are very good candidates for high heat flux cooling and do not require miniscule aspect ratio, multiple channel microcoolers for efficient cooling. However, since triple junction cells are very expensive to produce and Silicon-based CPV are far more sensitive to temperature it is of interest to apply the two phase flow boiling cooling methods examined thus far to Silicon-based CPV. The following paragraphs are a brief demonstration of the potential benefits of Silicon CPV cooling using two phase R134a.

Until recently, Silicon based CPV cells were the standard technology used with leading commercial high-concentration systems. The highest efficiency CPV Silicon cell was developed by Amonix in 2005 and holds the record efficiency of 25% at 400 suns [43]. The temperature coefficient of efficiency for these cells was -0.4% per °C [44], much larger than the coefficient of -0.06% for triple junction CPV. Using this information with Equation 1.1 we construct a new efficiency equation for Amonix Silicon-based CPV:

$$\eta = 25\% - 0.4\%(T - 25°C) \tag{3.4}$$

Equation 3.4 is valid up to 400 suns. At concentration ratios far beyond 400 suns, nonlinearity in efficiency as well as increased series resistance become important and will reduce cell efficiency. Nevertheless, if research and development in Silicon-based CPV resumed, concentrations above 500 suns could be easily realized today [44].

Figure 3.10 shows solar energy harvest of a two phase R134a cooled 1cm x 1cm Amonix Silicon CPV cell for 400, 1000 and 2000 suns. The number of channels is increased on the x-axis from 1 channel to a total of 30. At the single channel point, the best solar energy harvest of 9 watts is obtained by the microgap cooler at 1000 suns. As the number of channels is increased, the 2000 sun microcooler will obtain

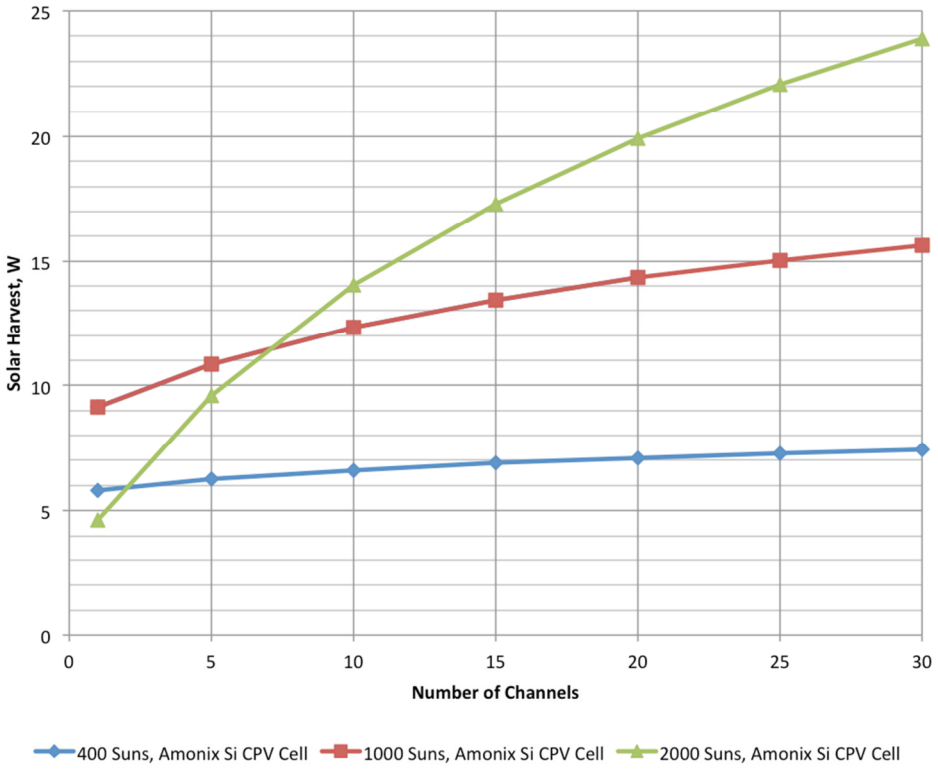

Figure 3.10: Solar Energy Harvest vs. Number of Channels. 400, 1000 and 2000 sun, 1cm x 1cm, Silicon-based Amonix CPV cell

the best solar energy harvest of 24 watts at the 30 channel point, gaining about 8 watts over the microcooler operating at 1000 suns. Though Silicon cells rated for 1000 and 2000 suns have not yet been developed, the results indicate that multi-microchannel coolers could extract more power from these higher concentration systems if cells rated for such insolations existed. In fact, for a 2000 sun CPV, increasing the number of channels from 1 to 30 can increase power output by 20 watts per each 1 cm^2 cell. This result becomes diminished as solar concentration is decreased to 400 suns however. For today's "best" 400 suns, it would appear that the solar harvest is marginally sensitive to the number of microchannels.

Figure 3.11 is the COP_T result for the same R134a cooling of 1cm x 1cm

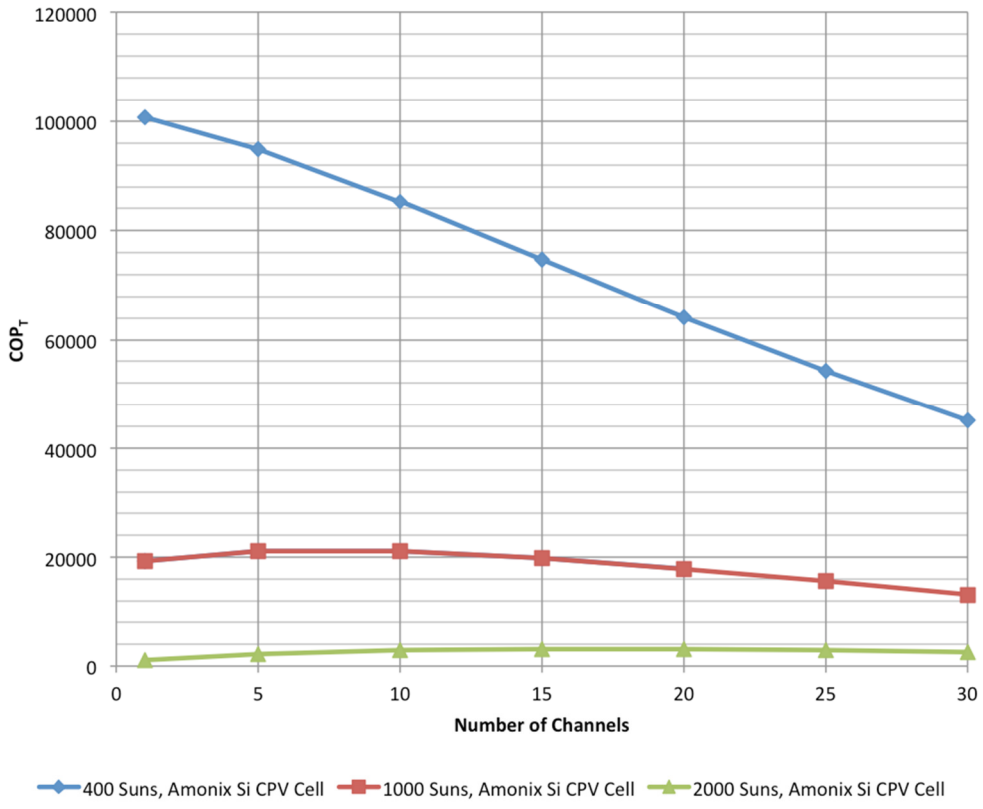

Figure 3.11: COP_T vs. Number of Channels. 400, 1000 and 2000 sun, 1cm x 1cm, Silicon-based Amonix CPV cell

Silicon CPV cells at 400, 1000 and 2000 suns. Like in Figure 3.10 the COP_T is plotted over the number of channels on the x-axis from 1-30 channels. It can be seen that 400 sun Silicon CPV cells operate most efficiently with the microgap cooler, achieving a COP_T in the range of 10^5 which decreases as the number of channels is increased. However, increasing concentration ratio to 1000 suns will shift the energetically optimum local maxima to the 5-10 channel range, where a COP_T of 2 x 10^4 is realized. An even higher concentration ratio of 2000 suns sees the COP_T local maxima shift to the 15-20 channel range where the COP_T is about 3000. From these results it is clear that concentration ratios above 400 suns on a Silicon-based CPV cell will require multiple-channel microcoolers in order to operate in their most efficient range.

3.5 Conclusion

This Chapter was on the investigated potential application of a two-phase microcooler for thermal management of a triple-junction concentrated photovoltaic 10mm by 10mm cell, radiated with 2000 suns and cooled with flow boiling of R134a. This effort was extended to Silicon-based CPV's with similar solar loads. The parametric space was explored for optimum solar CPV performance using an energy efficiency metric, COP_T, and the results compared to those achieved with single-phase water cooling. The following conclusions were reached in Chapter 3:

- Triple junction cell performance is largely insensitive to temperature in the

specified operating range of 52C to 69C, with a slight gain of just over 1% (or 1 Watt for the subject CPV cell) in usable solar power.

- Two-phase cooling is found to require low pumping power over most of the quality range of interest. Moreover, pumping losses make up less than a tenth of a watt of the just over 75 W of solar generated power, by a 2000 sun, $100mm^2$ CPV cell, for both single-phase and two-phase cooling, operating at optimal conditions.
- The microcooler Coefficient of Performance (COP) rises with exit quality for two-phase cooling. Therefore, it is energetically advantageous to operate the two-phase cooling system at a flow rate that leads to high exit vapor qualities.
- The highest values of Total Coefficient of Performance (COP_T) 1.77×10^6, representing the least-energy and least-material design, were found to be achieved by a single channel Aluminum microgap configuration in two phase flow.
- Silicon-based CPV under concentrations of 400, 1000, and 2000 suns were investigated and it was found that microgap cooling is optimal for concentrations of 400 suns. Above this concentration ratio, multichannel microcoolers, with between 5 – 15 channels depending on concentration, can provide more efficient cooling up to 2000 suns.

Though it was determined that for triple junction cells parallel microchannels or longitudinal fins, did not generate sufficient additional heat transfer over a single

microgap channel to justify the additional pumping power, it is not clear whether this is generally true for other fin configurations. Since pin fins can have significant wetted area enhancement, it was decided to explore the CPV cooling capability of microgap channels with pin fins. It was found, however, that the existing pin fin correlations in the literature did not cover our parametric range, specifically high exit vapor qualities. Therefore, it was decided to gather new experimental data for this range using our own two phase micro pin fin cooler.

Chapter 4: The Experimental Apparatus

In the present work, two separate Copper micro pin fin arrays of staggered and inline configuration were manufactured on equal overall base areas as well as equal pin width and height, so that performance between the two arrays may be directly compared. In this section, a detailed overview of the testing loop and experimental procedure used to evaluate the thermofluid performance of these micro pin fin channels are discussed.

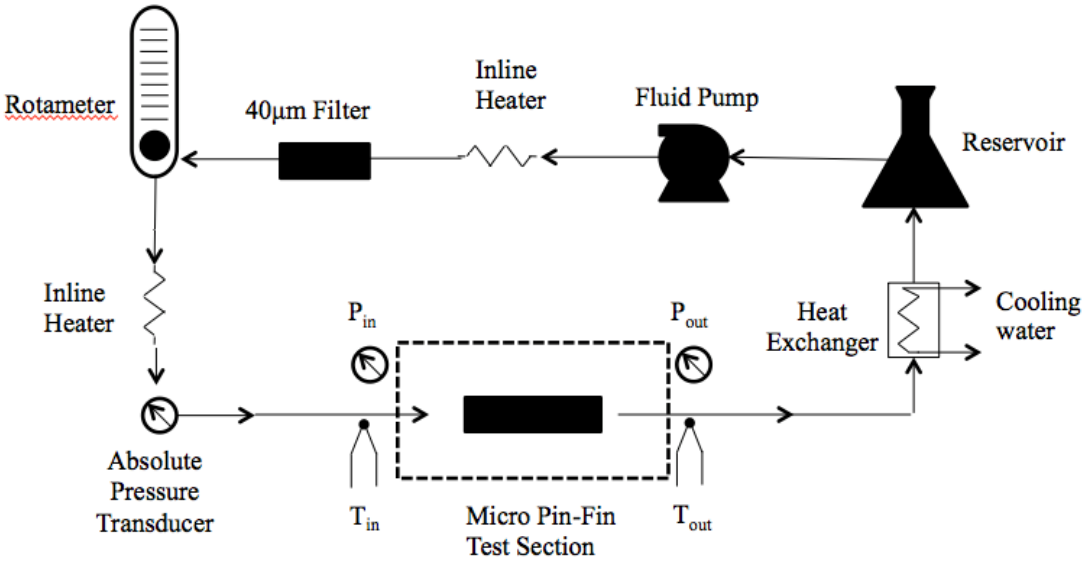

Figure 4.1: Micro-pin-fin testing loop

4.1 General Description

The following devices were used in the experiment: the micro pin fin test section, liquid-cooled condenser, liquid reservoir, fluid pump, rotameter, two inline heaters, inlet and outlet pressure transducers, and various E-type thermocouples for reading fluid and test section temperatures. Semi-transparent, high temperature,

flexible silicone rubber tubing connected all these devices together and provided a robust and easily customizable testing vehicle for the current set-up. A schematic of the testing loop is shown in Figure 4.1.

For pressure readings, two separate transducers were used, one at the inlet and one at the outlet, so that inlet and outlet pressures could be measured independently. This is done so that, along with temperature readings, the level of liquid subcooling, confirmation of saturated boiling condition, vapor quality at the exit, and pressure drop could be calculated and verified.

Two inline preheaters were used to elevate the liquid temperature to the desired inlet value. Two inline heaters were used to gradually heat the fluid to the desired temperature with sufficiently low power in each heater to avoid premature boiling or liquid dryout inside the heaters before reaching the test section.

A McMaster-Carr 40μm inline filter was inserted upstream of the test section to prevent contaminants from clogging the micro pin fins.

The rotameter is an Omega FL-5000 series flow meter with interchangeable tubes. It was installed with a 305cc/minute maximum flow rate tube with 150mm markings. Flow readings are measured visually with the metal ball float, and flow rate can be controlled with the integrated valve.

The condenser is a flat plate heat exchanger, cooled with forced convection water. The flow rate of the cooling water was manually controlled to condense the working fluid and lower the working fluid temperature to the desired value before entering the reservoir.

The pressure transducers were Setra Systems Model 230 with voltage signals between 0.05 and 5.05V. The pressure range for each sensor was 0 – 50psi and 0 – 5psi, for the inlet and outlet sensor respectively. An absolute pressure transducer was used to verify the inlet pressure reading.

4.2 The Micro-Pin-Fin Test Sections

Two micro pin-fin arrays, a staggered configuration and inline configuration,

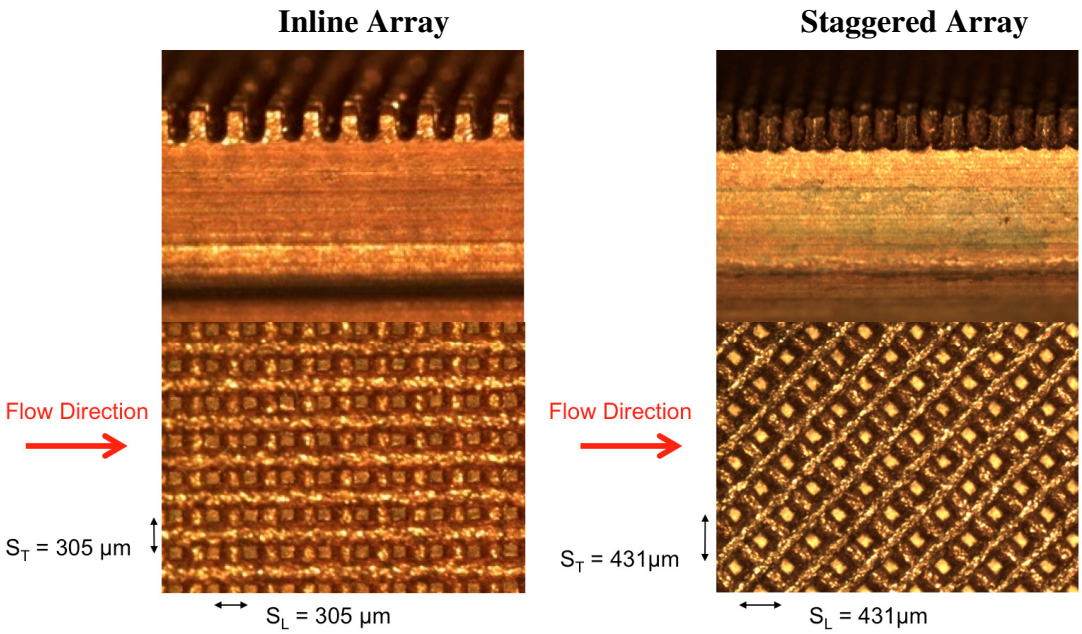

Figure 4.2: Inline and Staggered Pin Fin Arrays

were fabricated out of Copper using a wire electric discharge machining (EDM) process. The arrays were both set to equivalent 0.96cm x 2.88cm base areas and equivalent square pin fin width and height of 153µm and 305µm respectively, so they could be as geometrically similar as possible for performance comparisons. Due to the geometry of the inline and staggered arrays, they have slightly different pin fin pitch or spacing: the transverse and longitudinal spacing are both 305µm for the inline array and 431µm for the staggered array. Figure 4.2 contains a side-by-side visual comparison. On the back of each array, 3 approximately 1 cm^2 square ceramic heaters were soldered using 63% Sn/37% Pb electronic grade solder paste. 10 small holes were drilled above the heated surface where thermocouples were inserted to measure the wall temperature of the test section.

One polycarbonate (Lexan) housing was manufactured to fully enclose the pin fin array being tested, while providing insulation from natural convection heat losses during testing. The housing and pin fin arrays were designed such that easy replacement of test sections could be accomplished as needed with no other modification to the testing loop. On top of the housing, a polycarbonate cover was attached and sealed with silicone RTV. Figure 4.3 is an exploded view of the full assembly.

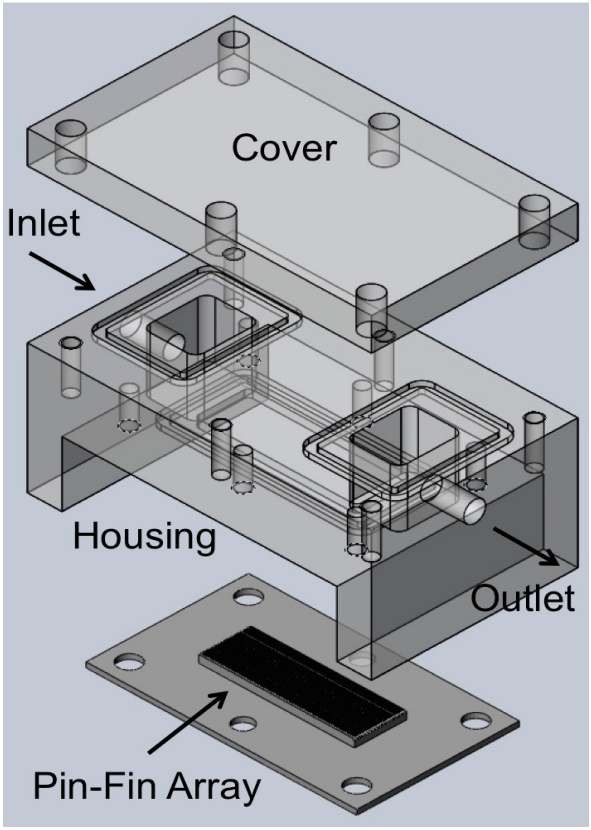

Figure 4.3: Exploded view of test section assembly

4.3 Experimental Testing Procedure

The procedure to obtain single phase data was as follows: the flow rate was set to the desired value using the rotameter. Next the inline preheaters were turned on and set to a power that would yield the inlet temperature for the tests. The heat exchanger cooling water flow was then turned on. A low initial heating level was applied at the test section using the power supply. Heat was increased in small increments for each test and the system was allowed to reach steady state, which took about 2-3 minutes, before data readings were gathered.

The procedure to gather two phase data was similar to the single phase procedure: the flow rate was set to the desired value using the rotameter. The preheaters and heat exchanger cooling water were turned on and the fluid was allowed to reach the desired inlet temperature. Then power was applied at a low level and increased until saturation was achieved at the outlet as confirmed by the temperature and pressure sensors at the channel outlet. The system was allowed to reach steady state for 2-3 minutes then pressure and temperature data were recorded. The heat was then gradually increased by 25 watts and the procedure was repeated.

After all tests with water were completed, the testing loop was drained of all fluid and allowed to dry for several days. Afterward, the testing loop was charged with HFE-7200 and similar testing procedures to water were performed.

Two runs of each mass flux for staggered and inline were run with repeatability in the range of 2% - 5%.

4.4 Error Analysis

To estimate the total measurement uncertainty, a root-sum-square method was applied using the following equation:

$$e_{total} = \sqrt{e_1^2 + e_2^2 + e_3^2 + ... + e_n^2} \qquad (4.1)$$

The error in single phase pressure drop is contributed to by errors in the pressure transducers, the data logger and the rotameter. The following equation can describe the total pressure drop error:

$$\frac{\delta \Delta P}{\Delta P} = \sqrt{\left(\frac{\delta \dot{m}}{\dot{m}}\right)^2 + \left(\frac{\delta V_{out}}{V_{out}}\right)^2 + \left(\frac{\delta \Delta P_{trans}}{\Delta P_{trans}}\right)^2} \qquad (4.2)$$

where $\delta \Delta P$ is the pressure drop measurement uncertainty, $\delta \dot{m}$ is the rotameter uncertainty (±3% full scale), δV_{out} is the data logger output DC voltage error (0.05%) and $\delta \Delta P_{trans}$ is the pressure transducer error (±0.25% full scale). The resulting total pressure drop measurement error was found to be 3%.

Uncertainty in the heat transfer coefficient is based on the flow rate, power supply instability, wall temperature and inlet and outlet temperature. Since the single phase heat transfer coefficient is obtained from:

$$h = \frac{q}{A\Delta T} \qquad (4.3)$$

it follows, then, that the heat transfer rate is obtained from a total energy balance:

$$q = \dot{m} C_p \left(T_{out} - T_{in} \right) \qquad (4.4)$$

Using Equation 4.4 an error for the heat transfer coefficient can be estimated using Equation 4.1:

$$\frac{\delta h}{h} = \sqrt{\left(\frac{\delta \dot{m}}{\dot{m}} \right)^2 + \left(\frac{\delta q}{q} \right)^2 + \left(\frac{\delta \Delta T_{wall}}{\Delta T_{wall}} \right)^2 + \left(\frac{\delta \left(T_{out} - T_{in} \right)}{\left(T_{out} - T_{in} \right)} \right)^2} \qquad (4.5)$$

δh is the uncertainty of the heat transfer coefficient, $\delta \dot{m}$ is the rotameter uncertainty ($\pm 3\%$ full scale), δq is the uncertainty in the power supply (0.071%), $\delta \Delta T_{wall}$ is the error in measurement of the difference between the wall temperature and fluid temperature and

$\delta(T_{out} - T_{in})$ is the measurement error of the fluid temperature. Since fluid property error of HFE-7200 could not be obtained and water property error is assumed negligible, the fluid property uncertainty was not taken into account.

The temperature measurement errors for both ΔT_{wall} and T_{out}-T_{in} are based on the uncertainty in the E-type thermocouples used, which have a 1°C uncertainty. The error in ΔT wall can then be estimated using the lowest measured excess wall temperature, which was 8°C. Therefore: 1°C/8°C = 12.5%. The error in T_{out}-T_{in} can be estimated similarly and was found to be 10% since the lowest temperature between inlet and outlet was measured at 10°C.

The maximum measurement error in single-phase heat transfer coefficient was calculated and found to be 16.3%.

To estimate heat losses to the ambient, the test section and housing were drained of fluid and allowed to dry fully. Low power was applied to the heaters, and the dry test section and housing were heated to steady-state which took approximately 20-30 minutes depending on power level. For each power increment, thermocouple temperatures were recorded. The tests were repeated for increasing power increments, up to thermocouple temperature readings of 138°C. A linear equation for heat loss - which had an uncertainty of less than 0.01% - was formed based on measured temperatures and supplied power. The resulting heat losses were subtracted from the total supplied power to the heaters. Heat losses to ambient were found to be less than 5% of supplied power for all experiments.

Chapter 5: Single Phase Micro Pin-Fin Experiments

5.1 Introduction

Single phase experiments were performed with deionized water and HFE-7200 in both the staggered and inline arrays. The tests established a baseline to which the available correlation could be compared, as well as to gauge the relative cooling performance enhancement for the two phase flow boiling experiments. Inlet temperature for all single phase experiments was held constant at 30°C.

5.2 Average Heat Transfer Coefficient

Plots of single phase average heat transfer coefficient versus heat flux for both deionized water and HFE-7200, in the in-line and staggered arrays, are given in this section. Results were corrected for fin efficiency, and the average heat transfer coefficient is based on the total wetted area of the channel.

Deionized Water Experimental Results

In Figures 5.1 and 5.2, the results for deionized water in the in-line array and staggered array are shown for 4 different mass fluxes from 400 kg/m^{2}s to 1300 kg/m^{2}s, with heat fluxes in the range of 10 to 110 W/cm^2. Error bars in the Figures indicate ±16%. It can be seen that while the average heat transfer coefficient is almost independent of heat flux (zero slope) for constant flow rate, a 3x increase of mass flux will cause the average heat transfer coefficient to increase by about 2x. Additionally, it can be seen that the in-line and staggered arrays are similar in magnitude for

equivalent mass fluxes, with the inline array slightly better except for the highest 1300 kg/m^{2}s mass flux.

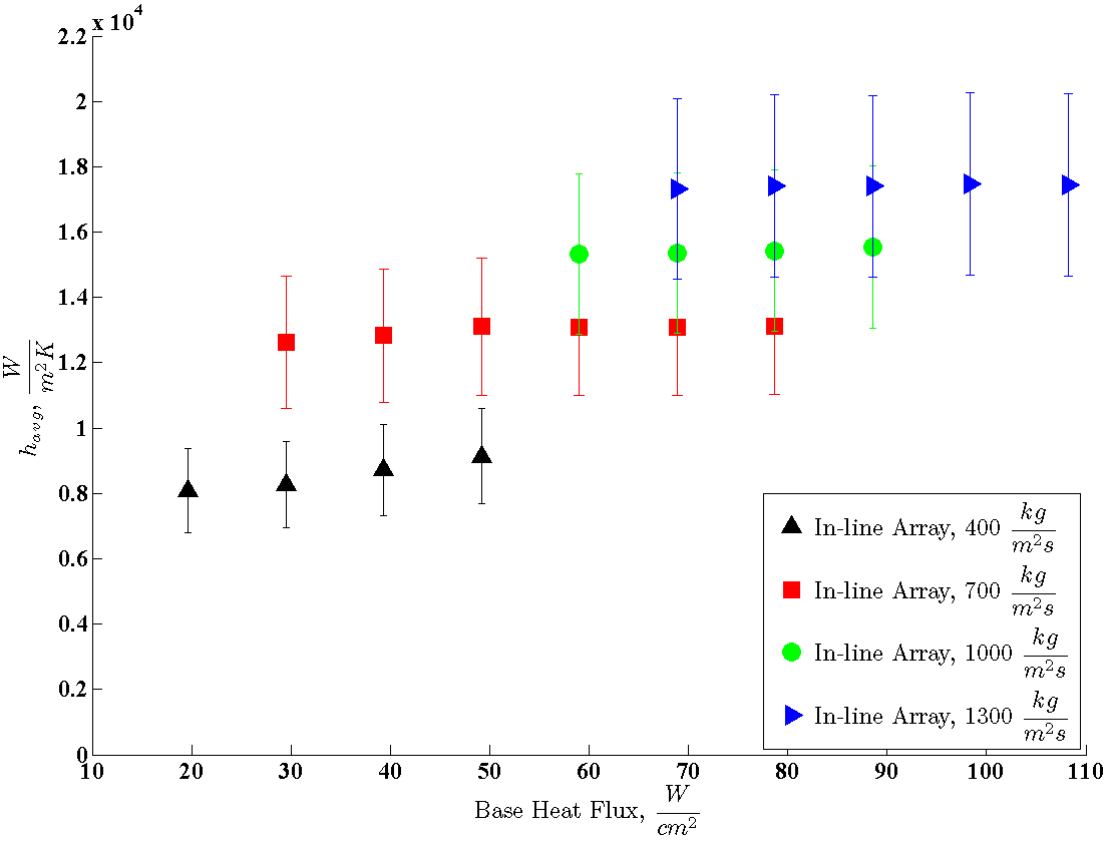

Figure 5.1: Single phase water average heat transfer coefficient vs. base heat flux for the inline array. Error bars indicate ±16%.

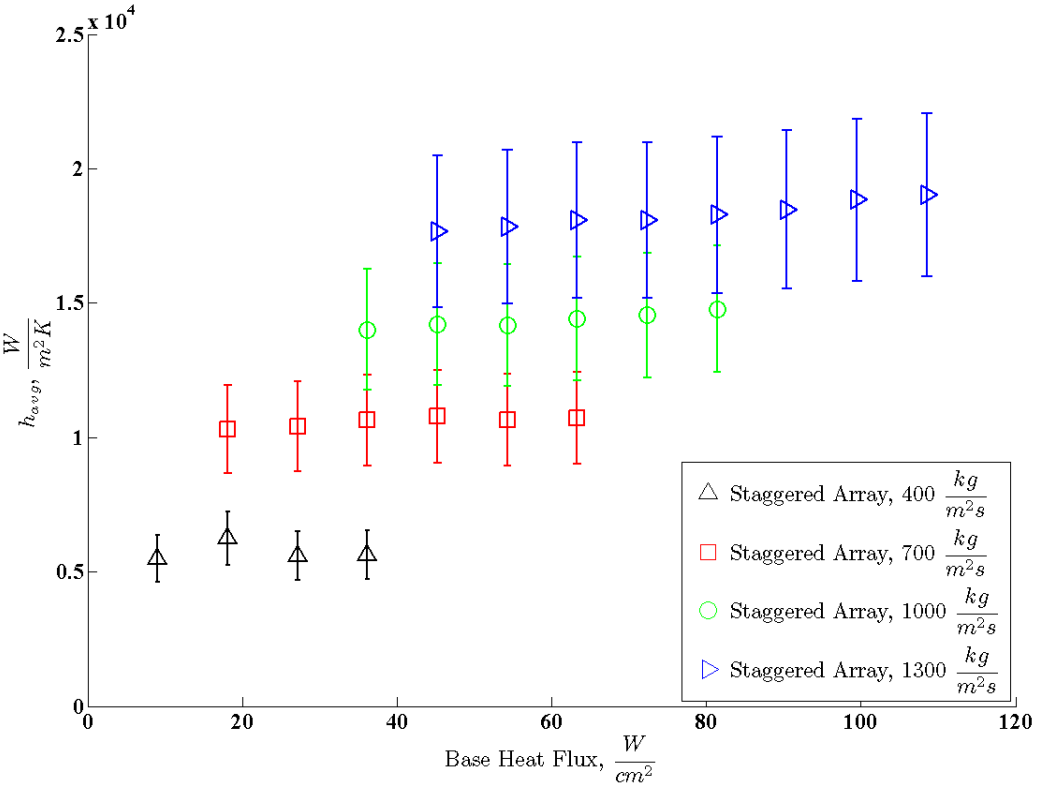

Figure 5.2: Single phase water average heat transfer coefficient vs. base heat flux for the staggered array. Error bars indicate ±16%.

Comparison to the Literature

Figure 5.3 shows the Tullius et al. correlation prediction (solid line) for the inline and staggered arrays using the square and diamond shape factor multipliers of 0.0937 and 0.036 respectively. Significant mean average error (MAE) between the correlation and data of 87.52% overall for the inline array occurs, while better MAE of 16.09% is seen for the staggered array. This result is compared to the reported MAE of 9% by Tullius et al. Since the current data for the parametric range of Tullius

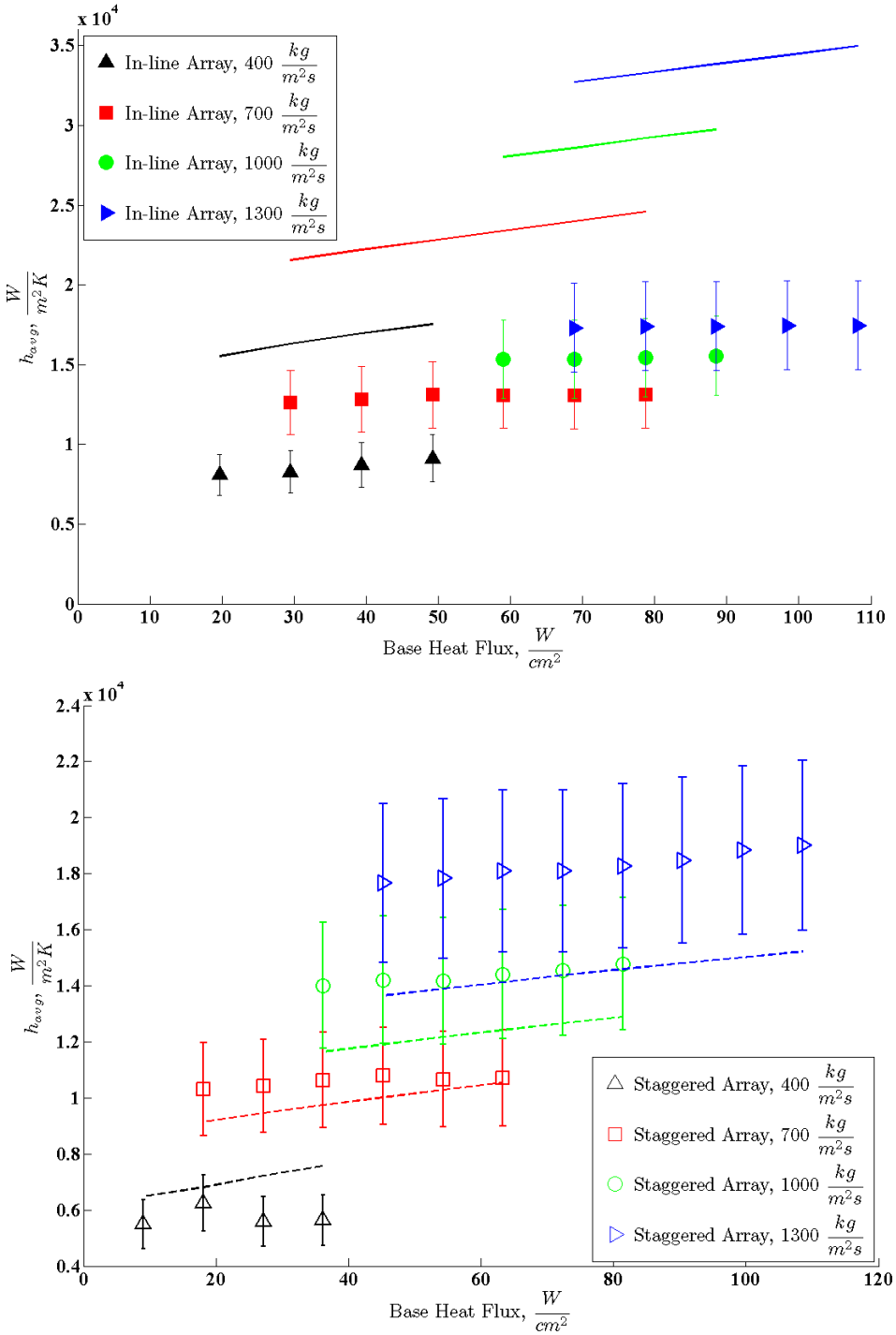

Figure 5.3: Tullius et al. prediction for single phase water in the inline array (top) using a square shape factor of 0.0937 and staggered array (bottom) using a diamond shape factor of 0.036

et al. is within range for the staggered array, the better accuracy is not unexpected.

However, since the correlation was developed for staggered arrays, the higher MAE

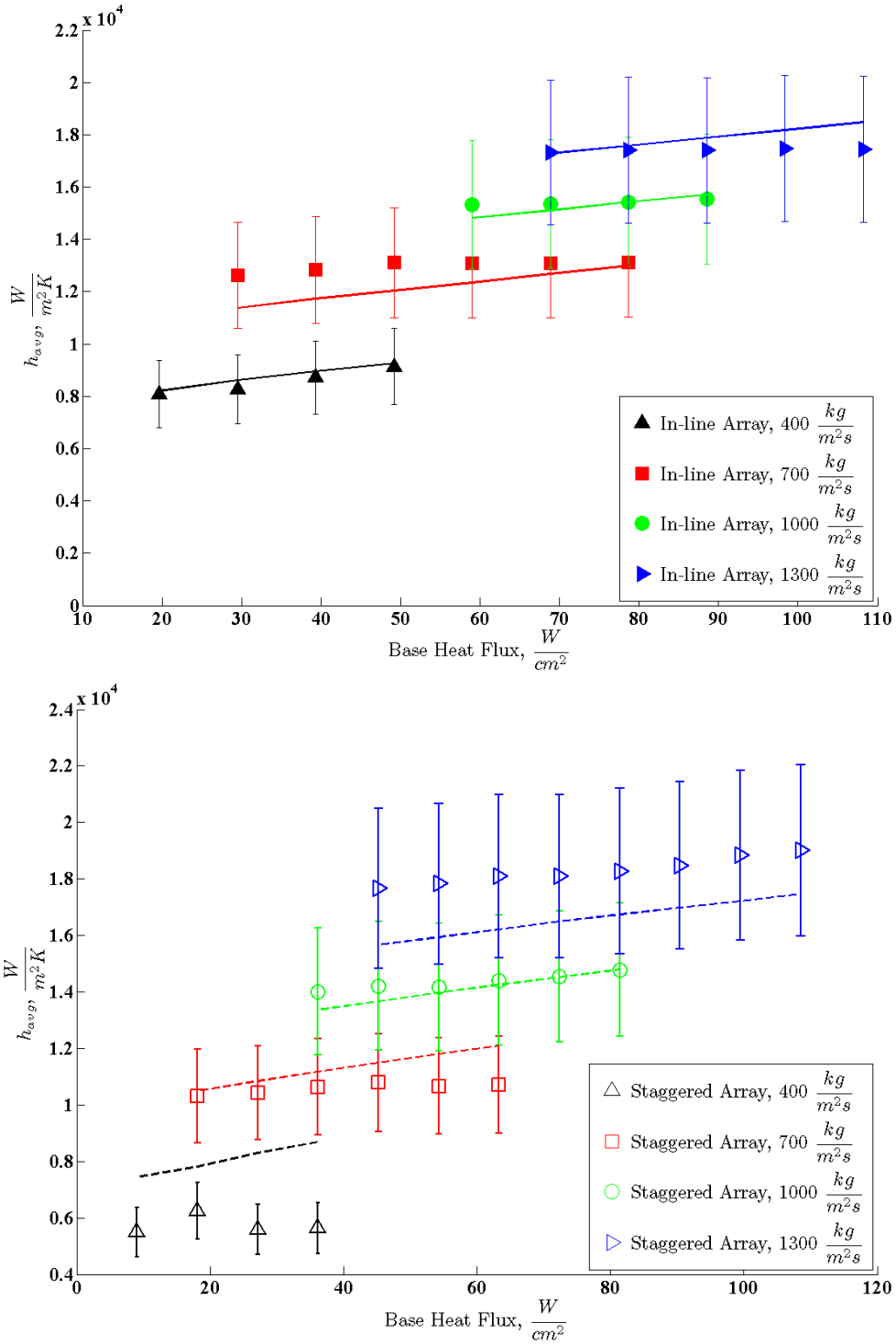

Figure 5.4: Improved Tullius et al. prediction for single phase water in the inline array (top) using a 0.0495 shape factor and the staggered array (bottom) using a 0.0413 shape factor.

of 88% for the inline array is expected due to being outside of the stated parametric

range. Interestingly, the accuracy of the correlation can be improved to 3.48% for the inline array by using a shape factor of 0.0495, and 12.07% for the staggered array by using a shape factor of 0.0413. These values are within range of the published shape factors. The improved correlation is shown in Figure 5.4.

HFE-7200 Experimental Results

The results for HFE-7200 average heat transfer coefficient versus heat flux for the in-line and staggered arrays are shown in Figures 5.5 and 5.6 respectively for 3 different mass fluxes from 200 kg/m^{2}s to 600 kg/m^{2}s. Error bars indicate ±16%. Similar to water, a 2x improvement in the average heat

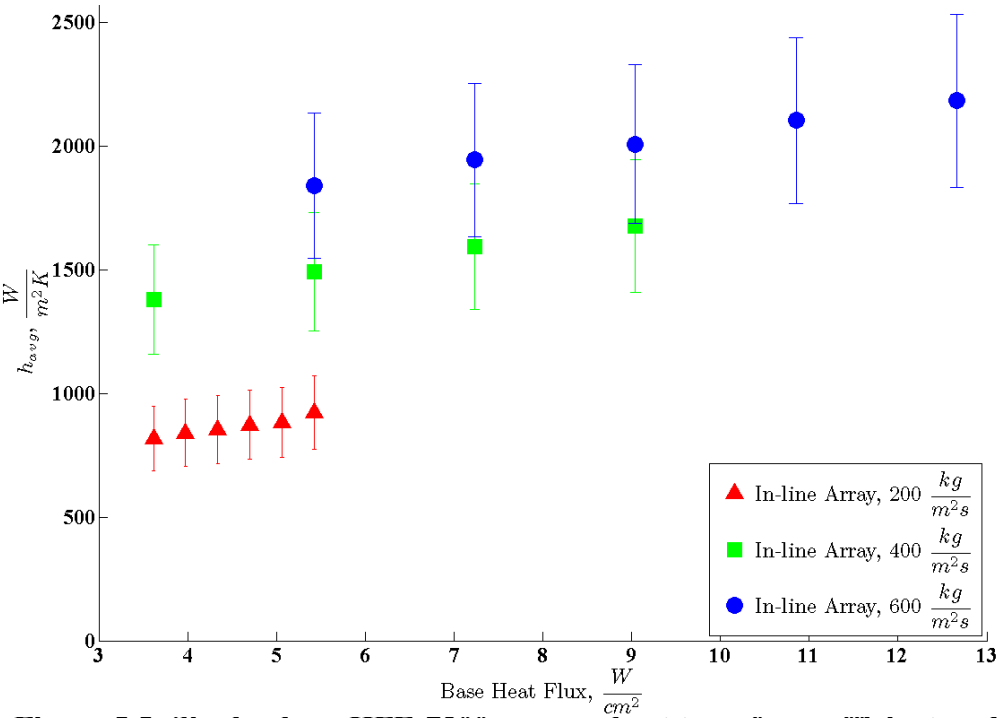

Figure 5.5: Single phase HFE-7200 average heat transfer coefficient vs. base heat flux for the inline array. Error bars indicate ±16%

transfer coefficient occurs for 3x increasing mass flux. However, the magnitude is lower than water due to HFE-7200's relatively lower cooling performance. The slope is less flat than for the single phase water data, with a slightly increasing trend of average heat transfer coefficient over base heat flux.

The staggered array improves over the inline array at the same mass flux by about 30%-50% for the two highest mass fluxes. Additionally, a larger 3x improvement in the average heat transfer coefficient occurs for a 3x increasing mass flux and it appears to display a more complex dependence on heat flux than seen with water.

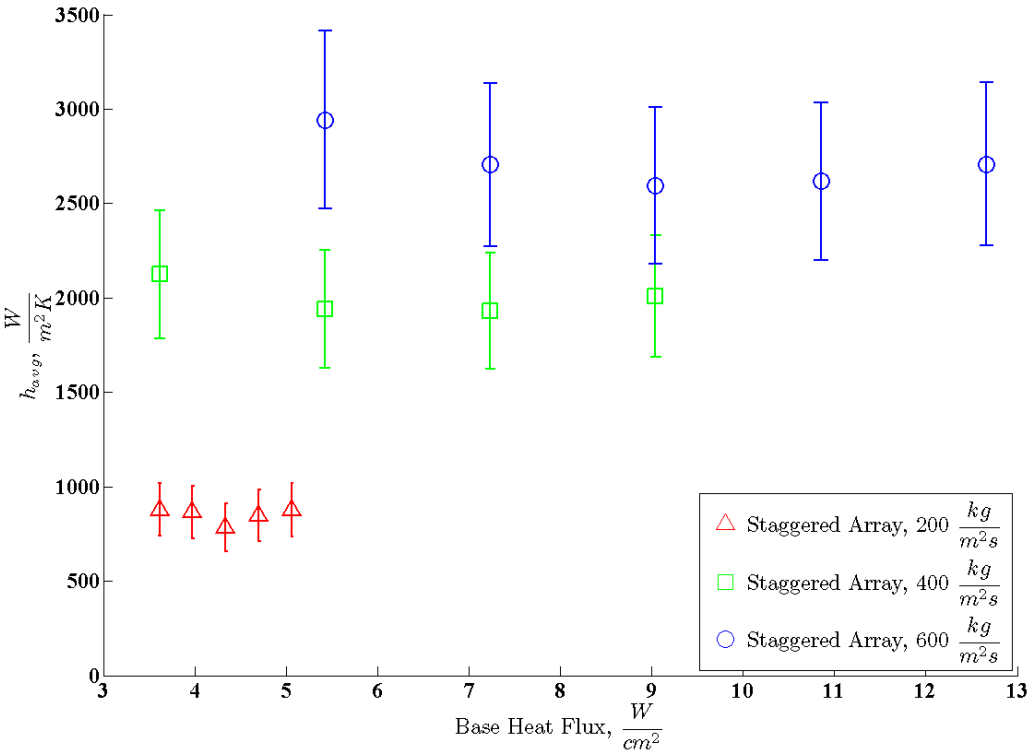

Figure 5.6: Single phase HFE-7200 average heat transfer coefficient vs. base heat flux for the staggered array. Error bars indicate ±16%

Comparison to the Literature

Figure 5.7 shows the Tullius et al. correlation prediction (solid line) for the inline and staggered arrays using the square and diamond shape factor multipliers of 0.0937 and 0.036 respectively. Displaying relatively high MAE between the correlation and data of 70.47% overall for the inline, and 36.49% for the staggered array. The accuracy of the correlation can be improved to 9.28% for the inline array by setting the shape factor to 0.054, and 23.35% for the staggered array by setting the shape factor to 0.065. The improved correlation is presented in Figure 5.8.

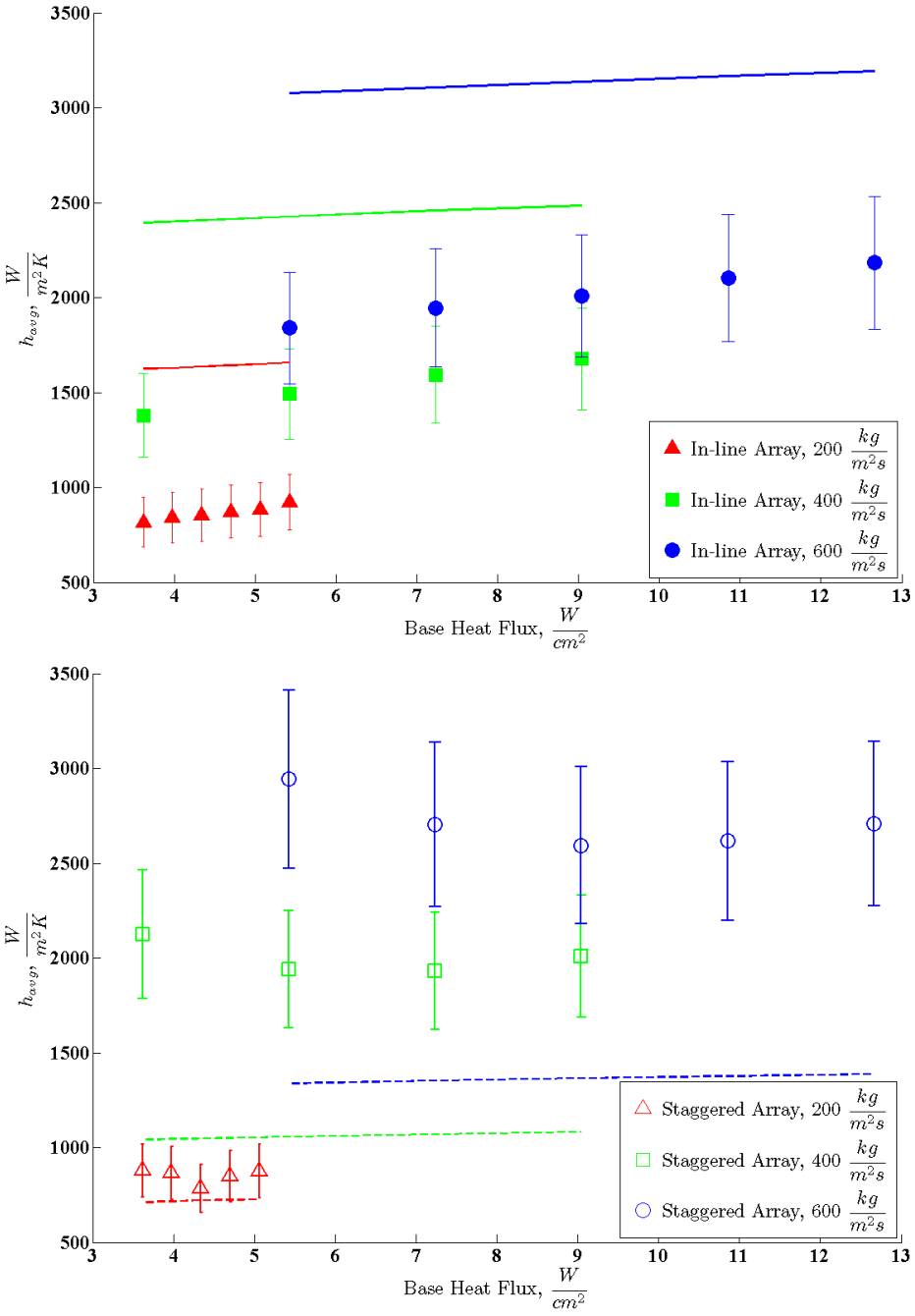

Figure 5.7: Tullius et al. prediction for single phase HFE-7200 in the inline array (top) using a square shape factor of 0.0937 and staggered array (bottom) using a diamond shape factor of 0.036

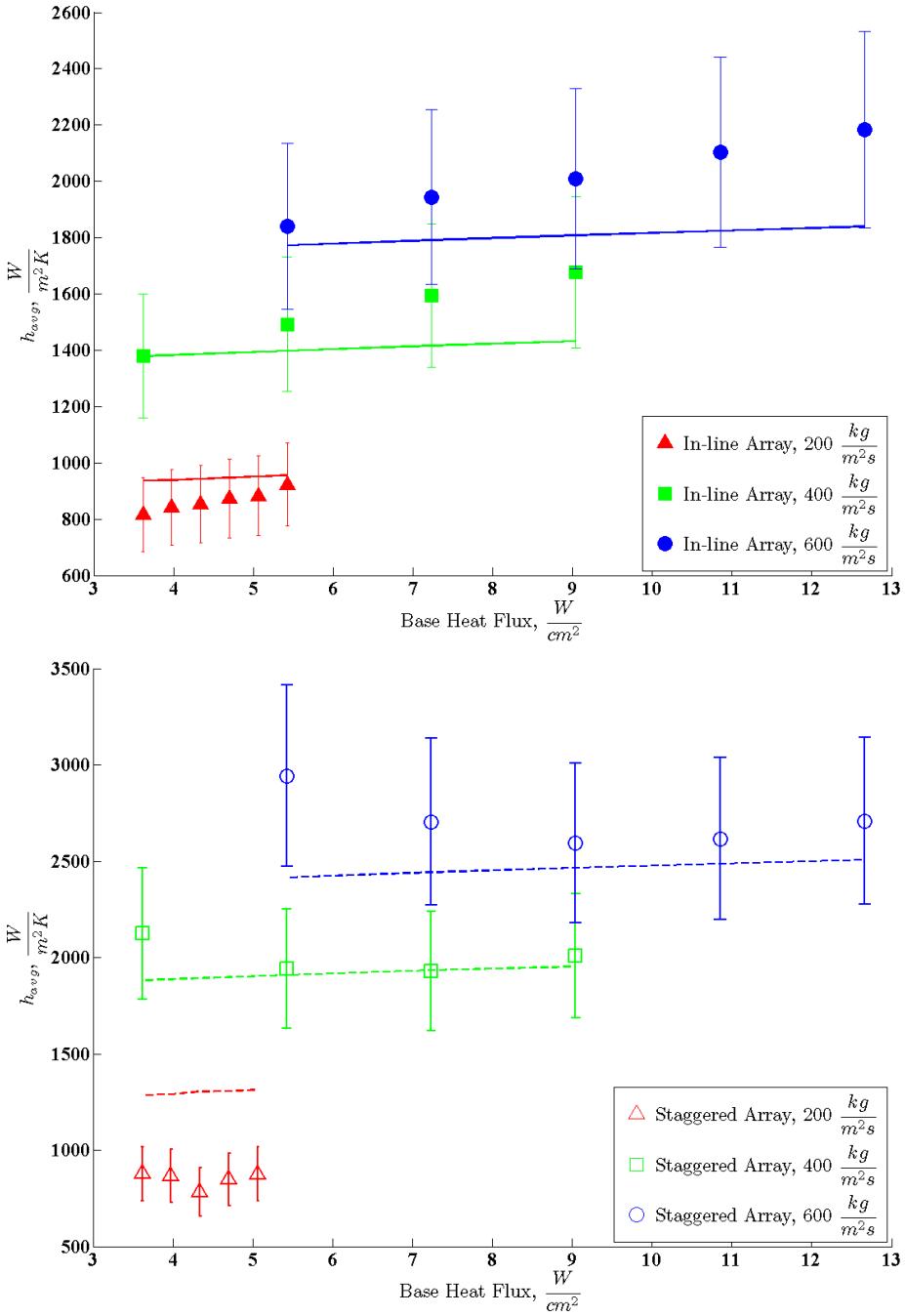

Figure 5.8: Improved Tullius et al. prediction for single phase HFE-7200 in the inline array (top) using a 0.054 shape factor and the staggered array (bottom) using a 0.065 shape factor.

5.3 Adiabatic Pressure Drop

Plots of adiabatic pressure drop vs. flow rate for both deionized water and HFE-7200, in the in-line and staggered arrays, is given in this section.

Figure 5.9 shows the pressure drop versus flow rate for deionized water in both arrays. Error bars indicate ±3%. The staggered array is seen to have higher pressure drop than the inline at the same flow rate. The difference in pressure drop between the two arrays becomes larger at increasingly high flow rates due to the tortuous flow path of the fluid in the staggered array.

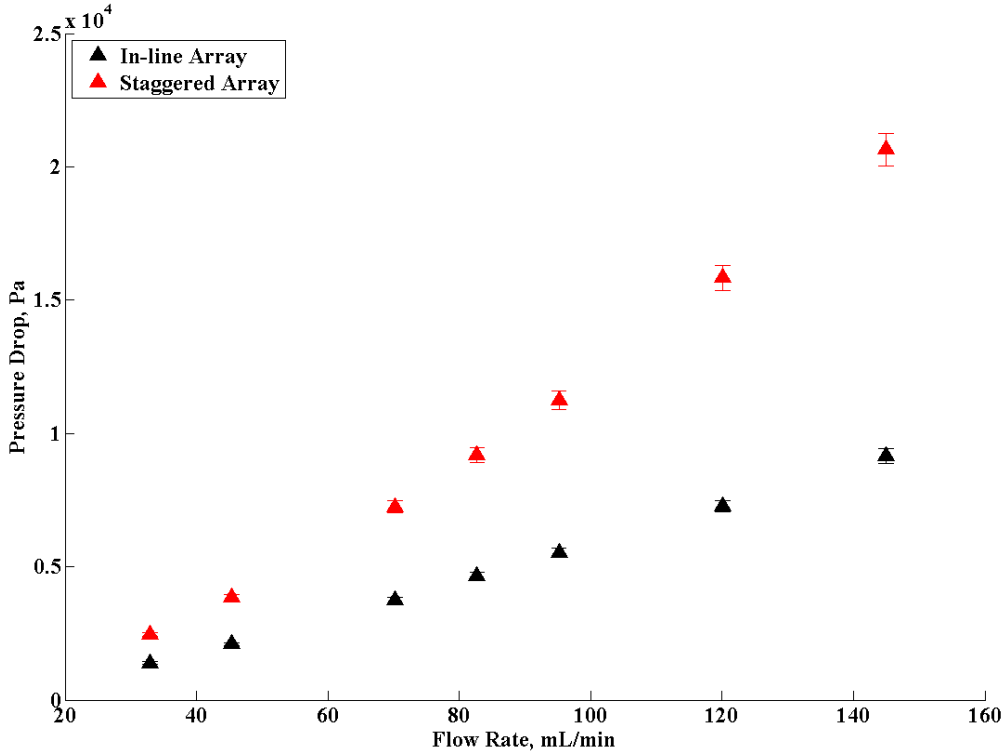

Figure 5.9: Single phase water adiabatic pressure drop vs. flow rate for the inline and staggered arrays. Error bars indicate ±3%.

Interestingly, for Figure 5.10 the same result does not occur for HFE-7200: the pressure drop is essentially the same between the two arrays. This result could be

due to lower flow rates and thus the low Reynolds number flow. Whether the array is staggered or inline is almost insignificant for adiabatic pressure drop at low flow rates for HFE-7200.

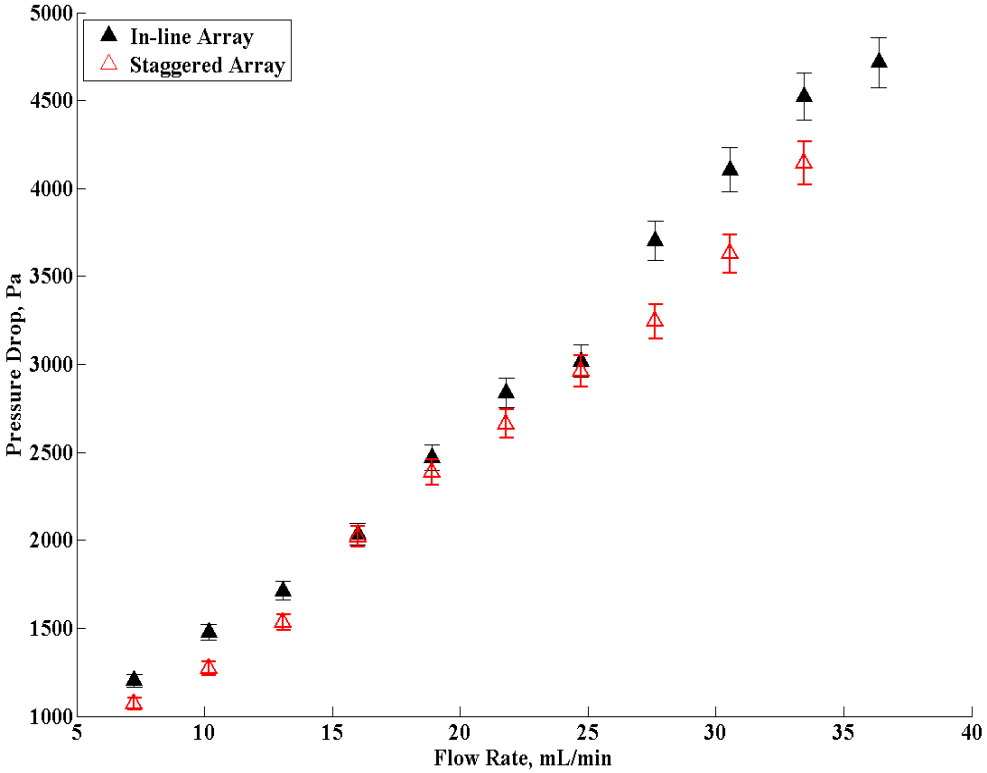

Figure 5.10: Single phase HFE-7200 adiabatic pressure drop vs. flow rate for the inline and staggered arrays. Error bars indicate ±3%.

Comparison to the Literature

Shown on the top plot of Figure 5.11 is the same water data from Figure 5.9, with the Tullius et al. pressure drop correlation prediction (solid lines). Using the correlation as outlined in Chapter 2.3, and using the square shape factor, 5.28, for the inline array and the diamond shape factor, 1.81, for the staggered array, MAE's of 748% and 128% are obtained. The prediction accuracy is greatly improved to 11.35%

and 4.74% MAE by using optimized shape factors of 0.62 and 0.78 for the inline and staggered array, respectively. This result is unexpected, since the parametric range for the water data is within the range of the Tullius et al. correlation. It may be possible that this is an discrepancy with the pressure drop correlation that can not be explained and which will require further study to discover the possible reason for the disagreement with the data. See the bottom picture of Figure 5.11 for the improved correlation.

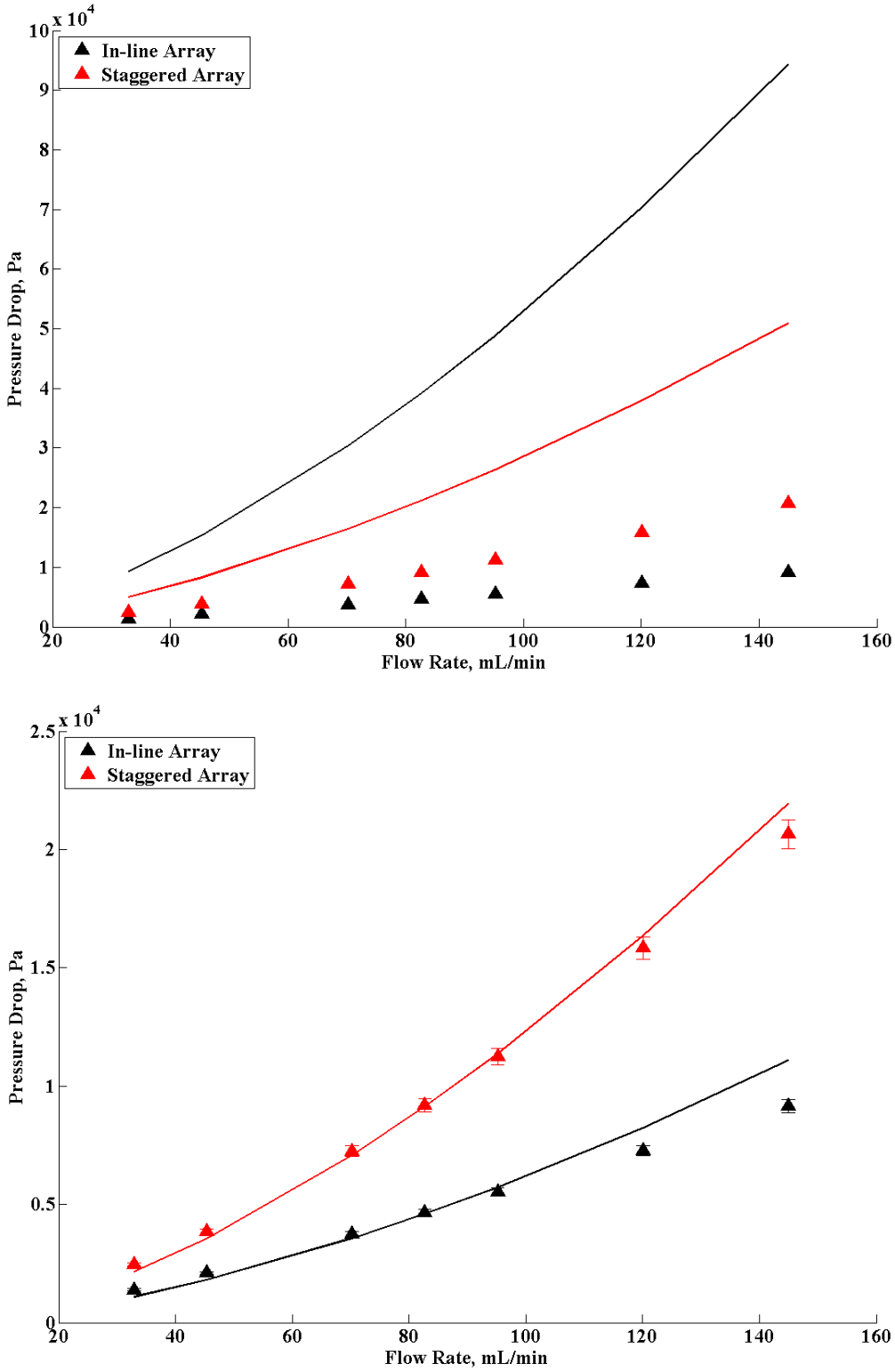

Figure 5.11: Tullius et al. prediction of pressure drop for single phase water in both arrays (top). Improved Tullius correlation for pressure drop in both arrays (bottom). Error bars ±3%

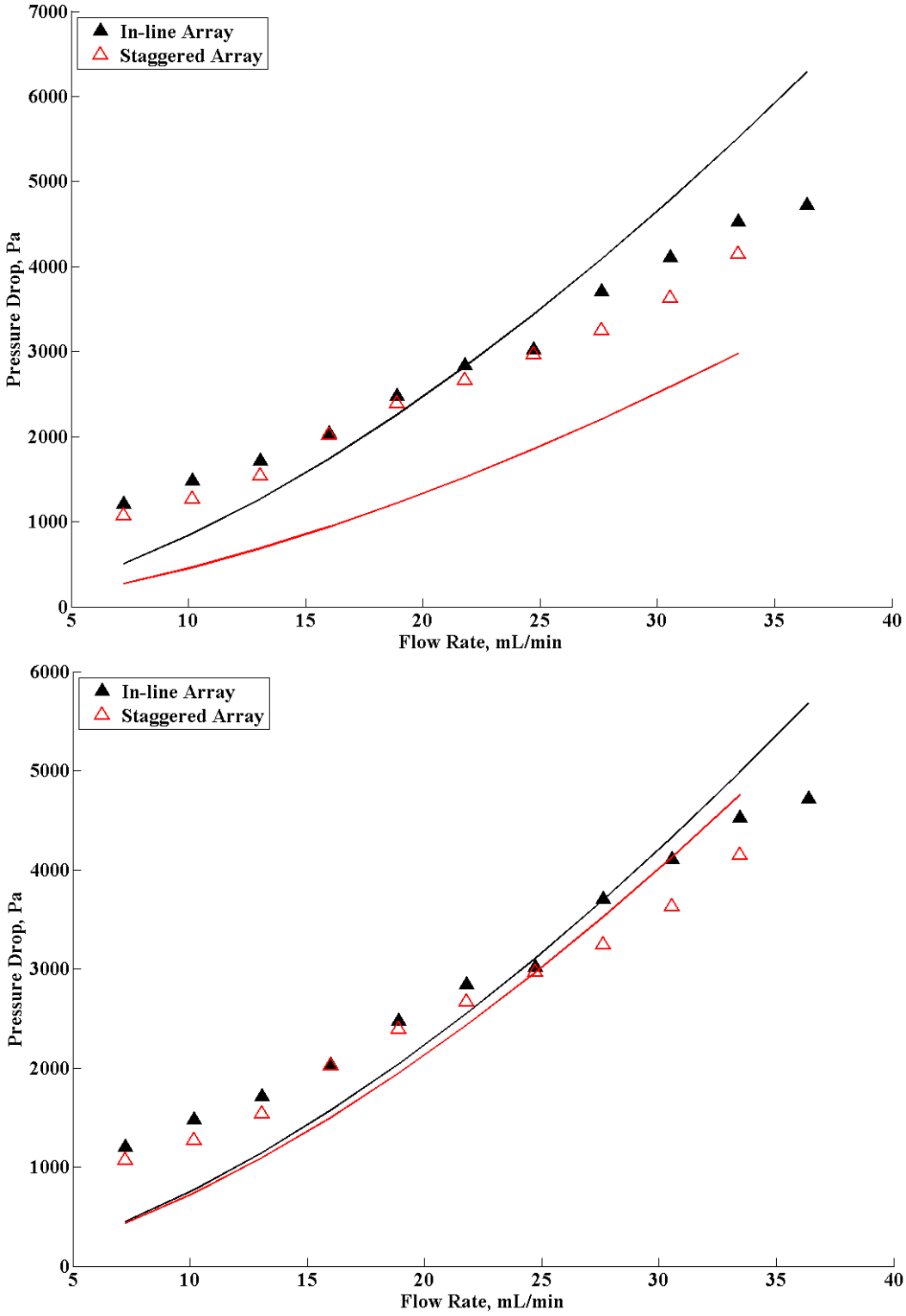

Figure 5.12: Tullius et al. prediction for pressure drop for single phase HFE-7200 in both arrays (top). Improved Tullius correlation for pressure drop in both arrays (bottom)

Shown on the top plot of Figure 5.12 is the HFE-7200 data from Figure 5.10, with the Tullius et al. pressure drop correlation prediction (solid lines). Using the correlation as outlined in Chapter 2.3, and once again using the square shape factor, 5.28, for the inline array and the diamond shape factor, 1.81, for the staggered array, MAE's of 22.36% and 46.5% are obtained. The prediction accuracy is improved to 21.1% and 22% MAE by using shape factors of 4.77 and 2.89 for the inline and staggered array, respectively. See the bottom plot of Figure 5.12 for the improved correlation.

Chapter 6: Two Phase Micro Pin-Fin Experiments

6.1 Introduction

Two phase flow boiling experiments were performed with deionized water and HFE-7200 in both the staggered and inline arrays. The goals of the experiments were as follows: to ascertain the cooling enhancement that two phase flow boiling could provide over the single phase baseline, with a particular emphasis on performance at high exit vapor qualities. No micro pin fin data exist in the literature for exit qualities above 30%. Thus, evaluating the accuracy of the existing two phase correlations for prediction at high exit qualities was an essential goal of the experiments and the results would support the determination of the best pin fin configuration for energy efficient cooling at the high heat fluxes that are encountered in a CPV array. In the following sections, the two phase cooling experiments are described along with a comparison of the results to those available in the existing literature.

6.2 Average Heat Transfer Coefficient

Plots of two phase average heat transfer coefficient versus exit quality for both deionized water and HFE-7200, in the in-line and staggered arrays, are given in this section. A comparison with the literature is then presented. Results were corrected for fin efficiency, and the average heat transfer coefficient is based on the total wetted area of the channel.

Deionized Water Experimental Results

Water entered the test sections at about 95°C, keeping the subcooling low so as to subsequently allow exit qualities to be as high as possible, while keeping surface temperatures below 140°C to prevent thermal destruction of the testing apparatus or any components.

Figure 6.1 is a plot of the two phase water average heat transfer coefficient versus heat flux for the inline and staggered arrays for 4 different mass fluxes from 400 kg/m^{2}s to 1300 kg/m^{2}s and heat flux from 27 W/cm^2 to 118 W/cm^2. Error bars indicate ±16%. When plotted against heat flux, average heat transfer coefficient appears independent of mass flux and increases with heat flux. The reason for this behavior is unknown, therefore, for a more complete and accurate picture, further

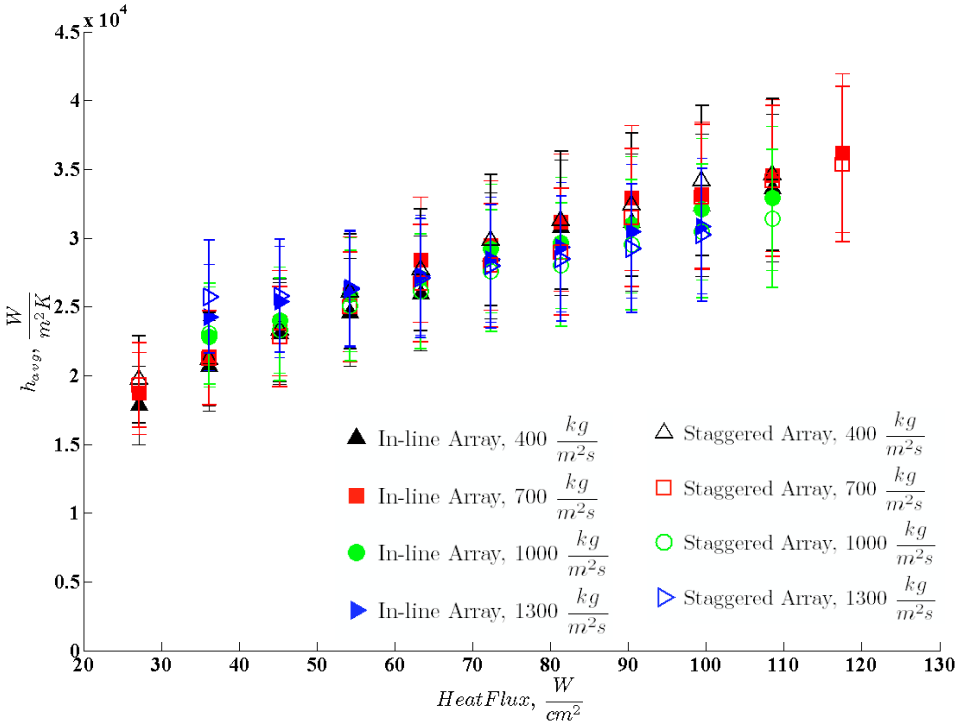

Figure 6.1: Average two phase heat transfer coefficient versus heat flux for water in the staggered and inline pin fin arrays. Error bars indicate ±16%.

work via visualization and a flow regime study will be needed to understand the micro pin fin flow patterns and regime transition points.

Next, the same data from Figure 6.1 is plotted in Figure 6.2, but this time against exit quality on the x-axis. It is easier to see distinct trends for each mass flux, with heat transfer coefficient at the same exit quality increasing with mass flux.

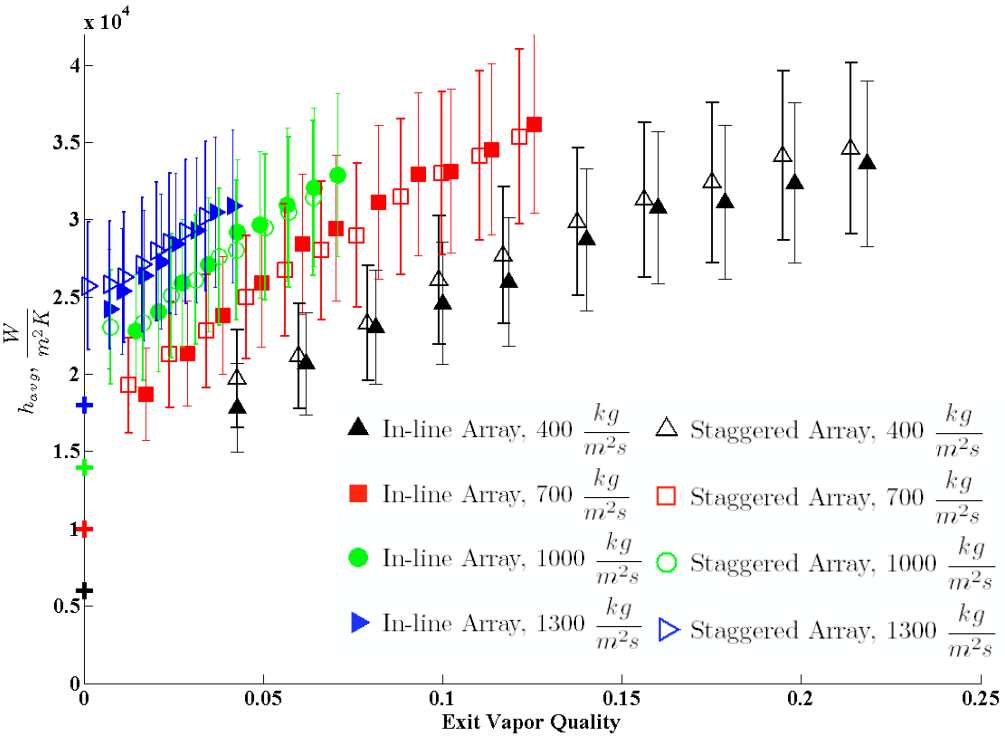

Figure 6.2: Average two phase heat transfer coefficient versus exit quality for water in the staggered and inline pin fin arrays. Error bars indicate ±16%. "+" marks indicates single phase asymptote.

Also, as exit quality is increased, the average heat transfer coefficient monotonically increases, with all data points better than the respective single phase asymptote marked on the y-axis at 0% exit quality. It is also important to note that the inline and staggered data points nearly coincide over the entire range of qualities shown here, implying that neither the inline or staggered array is significantly better than the other in terms of cooling performance.

Comparison to the Literature

In Figure 6.3, comparison of the current water data with the available two phase correlations outlined in Chapter 2.4 reveal the large differences in the trend and magnitude of the predicted heat transfer coefficients among these correlations. While the heat transfer coefficients are observed to generally increase with exit quality in this parametric range, the Qu and Siu-Ho correlation displays a nearly "quality-independent" behavior with a slight downward trend of the heat transfer coefficients with quality, having an MAE of 118% for inline and 129% for staggered. Parametrically, working fluid, heat fluxes, mass fluxes along with Prandtl and Reynolds number are within range of the Qu and Siu-Ho correlation, however their high inlet subcooling and staggered square pin fin geometry is substantially different from the current pin fin array experiments. The McNeil et al. correlation has a trend similar to the data but substantially overpredicts the empirical results with an MAE of 363% for inline and 351% for staggered. The overprediction by McNeil et al. could be explained by, not only the larger 1mm x 1mm pin fins used in their experiments, but also the R113 refrigerant working fluid that was used. The correlation with the best overall prediction capability for these empirical results is by Krishnamurthy and Peles with an MAE of 109% for inline and 144% for the staggered configuration. Once more, similar geometric deviations occur with the circular, staggered pin fin array used for the Krishnamurthy and Peles correlation. Additionally, the inlet subcooling was much higher than for the current work. These discrepancies are

substantially beyond the ±16% error bars indicated in Figure 6.3 and cannot be explained by experimental uncertainty alone.

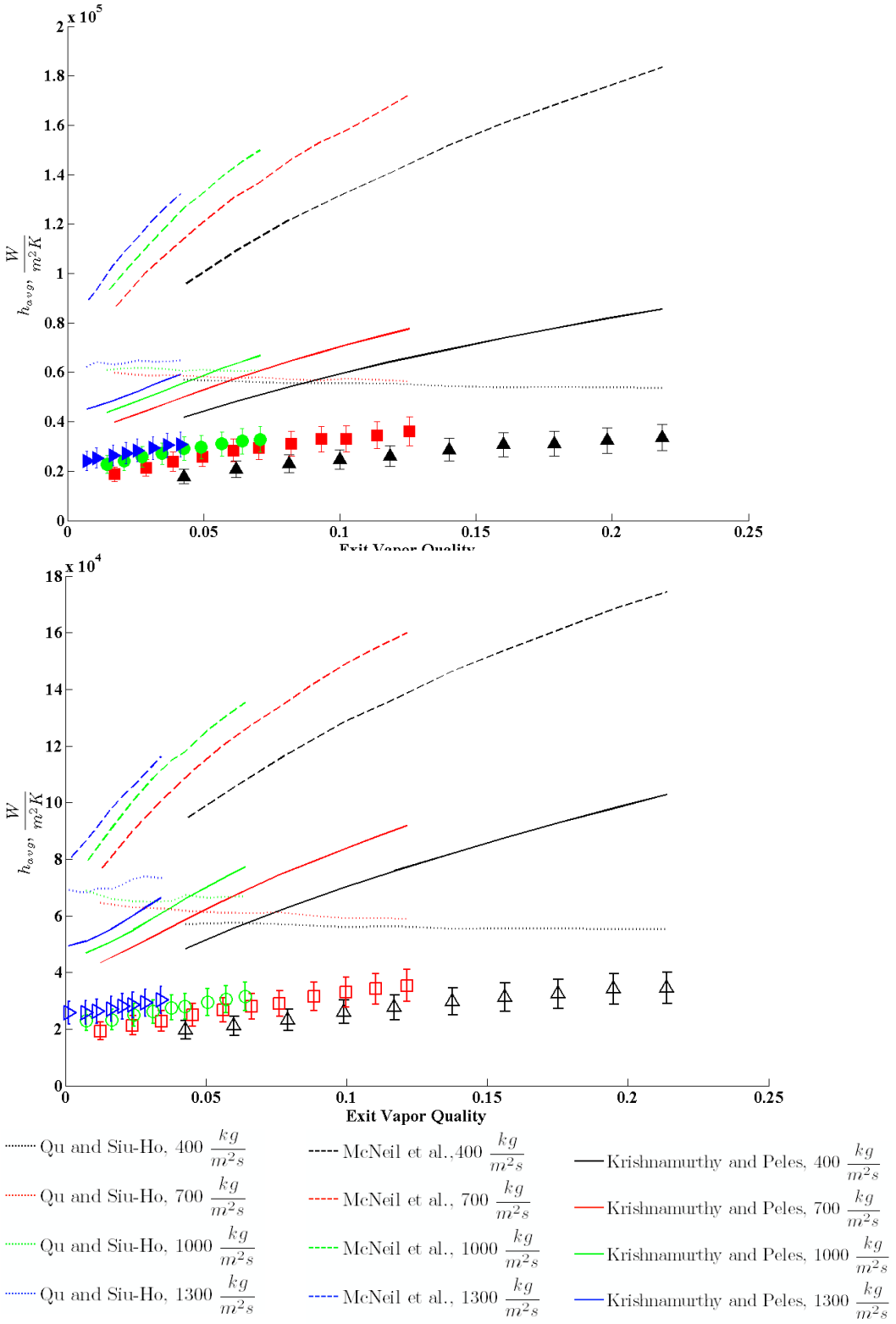

Figure 6.3: Comparison of average two phase heat transfer coefficient for water in the inline array (top) and staggered array (bottom), to the current correlations available in the open literature. Error bars indicate ±16%.

HFE-7200 Experimental Results

HFE-7200, with a boiling point of 76°C at atmospheric pressure, entered the pin fin array at 70°C, keeping the level of subcooling low to allow the exit qualities to be as high as possible. Also, the same 3 constant mass fluxes of 200 kg/m^{2}s, 400 kg/m^{2}s and 600 kg/m^{2}s from the previous single phase HFE-7200 experiments were

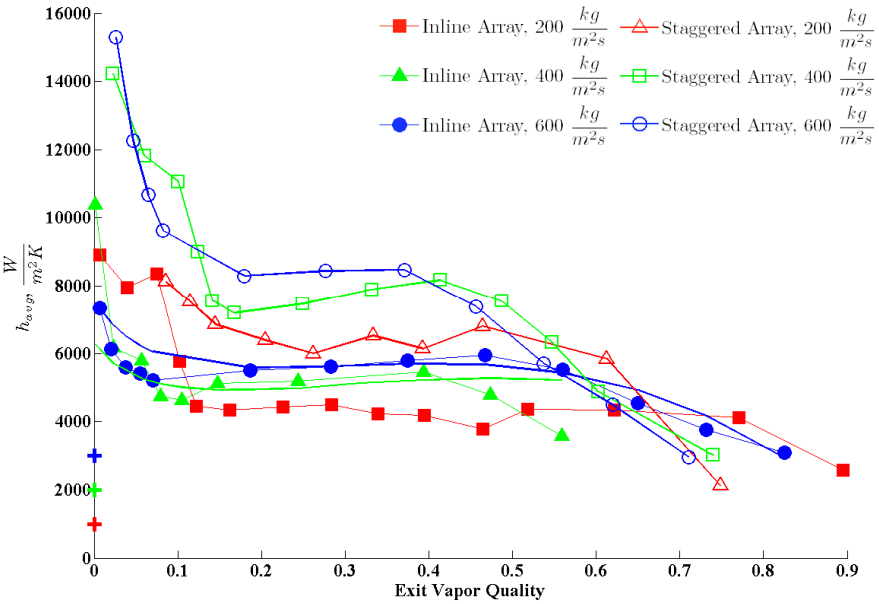

Figure 6.4: Average heat transfer coefficient vs. exit quality for two phase HFE-7200 in the inline and staggered arrays. "+" markings indicate single phase asymptote.

chosen. Heat fluxes ranged from 1 W/cm^2 to 36 W/cm^2. Due to the low latent heat of the HFE-7200, the experiments spanned a broader range of exit qualities, exceeding 70% for all the experiments and reaching a maximum value of 90% for the in-line pin fin array operating at a 200kg/m^{2}s mass flux. Inspection of Figure 6.4 immediately reveals distinct differences between the plots of two phase HFE-7200 heat transfer coefficients and the water data in Figure 6.2. Unlike the observed behavior with

water, the HFE-7200 data reveals an approximately 50% improvement in the average heat transfer coefficient of the staggered array over the inline array, for much of the range of exit qualities. Most notable for both HFE-7200 array configurations however, is the initial sharp decline in the average heat transfer coefficient from the lowest exit qualities to about 10% - 15%, followed by a plateauing or mild increase up to exit qualities of 40% - 50% where it reaches a local maximum. Finally, the average heat transfer coefficient deteriorates as the exit quality approaches 100%, possibly reflecting localized dryout in the pin fin array. It should be noted that the two phase heat transfer coefficients exceed that of the single phase asumptote ("+" markings on plot) over the entire exit quality range, for all mass fluxes. Additionally, the ±16% measurement error bars were left out of Figure 6.4 for clarity.

The observed variation of the heat transfer coefficient with quality is reminiscent of the trends described previously in microgap flow boiling experiments by Rahim et al. [27]. Though it was suggested by Krishnamurthy and Peles that there may be flow regimes unique to micro pin fin arrays, such as bridge-flow [35], the observed trend in this study is analogous to that occurring in microgaps and microchannels, and may thus be explained by the general physics of two phase phenomena in microchannels. Following Rahim et al [27], it can be expected that two-phase heat transfer coefficients will increase steeply from their single-phase values upon the initiation of nucleate boiling, for incrementally positive flow qualities, then decrease by transition to intermittent flow, as vapor "slugs" pass through the pin fin array and induce portions of alternating thin film evaporation and local dryout at the wall and surrounding pin fins. As the end of the slug-vapor

intermittent regime and the onset of annular flow is approached, the heat transfer coefficient can be expected to plateau and then begin to increase as thin film evaporation becomes the dominant heat transfer mechanism and rising heat transfer coefficients result from thinning of the evaporating liquid film surrounding the pin fins. Farther into the annular regime, a decrease in the heat transfer coefficient occurs, resulting from widespread local dryout of the liquid film. While the exact flow regime progression for pin fin microchannels is as yet unknown, the similarity of the observed variation in the heat transfer coefficient with exit quality to that seen in microgap channels provides an initial basis for interpreting these empirical results.

Comparison to the Literature

As expected, there is significant disagreement between the two phase correlations in the literature and the HFE-7200 data, as illustrated in Figure 6.5. Especially of note is the multiple inflection points of the average heat transfer coefficient over exit quality which are not readily captured by 2 of the 3 available correlations. Interestingly however, the Qu and Siu-Ho correlation does appear to follow the overall decreasing trend of the data, but in general, overpredicts with an MAE of 110.4% for the inline array and 59.32% for the staggered array. The Krishnamurthy and Peles correlation fails to capture the trend of the heat transfer coefficient with exit quality for HFE-7200, but has an overall MAE of 87.5% for the inline array and 93.6% for the staggered array. Since none of the available correlations were developed for HFE-7200, it is expected that they would not predict the current data well. In addition to the geometrical deviation of the current pin fin arrays to each of the correlations as mentioned in the previous section for water, the

heat fluxes for HFE-7200 are particularly low for both arrays and out of the range of the correlations. Additionally, the exit qualities in the current HFE-7200 data substantially exceeded the maximum observed for any of the literature from which these correlations were borrowed. The maximum observed exit quality was in Qu and Siu-Ho and was 26%.

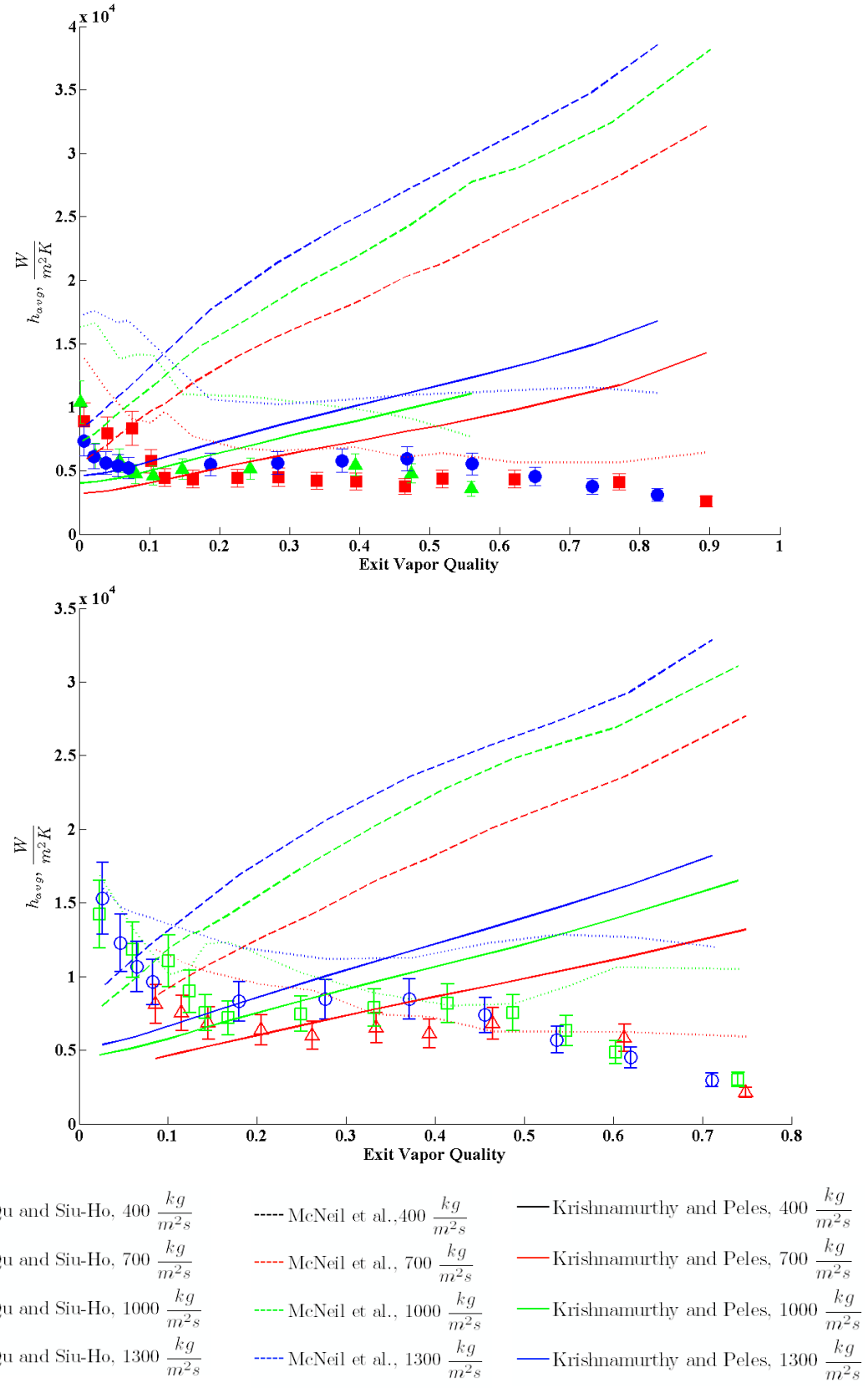

Figure 6.5: Comparison of average two phase heat transfer coefficient for HFE-7200 in the inline array (top) and staggered array (bottom), to the current correlations available in the open literature. Error bars indicate ±16%.

6.3 Two Phase Pressure Drop

Plots of two phase pressure drop versus exit quality for both deionized water and HFE-7200, in the in-line and staggered arrays, is given in this section. A comparison with the literature is then presented.

Deionized Water Experimental Results

Two phase pressure drop for deionized water corresponding to the same data points presented in Chapter 6.2 are shown in Figure 6.6. Water entered the test

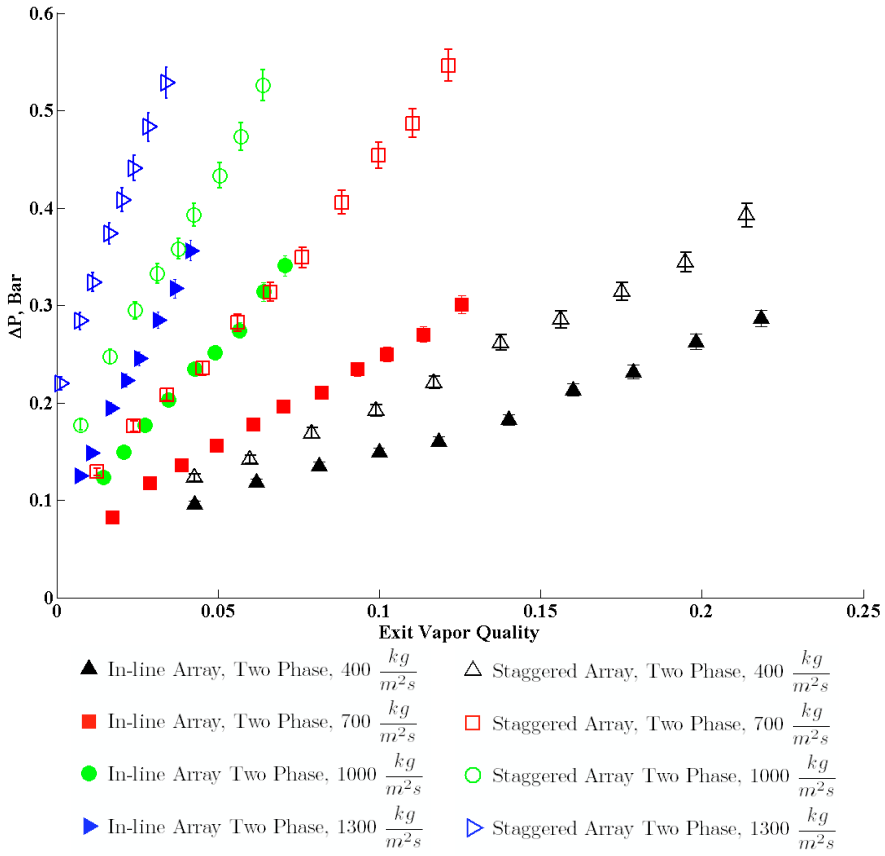

Figure 6.6: Two phase pressure drop for deionized water in the inline and staggered arrays. Error bars indicate ±3%.

sections at about 95°C to keeping the subcooling low to subsequently allow exit qualities to be as high as possible, while keeping surface temperatures below 140°C to prevent thermal destruction of the testing apparatus or any components.

The staggered array pressure drop - corresponding to the same exit quality and mass flux as the inline array - is at least 50% higher than the inline array. As the mass flux is increased, the magnitude and slope of the pressure drop become larger and steeper. The increase of pressure drop at increasing exit quality and heat flux (at constant flow rate) can be explained by vapor generation inside the test section: as heat flux becomes larger the amount of vapor produced in the pin fin array along the flow direction increases. The vapor travels downstream at a significantly higher velocity than the liquid, which in turn applies a shear force to the liquid film on the fins and causes more frictional drag along the wall.

Comparison to the Literature

The correlation that will be utilized for pressure drop prediction is by Qu and Siu-Ho. See Chapter 2.3 for a detailed outline of the correlation.

The Qu and Siu-Ho correlation was compared to the experimental water pressure drop data for both arrays. Unfortunately a large deviation between the correlation and the data occurred. The deviation was large enough to rule out significant parametric or geometric differences between Qu and Siu-Ho and the current experiments as the main cause. It will be shown in a later section that modifying the correlation by using a different single phase friction factor suited for our data will significantly improve its prediction accuracy.

HFE-7200 Experimental Results

6.7 is a plot of the HFE-7200 experimental two phase pressure drop for both arrays. Similar to the water results, the staggered array pressure drop is about 50% higher than the inline array at the same exit quality and mass flux. It is interesting to note that, at high HFE-7200 exit qualities of about 60% to 70%, the magnitude of the HFE-7200 pressure drop is close to the water results obtained for exit qualities of about 20%. The large level of vapor generation within pin fin array will cause significant vapor velocity and therefore frictional drag along the pin fins and array walls, even though flow rates are lower than the deionized water experiments.

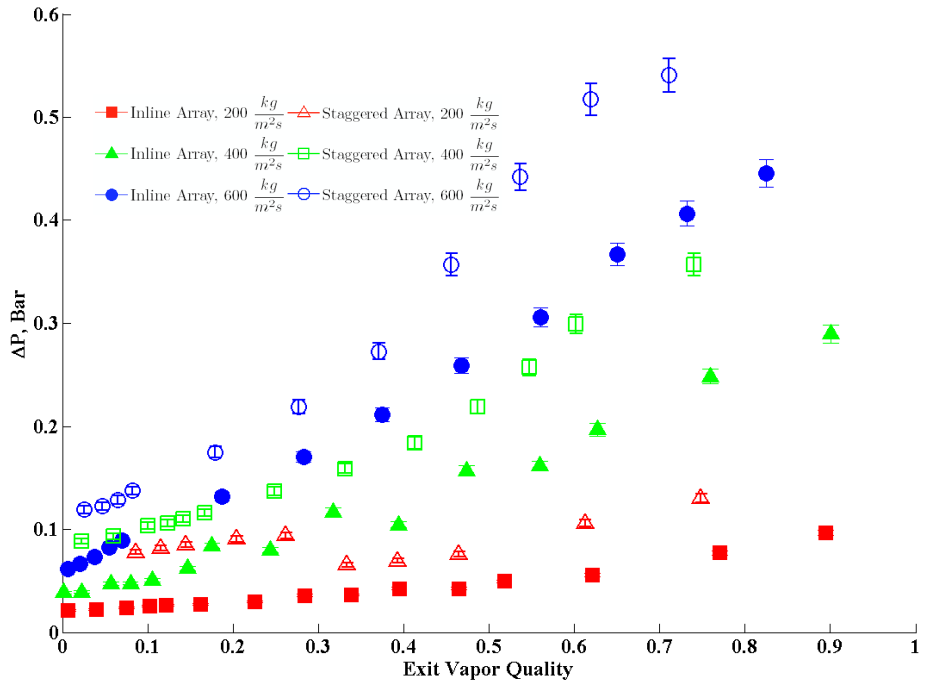

Figure 6.7: Two phase pressure drop for HFE-7200 in the inline and staggered arrays. Error bars indicate ±3%.

Comparison to the Literature

The correlation that will be utilized for pressure drop prediction is by Qu and Siu-Ho. See Chapter 2.3 for a detailed outline of the correlation.

Like the prediction for water in the previous section, it was found that Qu and Siu-Ho grossly overpredicts the pressure drop for the inline and staggered arrays. However this time, since the correlation was developed for water and low exit qualities, significant deviation with HFE-7200 is expected. In a later section it will be shown that substituting a single phase friction factor in the correlation, along with other modifications, will improve the correlation.

6.4 New Correlation for Two Phase Heat Transfer Coefficient

As described in Section 6.2 of this chapter, correlations available in the literature are unable to predict the current two phase heat transfer coefficient data, especially over the broad range of exit qualities that were investigated. Therefore it is important to develop a robust new correlation that can predict the performance of the inline and staggered arrays for both water and HFE-7200 with low average error. Since the Krishnamurthy and Peles correlation had the best overall performance, we will start with the same form they developed and make a few key changes to improve it. First, the Nusselt number correlation by Short et al. used by Krishnamurthy and Peles was originally developed for large, air-cooled pin fin heat sinks at laminar

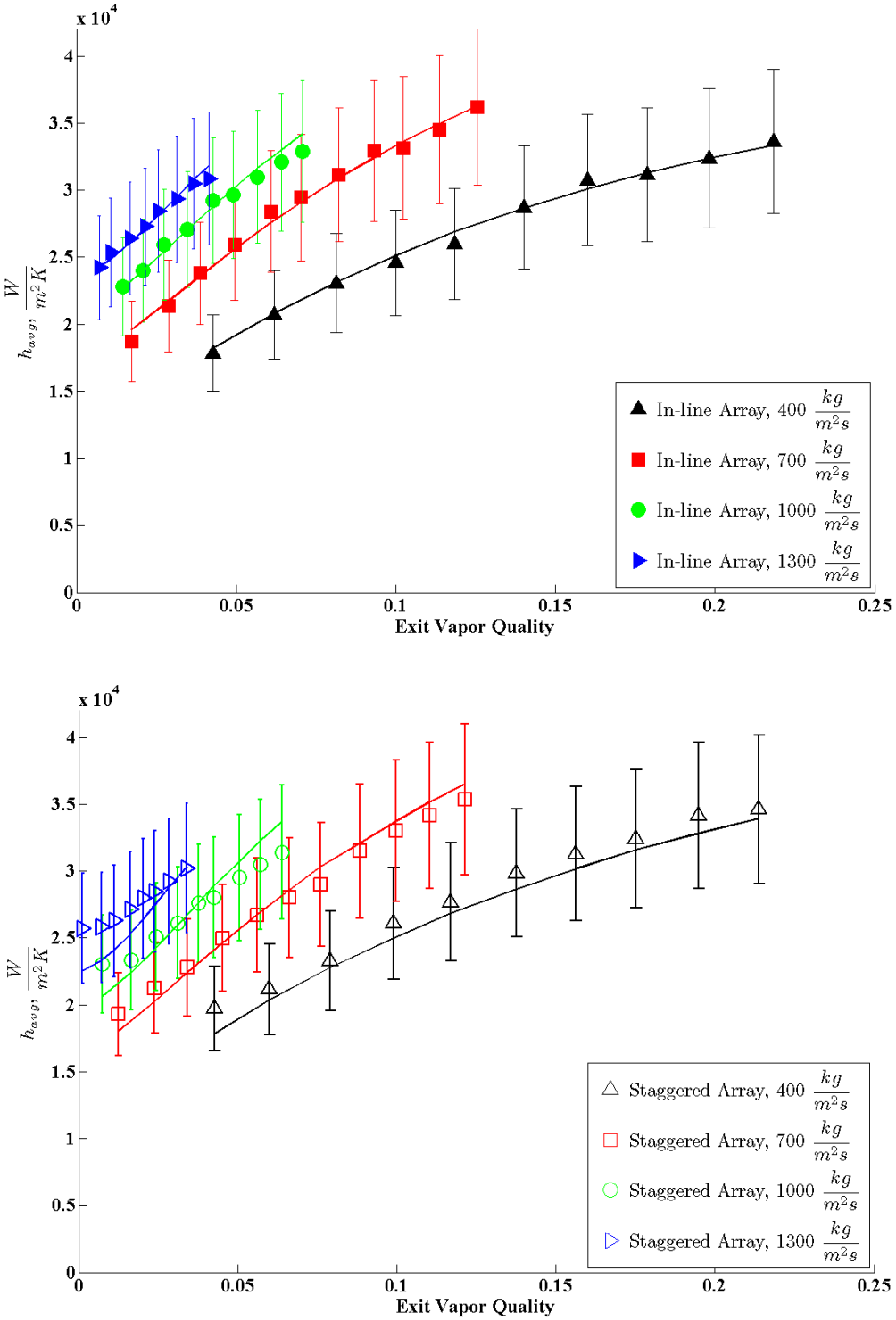

Figure 6.8: New two phase heat transfer coefficient correlation prediction for water in the inline array (top) and staggered array (bottom)

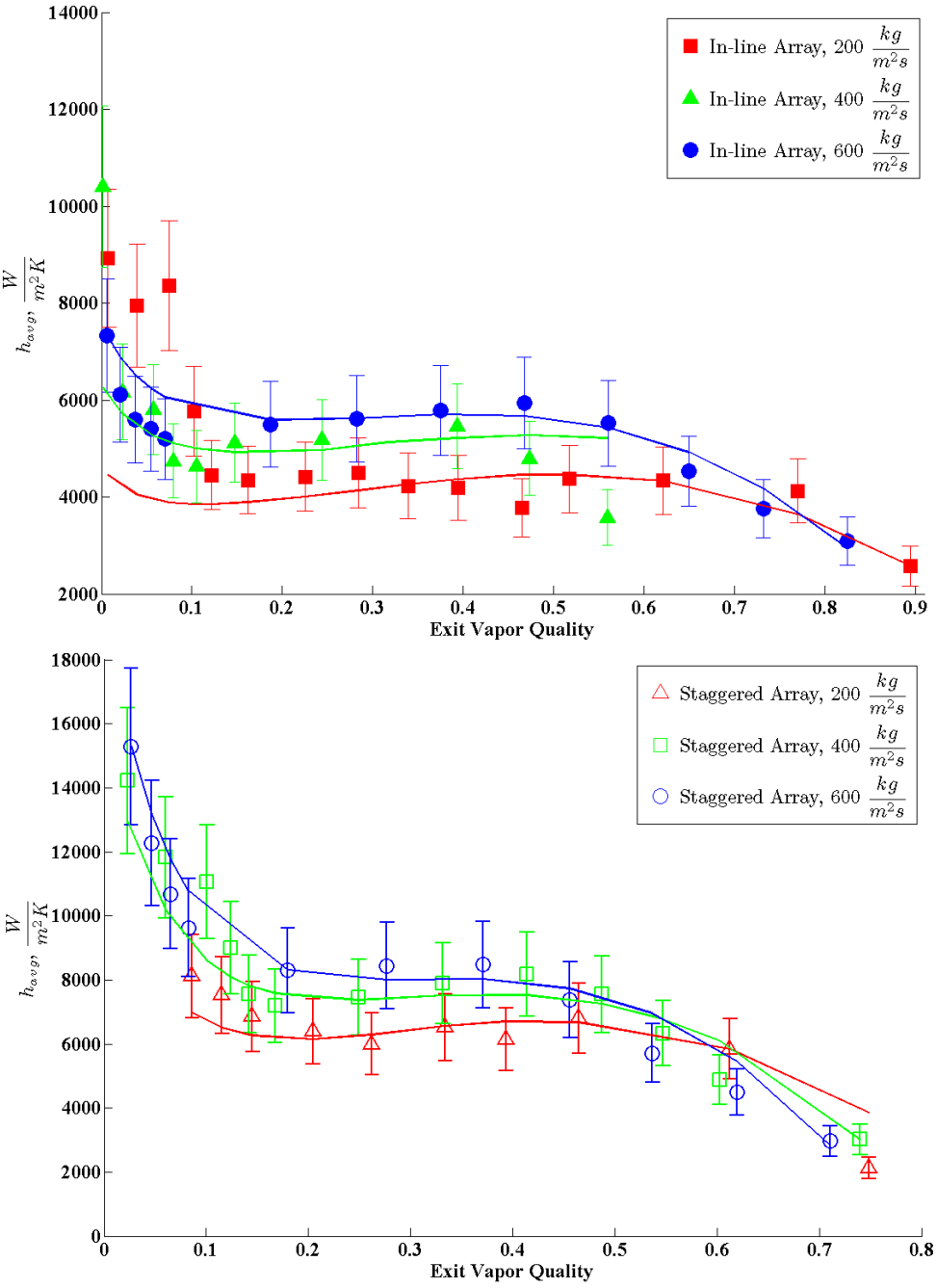

Figure 6.9: New two phase heat transfer coefficient correlation prediction for HFE-7200 in the inline array (top) and staggered array (bottom)

Reynolds numbers less than 10^3. Since good prediction accuracy for the current single phase data was obtained with the Tullius et al. Nusselt number correlation using optimized shape factors in Chapter 5.2, these will be used in place of the Short et al. relation.

Next, the constant ζ=1 correction factor for the average heat transfer coefficient, will instead be replaced by an enhancement equation with exit quality and mass flux dependence. The equation will have 5 variable constants, C_1, C_2, C_3, C_4, and C_5. This will facilitate generation of the final correlation for average heat transfer coefficient by allowing adjustment of the shape of the curve for both pin fin arrays over the entire range of exit quality. The form of the equation will be:

$$\zeta = C_1 e^{C_2 x_e} + C_3 x_e^3 + \left(\frac{C_4}{G + C_5} \right)^{1/2}$$

The form of this equation has a quality dependent exponential function in the first term, an exit quality dependent cubic function in the second term, and a mass flux dependent function in the third and final term. The unit of mass flux, G, is $\frac{kg}{m^2 s}$.

After using this new two phase equation and selecting the constants $C_1 - C_5$ that minimize MAE for both arrays, the resulting prediction curves for deionized water are shown in Figure 6.8 Since the experimental water heat transfer coefficients for the inline and staggered arrays were nearly the same, one set of constants were used to generate the equation. A remarkably small MAE of 2.44% was obtained overall for water.

For HFE-7200, two sets of constants were optimized separately, each for the inline and staggered arrays. The prediction curves are shown in Figure 6.9. An MAE of 13.16% was obtained for the inline array and an MAE of 10.18% was obtained for the staggered array. A summary of the new correlation along with the constants used is given in Table 6.1.

Table 6.1: New Heat Transfer Coefficient Correlation Summary

$$Nu = C_{Nu}\left(\frac{S_L}{D_f}\right)^{0.2}\left(\frac{S_T}{D_f}\right)^{0.2}\left(\frac{h_f}{D_f}\right)^{0.25}\left(1+\frac{dh}{D_f}\right)^{0.4}\mathrm{Re}^{0.6}\,\mathrm{Pr}^{0.36}\left(\frac{\mathrm{Pr}}{\mathrm{Pr}_w}\right)^{0.25} \qquad h_{sp} = \frac{Nu\cdot k_f}{d_{fin}} \qquad \left(\Delta P_f\right)_f = \frac{fN\left(G\left(1-x\right)\right)^2}{2\rho_f} \qquad \left(\Delta P_f\right)_v = \frac{fN\left(Gx\right)^2}{2\rho_v}$$

$$\zeta = C_1 e^{C_2 x_e} + C_3 x_e^3 + \left(\frac{C_4}{G+C_5}\right)^{1/2} \qquad X_{vv} = \left[\frac{\left(\Delta P_f/\Delta Z\right)_f}{\left(\Delta P_f/\Delta Z\right)_v}\right]^{1/2} \qquad \left(\phi\right)^2 = 1+\frac{0.24}{X_{vv}}+\frac{1}{X_{vv}^2} \qquad h_{tp} = \zeta\left(\phi^2\right)^{0.2475} h_{sp}$$

Fluid	Array	C_{Nu}	C_1-C_5	MAE
Water	Inline	0.0495	C_1= -0.07 C_2=4.3 C_3= 0 C_4=80 C_5=2965	2.44%
Water	Staggered	0.0413	C_1= -0.07 C_2=4.3 C_3= 0 C_4=80 C_5=2965	2.44%
HFE-7200	Inline	0.054	C_1= 2.47 C_2=-9.2 C_3= -1.71 C_4=45 C_5=181	13.16%
HFE-7200	Staggered	0.065	C_1= 6.0 C_2= -14.15 C_3= -3.63 C_4=45 C_5=88	10.18%

6.5 New Correlation for Two Phase Pressure Drop

It was demonstrated in Section 6.3 of this chapter that the current pressure drop correlation by Qu and Siu-Ho in its published form cannot predict the experimental data of this work. It was discovered that the reason for this

incongruency between the correlation and the experimental data is mainly due to lack of a suitable single phase friction factor. Therefore the optimized Tullius et al. friction factors for pressure drop for water in Chapter 5.3 will be substituted in place of the Qu and Siu-Ho friction factors that were developed for their test section. With this one update to the correlation, deionized water prediction is improved to 41.9% MAE for the inline array and 36% MAE for the staggered array. Furthermore, if the constant C of the Lockhart-Martinelli parameter is changed from 5 to 10 for the inline array, and to 8 for the staggered array, even better accuracy of 15% MAE for the inline array and 17.3% MAE for the staggered array is obtained. Figure 6.10 is a demonstration of the new correlation's prediction. For low exit qualities, the ΔP_{sub} term plays a more dominant role in the total two phase pressure drop since saturated boiling will occur nearer to the exit. Conversely, as exit quality is increased, saturated boiling will commence farther upstream therefore the ΔP_{sat} term will contribute an overall higher percentage to the total two phase pressure drop.

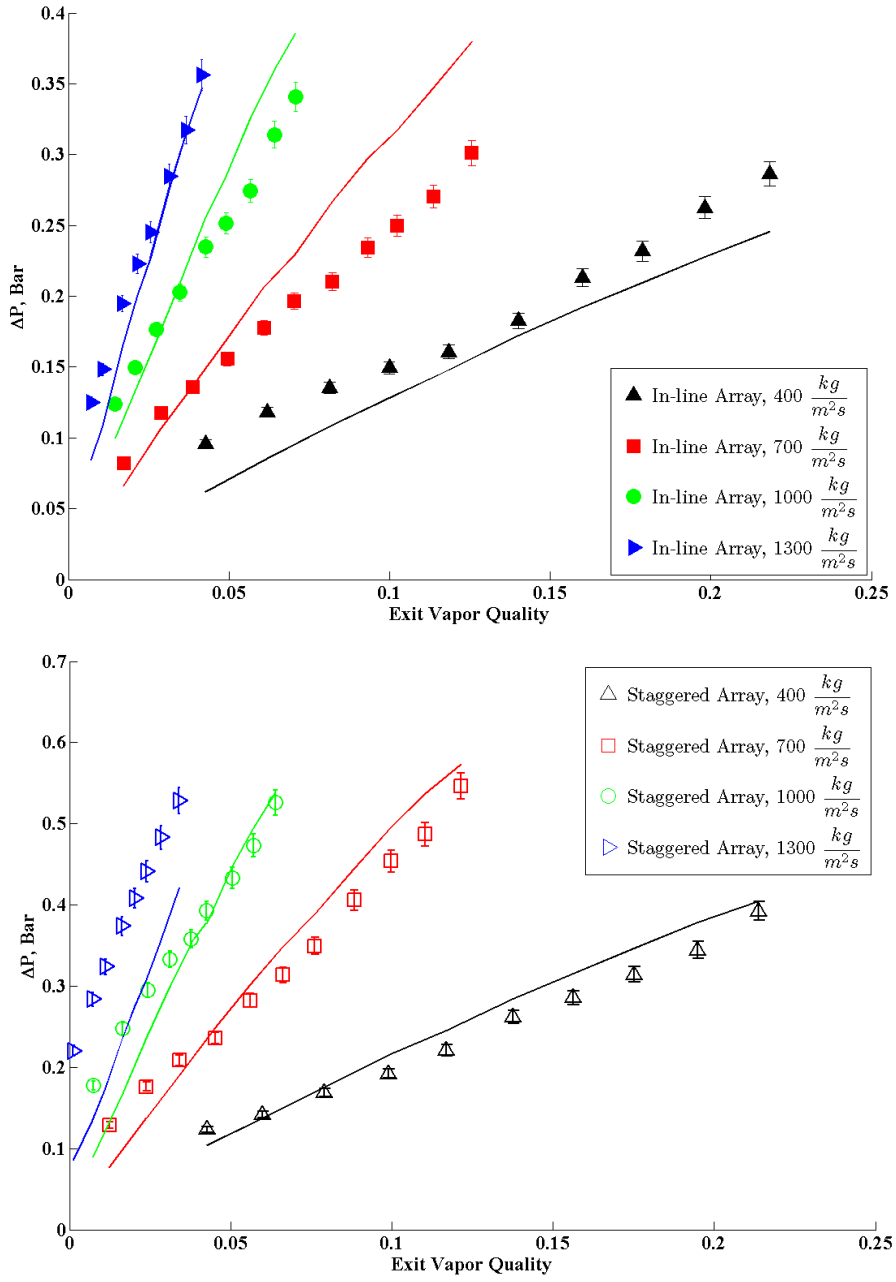

Figure 6.10: New two phase pressure drop correlation prediction for water in the inline array (top) and staggered array (bottom)

The same methodology to generate the correlation for water above was applied to HFE-7200, namely, to substitute the optimized Tullius et al. single phase friction factors for HFE-7200 obtained in Chapter 5.3. Unfortunately, the MAE of the correlation after this modification did not improve substantially, due to an abnormally inflated ΔP_{sat} term. Likewise, changing the Lockhart-Martinelli constant C did not have any appreciable effect on the prediction accuracy. In order to preserve the prediction quality of the ΔP_{sub} term and maintain consistency of f_{sp} in both terms,

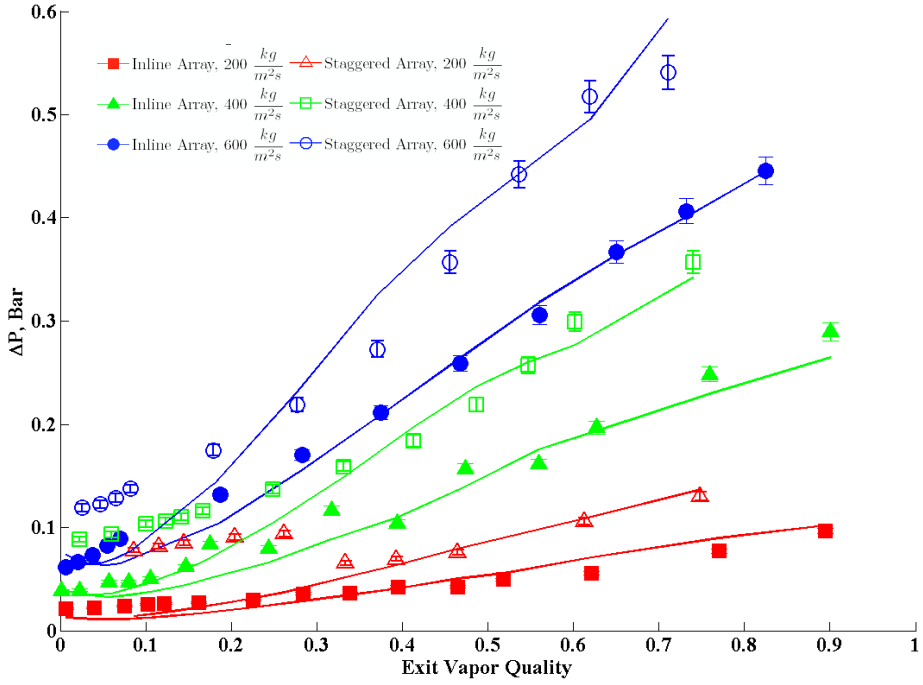

Figure 6.11: New two phase pressure drop correlation prediction for two phase HFE-7200 in the inline and staggered arrays.

an adjustment factor will be introduced to ΔP_{sat}. This adjustment factor, λ, will be selected separately for both arrays to produce minimum MAE. For the inline array, this factor will be 0.027 and for the staggered array it will be 0.044, which improves the MAE to 18.4% for the inline array and 30.6% for the staggered array. The new

correlation prediction for the current data is shown in Figure 6.11. It should be noted that most of the error is concentrated in the low exit quality region therefore better accuracy should be obtained when using the correlation for high exit qualities. Table 6.2 is a summary of the new two phase pressure drop correlation for both arrays and both working fluids.

Table 6.2: New Pressure Drop Correlation Summary

$$\Delta P_{sub} = \sum_{i=1}^{N_{sat}-1}\left[f_{sp,,i}\left(\frac{\mu_{f,i}}{\mu_{w,i}}\right)^{0.58}\frac{G^2}{2\rho_{f,i}}\right] \qquad \Delta P_{sat} = \sum_{i=N_{sat}}^{N_f}\left[\lambda f_{sp,,i}\frac{v_{f,i}G^2(1-x_{local,i})^2}{2}\phi_{f,i}^2\right] \qquad \phi_f^2 = 1+\frac{C}{X_{vv}}+\frac{1}{X_{vv}^2}$$

$$X_{vv} = \left(\frac{\mu_f}{\mu_g}\right)^{0.274}\left(\frac{1-x_{local}}{x_{local}}\right)^{0.727}\left(\frac{v_f}{v_g}\right)^{0.5} \qquad f_{sp} = C_f\left(\frac{S_L}{D_f}\right)^{0.2}\left(\frac{S_t}{D_f}\right)^{0.2}\left(\frac{h_f}{D_f}\right)^{0.18}\left(1+\frac{dh}{D_f}\right)^{0.2}\mathrm{Re}_f^{-0.435} \qquad \Delta P_{tp} = \Delta P_{sub} + \Delta P_{sat}$$

Fluid	Array	C_f	C	λ	MAE
Water	Inline	0.62	10	1	15%
Water	Staggered	0.78	8	1	17.3%
HFE-7200	Inline	4.77	5	0.027	18.4%
HFE-7200	Staggered	2.89	5	0.044	30.6%

Chapter 7: Solar Energy Analysis for the Pin Fin Arrays

7.1 Introduction

In this Chapter both the staggered and inline pin fin arrays will be analyzed on the basis of maximum COP and COP_T for a CPV module. A comparison with similar microchannel geometry as well as a microgap channel with the same conditions and working fluid will be made.

7.2 Embodied Energy of Copper

The least-energy, least-material analysis of Chapter 3 was for an Aluminum microcooler. The experimental study of Chapters 5 and 6 were for the Copper pin fin arrays, therefore the previous 85 kWh/kg value for the embodied energy of Aluminum is not applicable to Copper.

After a search for appropriate estimates of embodied energy for Copper, it was found that the work by Ashby [45] is the most comprehensive, and includes embodied energy values for many materials. The embodied energy is categorized into 3 parts: material, processing and recycling. For Copper, these 3 values are 20.5 kWh/kg in material energy, 1.4 kWh/kg in processing energy, and 5.14 kWh/kg in recycling energy. Summing all 3 of these parts we will get 27 kWh/kg as the embodied energy for Copper. This value is significantly lower - about 30% that of the 85 kWh of Aluminum - which is due to Copper's much lower material embodied energy in primary production.

7.3 Least-Material and Least-Energy Analysis for the Micro Pin Fin Arrays

A cell aperture area equivalent to the 28.8mm x 9.6mm base area of the pin fin coolers will be assumed in the forthcoming analysis. This is a valid assumption since Spectrolab 40% efficient, triple junction CPV cells are available in multiple sizes, as small as 5.5mm x 5.5mm. Therefore the 28.8mm x 9.6mm area could be considered as a cooling "module" of 3 or more CPV cells, which could then be used with other modules in a theoretical two phase manifold cooling system. This concept is similar to the Solar Systems single phase liquid cooling manifold design [16].

For a complete analysis, longitudinal-finned microchannels of similar geometry and aspect ratio to the inline pin fin array, and a microgap cooler will be included in the comparison model. The microchannel cooler will have 31 channels with the same channel width and height of 153μm and 305μm respectively. The microgap cooler will have 1mm thick walls and a 1mm thick base with a channel height of 305μm. All coolers are assumed to have the same 1mm thick base wall, along with a 50μm layer of 63% Sn/37% Pb solder as the cell's thermal interface material. Working fluid for all simulations will be water.

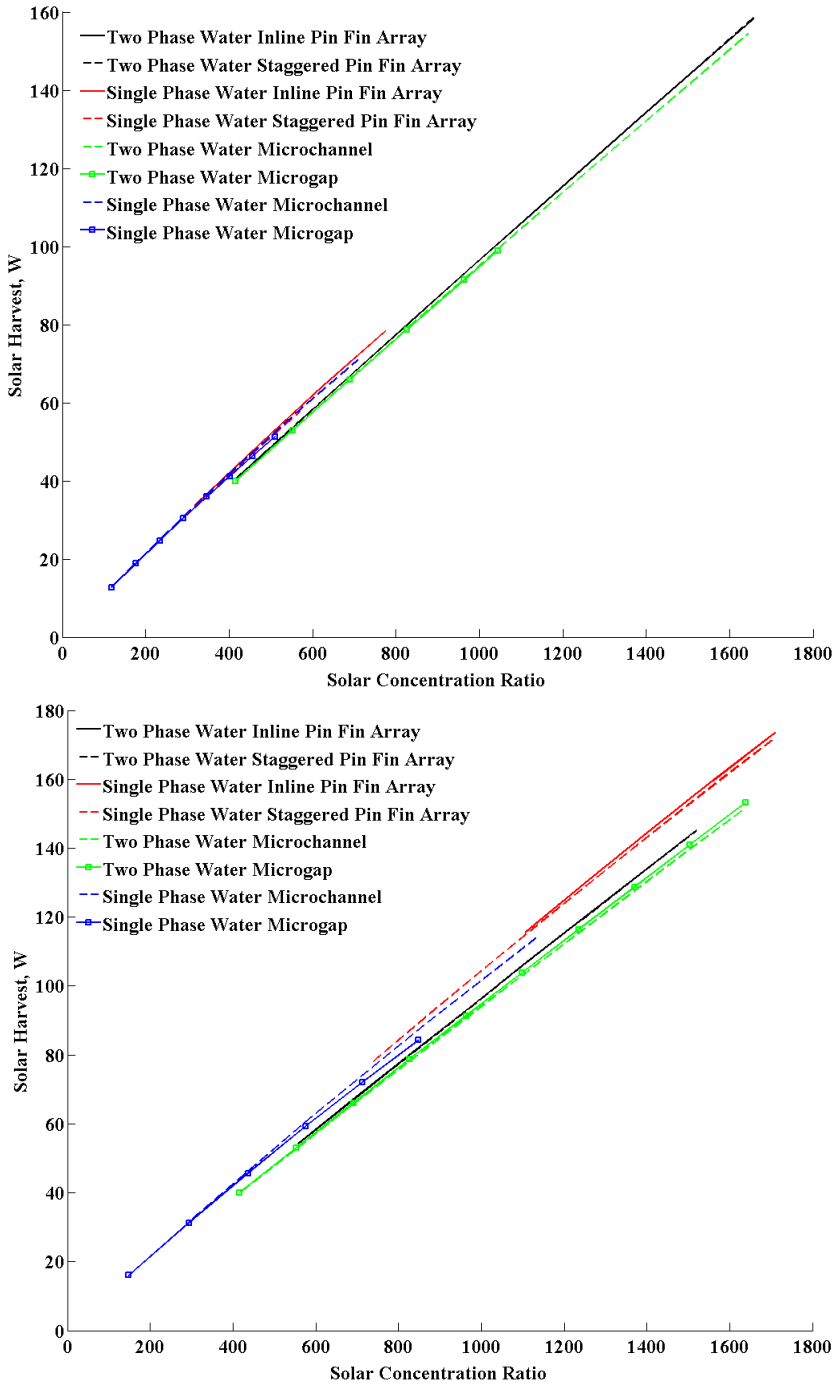

Figure 7.1: Solar Energy Harvest for a constant mass flow rate of 33 g/min (top) and 70 g/min (bottom). Solar heat flux range from 20 W/cm^2 – 165 W/cm^2.

Figure 7.1 is the solar energy harvest, which is the total power generated by the theoretical Spectrolab triple junction CPV module, minus pumping power, for a heat flux range from 20 W/cm^2 – 165 W/cm^2. Embodied energy is not included in the

solar harvest analysis or Figure 7.1. A constant flow rate of 33 g/min for the top plot, and 70 g/min for the bottom plot of Figure 7.1 is assumed for each cooler in each of the respective plots. It is easy to see upon inspection of both plots of Figure 7.1 that the pin fin energy harvest is better for the pin fin arrays than the microchannel and microgap coolers by 1 to 10 watts, depending on the concentration ratio and flow rate. The difference between the inline and staggered arrays ranges from less than 1 watt to 1 watt with the inline array having a slight advantage in solar harvest.

For the low flow rate in the top plot of Figure 7.1, the single phase microchannel, the single phase pin fin coolers and single phase microgap cooler are not able to provide cooling above 800 suns. Also the two phase microgap cooler cannot provide cooling above 1100 suns due to reaching CHF above this point. Further, both of the two phase pin fin coolers, which are able to provide cooling to over 1600 suns, will generate 160 watts of usable power for our theoretical CPV module.

Shifting attention to the bottom of Figure 7.1 we can see that the pin fin arrays still facilitate the best solar power generation by the CPV module. However, due to the high flow rates in this case the single phase pin fins are able to provide lower average base temperature and thus generate 10 more watts than the two phase pin fin coolers at an eqivalent concentration of 1500 suns.

The COP_T, which is defined in Equation 3.2, is shown in Figure 7.2 and includes the embodied energy of the copper microcooler. The highest COP_T of 8 $x10^4$ is obtained by the single phase microgap at 500 suns, which sharply increases up to

this maximum value due to constant single phase pumping power over increasing insolation. The two phase cooling devices COP_T's, however, are generally more constant. In the range shown, the two phase pin fin coolers stay near 10^4 over the entire range and are the most energy efficient microcooler for cooling above 1000 suns. In the bottom plot of Figure 7.2, COP_T is substantially lower for all arrays due to the higher flow rate and thus higher pumping power. Once again the inline single phase pin fins provide the best cooling, even up to 1700 suns, but does so only at a higher flow rate. Thus, at these higher heat fluxes or insolations above 1000 suns, the COP_T is higher - and therefore more energy efficient - when utilizing lower flow rate two phase pin fin cooling.

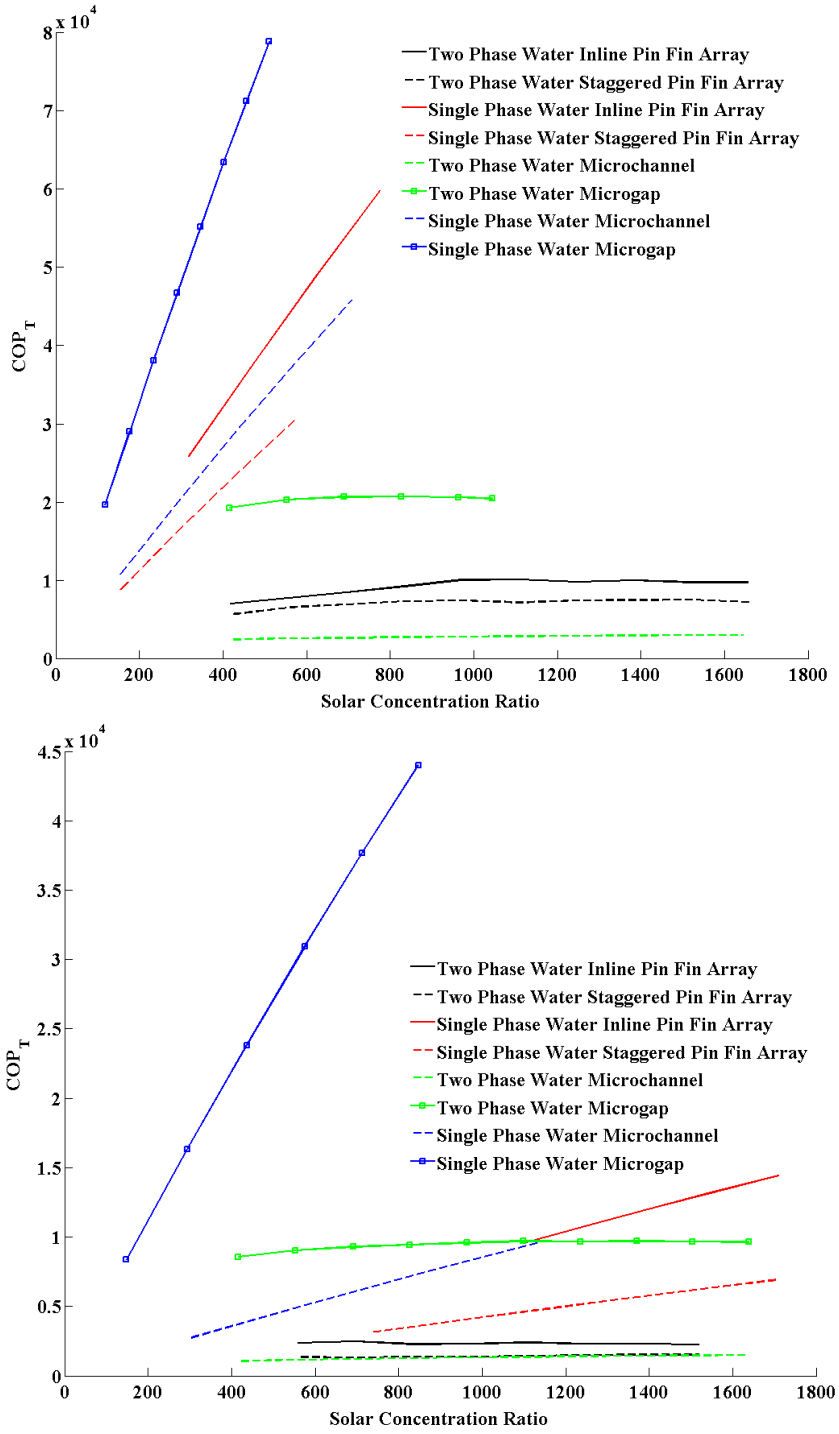

Figure 7.2: COP_T for a constant mass flow rate of 33 g/min (top) and 70 g/min (bottom). Solar heat flux range from 20 W/cm^2 – 165 W/cm^2.

7.3 Conclusion

In this chapter, the micro pin fin arrays were compared to a geometrically similar microchannel array as well as a microgap channel, using water as the working fluid in single phase and two phase. It was concluded that at high heat fluxes encountered at 1000 suns, and higher for high solar power generation at low flow rates, two phase micro pin fins are the most energy efficient design. For high flow rates and high heat flux cooling, single phase pin fins provide the most energy efficient design choice. For low heat flux encountered at low concentration ratio, single phase microgap maintains lower cell temperatures for the lowest parasitic pumping penalty. For both single phase and two phase cooling, inline pin fin arrays are generally more energy efficient than staggered arrays.

The analysis in this chapter could be repeated for refrigerants, which due to lower saturation temperatures and therefore lower base temperatures, could generate better COP_T for the CPV cells. It is expected that such an analysis repeated for refrigerants would draw similar conclusions to the current work with water.

Bibliography

[1] http://www.eia.gov/totalenergy/data/annual/pdf/aer.pdf

[2] P. Pérez-Higueras, E. Mu˜noz, G. Almonacid, P.G. Vidal, High Concentrator PhotoVoltaics efficiencies: Present status and forecast, Renewable and Sustainable Energy Reviews, 15 (2011) 1810-1815

[3] Yastrebova, N.V. High-efficiency multi-junction solar cells: Current status and future potential. University of Ottawa (2007)

[4] Luque, A., Hegedus, *Handbook of photovoltaic science and engineering*. John Wiley & Sons, 2003

[5] van Kessel, T.; Abduljabar, A.; Khonkar, H.; Moumen, N.; Sandstrom, R.; Al-Saaedi, Y.; Martin, Y.; Guha, S.; Concentrator photovoltaic reliability testing at extreme concentrations up to 2000 suns. Photovoltaic Specialists Conference 2009 34th IEEE 1020-1023

[6] Royne, Anja. "Cooling of photovoltaic cells under concentrated illumination: A critical review." Solar energy materials and solar cells 86.4 (2005):451-483.

[7] Landis, G. A., Merritt, D. Raffaelle, R. P., Scheiman, D. High-Temperature Solar Cell Development NASA 2005

[8] http://www.spectrolab.com/DataSheets/PV/CPV/C4MJ_40Percent_Solar_Cell.pdf

[9] Green, M. A., Emery, K., Hishikawa, Y., Warta, W. and Dunlop, E. D. (2012), Solar cell efficiency tables (version 39). Prog. Photovolt: Res. Appl., 20: 12–20. doi: 10.1002/pip.2163

[10] Yoon, Sewang. "Reduced temperature dependence of high-concentration photovoltaic solar cell open-circuit voltage (Voc) at high concentration levels." Conference Record of the IEEE Photovoltaic Specialists Conference 2(1994):1500-1504.

[11] Incropera, Frank P., and David P. DeWitt. *Fundamentals of Heat and Mass Transfer*. New York: Wiley, 2002.

[12] Cui, Min. "Thermal analysis and test for single concentrator solar cells." Journal of Semiconductors 30.4 (2009)

[13] http://www.greenvolts.com/system/complete-fully-integrated-system/module

[14] http://solarsystems.com.au/technology-2/cpv-systems-overview/cooling/

[15] P.J. Verlinden, A. Terao, D.D. Smith, K. McIntosh, R.M. Swanson, G. Ganakas, J.B. Lasich, Will we have a 20%-efficient (PTC) photovoltaic system? Conference record, Proceedings 17th European Photovoltaic Solar Energy Conference, 2001

[16] J.B. Lasich, Cooling circuit for receiver of solar radiation, Patent WO02080286, 2002, Australia.

[17] Verlinden, P J. "Performance and reliability of a 30-kW triple-junction photovoltaic receiver for 500X concentrator dish or central receiver applications." Proceedings of SPIE--the international society for optical engineering 6339(2006)

[18] Verlinden, P.J.; Lewandowski, A.; Kendall, H.; Carter, S.; Cheah, K.; Varfolomeev, I.; Watts, D.; Volk, M.; Thomas, I.; Wakeman, P.; Neumann, A.; Gizinski, P.; Modra, D.; Turner, D.; Lasich, J.B.; , "Update on two-year performance of 120 kWp concentrator PV systems using multi-junction III–V solar cells and parabolic dish reflective optics," *Photovoltaic Specialists Conference, 2008. PVSC '08. 33rd IEEE* , vol., no., pp.1-6, 11-16 May 2008

[19] Ho, Tony. "Improving efficiency of high-concentrator photovoltaics by cooling with two-phase forced convection." International journal of energy research 34.14 (2010):1257-1271.

[20] D. Copeland, “Optimization of parallel plate heat sinks for forced convection,” Proceedings of 16th IEEE SEMI-THERM Symp (SEMI-THERMAL 2000), San Jose, CA, 2000, pp. 266–272.

[21] V. Gnielinski, New Equations for Heat and Mass Transfer in Turbulent Pipe and Channel Flow, International Chemical Engineer, 16(1976)359-368.

[22] S. Kakac, The effect of temperature dependent fluid properties on convective heat transfer, Handbook of Single-Phase Convective Heat Transfer, John Wiley, New York, 1987

[23] W. M. Kays, A. L. London, “Compact Heat Exchangers”, McGraw-Hill, 1984.

[24] White, Frank, “Viscous Flow in Ducts” in *Fluid Mechanics, 6th ed.* New York, McGraw-Hill, 2008, Ch 6.3, pg 350

[25] F. Mei, P. R. Parida, J. W. Meng, and S. V. Ekkad, “Fabrication, assembly, and testing of Cu-and Al-based microchannel heat exchangers, ” Journal of Microelectromechanical Systems, 17(2008)869-881.

[26] Chen, J., Correlation for Boiling Heat Transfer to Saturated Fluids in Convective Flow. I&EC Process Design and Development, Vol. 5 No. 3 (1966): 322-329

[27] Rahim, E., Revellin, R., Thome, J., Bar-Cohen, A., Characterization and prediction of two-phase flow regimes in miniature tubes, Int. J. of Multiphase Flow 37 (2011), 12-23.

[28] Dittus, F. W., and Boelter, L. M. K., Heat Transfer in Automobile Radiators of the Tubular Type, University of California Publica- tions in Engineering, vol. 2, pp. 443–461, 1930.

[29] Forster, H. K., and Zuber, N., Dynamics of Vapor Bubbles and Boiling Heat Transfer, AIChE Journal, vol. 1, no. 4, pp. 531–535, 1955.

[30] A. Bar-Cohen and E. Rahim, Modeling and prediction of two-phase microgap channel heat transfer characteristics, Heat Transfer Eng. **30** (8) (2009), pp. 601–625.

[31] Wang, P., McCluskey, F. P., Bar-Cohen, A. Evaluation of Two-Phase Cold Plate for Cooling Electric Vehicle Power Electronics. 2011 ASME International Mechanical Engineering Congress & Exposition

[32] Qu, W., Mudawar, I., Measurement and Correlation of Critical Heat Flux in Two-Phase Microchannel Heat Sinks. Int. Journal of Heat and Mass Transfer. Vol. 47 (2004): 2045-2059

[33] Muller-Steinhagen, H., Heck, K., A Simple Friction Pressure Drop Correlation for Two-Phase Flow in Pipes. Chemical Engineering and Processing. Vol. 20 (1986): 297-308

[34] Tullius, J., Tullius, T. Bayazitoglu, Y. Optimization of short micro pin fins in minichannels. Int. J. Heat Mass Transfer 55 (2012) 3921-3932

[35] S. Krishnamurthy, Y. Peles, Flow boiling of water in a circular staggered micro-pin fin heat sink, Int. J. Heat Mass Transfer 51 (2008) 1349-1364.

[36] W. Qu, A. Siu-Ho, Experimental study of saturated boiling heat transfer in an array of staggered micro-pin-fins, Int. J. Heat Mass Transfer 52 (2009)

[37] McNeil, D. Raeisi, A. Kew, P. Bobbili, P. "A comparison of flow boiling heat-transfer in in-line mini pin fin and plane channel flows." Applied thermal engineering 30.16 (2010):2412-2425.

[38] Qu, W., Siu-Ho, A. Measurement and prediction of pressure drop in a two-phase micro-pin-fin heat sink, Int. J. Heat Mass Transfer 52 (2009) 5173-5184

[39] Iyengar, M. & Bar-Cohen, A. Least-Energy Optimization of Forced Convection Plate-Fin Heat Sinks. IEEE TCPT Vol. 26 No. 1 (2003)

[40] http://www.spectrolab.com/DataSheets/PV/CPV/C4MJ_40Percent_Solar_Cell.pdf

[41] Olson, J.M., Friedman, D.J., Kurtz, S., High-Efficiency III-V Multijunction Solar Cells. Handbook of Photovoltaic Science and Engineering. Ch 9 (2003)

[42] R. Jones. "FW: University of Maryland - 40% point focus terrestrial cell" Personal e-mail (Oct 25, 2011)

[43] Green, Martin A., et al. "Solar cell efficiency tables (version 39)." *Progress in photovoltaics: research and applications* 20.1 (2011): 12-20.

[44] Yoon, Sewang, and Vahan Garboushian. "Reduced temperature dependence of high-concentration photovoltaic solar cell open-circuit voltage (Voc) at high concentration levels." *Photovoltaic Energy Conversion, 1994., Conference Record of the Twenty Fourth. IEEE Photovoltaic Specialists Conference-1994, 1994 IEEE First World Conference on*. Vol. 2. IEEE, 1994.

[45] Ashby, Michael F. *Materials and the Environment: Eco-Informed Material Choice*. Butterworth-Heinemann, 2009.